

## From wave speed to cardiac stiffness

Sabbadini, S.

**DOI**

[10.4233/uuid:8180568b-8d79-4b1a-8f72-80c40b4c9ef0](https://doi.org/10.4233/uuid:8180568b-8d79-4b1a-8f72-80c40b4c9ef0)

**Publication date**

2021

**Document Version**

Final published version

**Citation (APA)**

Sabbadini, S. (2021). *From wave speed to cardiac stiffness*. [Dissertation (TU Delft), Delft University of Technology]. <https://doi.org/10.4233/uuid:8180568b-8d79-4b1a-8f72-80c40b4c9ef0>

**Important note**

To cite this publication, please use the final published version (if applicable).  
Please check the document version above.

**Copyright**

Other than for strictly personal use, it is not permitted to download, forward or distribute the text or part of it, without the consent of the author(s) and/or copyright holder(s), unless the work is under an open content license such as Creative Commons.

**Takedown policy**

Please contact us and provide details if you believe this document breaches copyrights.  
We will remove access to the work immediately and investigate your claim.

# **FROM WAVE SPEED TO CARDIAC STIFFNESS**



# **FROM WAVE SPEED TO CARDIAC STIFFNESS**

## **Dissertation**

for the purpose of obtaining the degree of doctor  
at Delft University of Technology,  
by the authority of the Rector Magnificus Prof.dr.ir. T.H.J.J. van der Hagen,  
chair of the Board for Doctorates,  
to be defended publicly on  
Tuesday 1<sup>st</sup> of June 2021 at 15:00 o' clock.

by

**Alberico SABBADINI**

Master of Science in Physics,  
Leiden University, the Netherlands,  
born in Milan, Italy.

This dissertation has been approved by the

promoters: Prof.dr.ir. N. de Jong and Dr.ir. M.D. Verweij

copromoters: Dr.ir. H.J. Vos and Dr.ir. A. Caenen

Composition of the doctoral committee:

Rector Magnificus,	chairperson
Prof.dr.ir. N. de Jong,	Delft University of Technology, promotor
Dr.ir. M.D. Verweij,	Delft University of Technology, promotor
Dr.ir. H.J. Vos,	University Medical Center Rotterdam, copromotor
Dr.ir. A. Caenen,	Gent University, copromotor

*Independent members:*

Prof.dr.ir. P.G. Steeneken,	Delft University of Technology
Prof.dr. M.W. Urban,	Mayo Clinic College of Medicine and Science, USA
Prof.dr.ir. P. Segers,	Ghent University, Belgium
Dr. F.H.J. Gijsen,	University Medical Center Rotterdam
Prof.dr. B. Rieger,	Delft University of Technology, reserve member



Nederlandse Organisatie voor Wetenschappelijk Onderzoek

*Keywords:* Wave propagation, modeling, Finite Elements, heart, elastography, ultrasounds, Lamb waves, local stiffness determination, time-varying medium, space-varying tapering.

*Printed by:* Ridderprint | [www.ridderprint.nl](http://www.ridderprint.nl).

*Front & Back:* Designed by Alberico and Hanna.

Copyright © 2021 by A. Sabbadini

ISBN 000-00-0000-000-0

An electronic version of this dissertation is available at  
<http://repository.tudelft.nl/>.

This work is part of the research program "Earlier recognition of cardiovascular diseases" with project number 14740, which is (partly) financed by The Netherlands Organization for Scientific Research (NWO).

*When left is not right  
only right is left.*

"In the maze", Uli



# CONTENTS

<b>Summary</b>	<b>ix</b>
<b>Samenvatting</b>	<b>xi</b>
<b>1 Introduction</b>	<b>1</b>
1.1 Hearts, heart failure and heart stiffness . . . . .	2
1.2 Waves in solids . . . . .	3
1.3 Ultrasound shear wave elastography . . . . .	5
1.4 Heart modelling. . . . .	6
1.5 Thesis goal and outline . . . . .	7
References . . . . .	8
<b>2 1D waves in temporally relaxing media</b>	<b>13</b>
2.1 Introduction . . . . .	15
2.2 Setup . . . . .	16
2.3 Results . . . . .	18
2.4 Discussion . . . . .	23
2.5 Conclusions. . . . .	26
2.6 Appendix: Reflection and transmission coefficients. . . . .	26
References . . . . .	28
<b>3 Wave propagation in the tapered septum</b>	<b>31</b>
3.1 Introduction . . . . .	33
3.2 Methods . . . . .	34
3.2.1 Experimental setup . . . . .	34
3.2.2 Experimental data analysis. . . . .	35
3.2.3 Numerical configuration. . . . .	36
3.2.4 Numerical model validation . . . . .	36
3.2.5 Numerical data analysis . . . . .	37
3.2.6 Numerical dispersion curve analysis and error map reconstruction . .	38
3.2.7 Effects of different IVS shapes . . . . .	40
3.3 Results . . . . .	41
3.3.1 Experiments . . . . .	41
3.3.2 Simulations . . . . .	42
3.4 Discussion . . . . .	46
3.4.1 Effects of tapering on SWE measurements . . . . .	46
3.4.2 Simulations versus experiments . . . . .	49
3.4.3 Limitations. . . . .	49
3.5 Conclusions. . . . .	50
References . . . . .	51

<b>4</b>	<b>Local dispersion analysis in bounded media</b>	<b>55</b>
4.1	Introduction . . . . .	57
4.2	Methods . . . . .	58
4.2.1	Numerical setup . . . . .	58
4.2.2	LPVI analysis. . . . .	59
4.2.3	$f$ - $k$ domain M-line analysis . . . . .	60
4.2.4	Shear modulus estimation . . . . .	60
4.2.5	Shear modulus 2D maps . . . . .	61
4.3	Results . . . . .	61
4.3.1	Validation of LPVI in a plate (flat plate, ARF wave) . . . . .	61
4.3.2	Comparing LPVI and $f$ - $k$ domain M-line at different extraction lengths (flat plate, ARF wave). . . . .	62
4.3.3	LPVI in tapered plates (linearly tapered plate, naturally-induced wave)	
	65	
4.4	Discussion . . . . .	66
4.5	Conclusions. . . . .	68
	References . . . . .	71
<b>5</b>	<b>Multi-parameter Lamb wave inversion</b>	<b>75</b>
5.1	Introduction . . . . .	77
5.2	Setup . . . . .	77
5.2.1	Numerical setup . . . . .	77
5.2.2	Experimental setup . . . . .	78
5.3	Methods . . . . .	78
5.3.1	Dispersion curve extraction . . . . .	78
5.3.2	Curve fitting and error volumes . . . . .	80
5.3.3	Fitting reliability . . . . .	81
5.4	Results . . . . .	82
5.4.1	Error volumes . . . . .	82
5.4.2	Robustness against noise . . . . .	86
5.4.3	Frequency range analysis . . . . .	87
5.5	Discussion . . . . .	89
5.6	Conclusions. . . . .	91
5.7	Appendix: sensitivity analysis. . . . .	93
	References . . . . .	94
<b>6</b>	<b>Conclusions and Discussion</b>	<b>97</b>
6.1	Conclusions. . . . .	98
6.2	Results in context . . . . .	99
6.3	Implications for applications . . . . .	101
6.4	Limitations and future work . . . . .	101
	References . . . . .	104
	<b>Acknowledgements</b>	<b>109</b>
	<b>List of Publications</b>	<b>111</b>
	<b>About the author</b>	<b>113</b>

# SUMMARY

Diastolic heart failure is one of the principal causes of death in Western countries, and there is currently no treatment available; prevention, on the other hand, may be possible, provided an early enough diagnosis. The worsening of diastolic functionality is associated with increased values of cardiac stiffness, which could therefore provide a measurable quantification of the diastolic health of the heart.

Ultrasound imaging technologies can be used to non-invasively record the propagation of small amplitude shear waves propagating in the cardiac muscle. In principle, since the propagation speed of a wave is proportional to the stiffness of the medium in which it travels, ultrasonic shear wave imaging could provide a measure of the stiffness of the heart. However, various features of the heart, such as shape and contractility, complicate the relation between wave speed and stiffness in unknown ways.

This thesis aims at understanding how wave propagation is affected by the temporal behaviour and the varying thickness of the heart muscle, and consequently how ultrasonic images of the propagation should be analysed to correctly convert wave speed into muscle stiffness.

More specifically, **Chapter 1** is meant to introduce the readers to the motivation and the background of this thesis, including a brief explanation of the basic theoretical concepts necessary to understand the work presented in the following chapters.

The first scientific question addressed in this thesis concerns the effects that the temporal behaviour of the heart has on propagating waves. In other words: does the contraction/relaxation of the heart affect shear wave elastography (SWE)? **Chapter 2** investigates the effects of temporal stiffness variations on a one-dimensional (1D) wave by using a combination of analytical, numerical and experimental tools. In particular, this chapter shows that the amplitude and the period of a wave increase proportionally to the relaxation of the medium. These results open up new possibilities for functional imaging of contractile media, although the current resolution of measurement technologies is too low to observe the effects presented in this chapter *in-vivo*.

**Chapter 3** shifts the attention from temporal variations to spatial ones. Specifically, this chapter is dedicated to analysing the effects of thickness variations on low frequency Lamb waves, as are expected to be imaged in the interventricular septum. To isolate the role of thickness, two-dimensional (2D) finite element simulations and experiments on a tissue-mimicking phantom were employed. The results of this study shows that thickness variations introduce an additional source of error in the estimation of the shear modulus based on time-of-flight measurements. Moreover, when analysing waves in tapered plates in the frequency domain, assuming a constant value of thickness can lead to very large errors in the estimation of the shear modulus; considering the thickness to be equal to the average thickness over the measurement area reduces the error.

**Chapter 4** investigates a Local Phase Velocity Imaging (LPVI) analysis that was originally proposed for SWE with application to viscoelastic media, with the goal of determin-

ing whether it can improve the analysis of Lamb waves in the heart. The advantage of this technique would be that of reconstructing Lamb dispersion curves locally, therefore potentially reducing the error caused by assuming a constant thickness over large measurement regions in tapered plates. In this chapter, the LPVI approach is employed to analyse 2D finite element simulations, reconstructing local values of shear modulus within small (4 x 2.7 mm) windows. For comparison, the same analysis is performed on data extracted from short (4 mm long) lines. The LPVI approach is shown to be able to reconstruct 2D maps of shear modulus within an average accuracy of 10 % in flat plates and 20 % in tapered ones. Surprisingly, analysing comparably small lines in the frequency-wavenumber domain yields comparably accurate results, despite it being traditionally understood as a "long space" approach.

Chapters 3 and 4 shared a commonly made assumption that inverting a Lamb dispersion curve is a robust method to estimate material parameters such as the shear modulus. However, it was observed that results can change depending on factors such as the frequency range considered for the inversion. **Chapter 5** is dedicated to analyzing the robustness and the precision of the Lamb wave inversion approach. In this chapter, simulated data and experimental data extracted from a metal pipe are analysed to demonstrate that the sensitivity of each mode to these three parameters depends on the frequency content analysed, as well as on the parameter itself. Moreover, it is shown that the results of inverting either mode are sensitive to noise, and that small variations in the extracted dispersion curve can result in large variations of the estimated material parameter, when multiple parameters are being considered simultaneously.

Finally, a summary of the main achievements of this thesis is presented in **Chapter 6**, together with some recommendations for future research and a brief discussion on the relevance of these results for clinical applications.

# SAMENVATTING

Diastolisch hartfalen is een van de meest voorkomende doodsoorzaken in de westerse wereld, en er is momenteel geen behandeling voorhanden. Een vroegtijdige correcte diagnose kan verdere ontwikkeling van de ziekte potentieel vermijden. Aangezien diastolisch hartfalen gepaard gaat met een verhoogde myocardiale stijfheid, is cardiale stijfheid een interessante parameter om de gezondheidstoestand van het hart te beschrijven.

Beeldvorming op basis van ultrageluid (echografie) stelt ons in staat om de voortplanting van transversale golven in de hartspier niet-invasief te meten. De voortplantingssnelheid van deze golven is gerelateerd aan de stijfheid van het medium waarin de golf zich voortplant. Echter, bepaalde karakteristieken van het hart (zoals vorm en contractiliteit) beïnvloeden deze relatie, waardoor de stijfheid van de hartspierwand niet onmiddellijk kan worden afgeleid uit de voortplantingssnelheid.

Het doel van dit proefschrift is om te begrijpen hoe het temporele gedrag en de variërende dikte van de hartspierwand de golfvoortplanting beïnvloeden, zodat een correcte analyse van de cardiale stijfheid kan worden verkregen.

**Hoofdstuk 1** beschrijft de motivatie en achtergrond van dit proefschrift, waarbij kort de theoretische concepten die nodig zijn om het werk in de volgende hoofdstukken te begrijpen worden toegelicht.

De eerste wetenschappelijke vraag die we in dit proefschrift beschouwen betreft het effect van het temporele gedrag van het hart op de voortplanting van afschuifgolven. Met andere woorden: beïnvloedt de contractie/relaxatie van het hart de shear wave elastografie (SWE)? **Hoofdstuk 2** onderzoekt de effecten van temporele stijfheidsvariëaties op een 1D-golf middels een combinatie van analytische, numerieke en experimentele middelen. Dit hoofdstuk toont aan dat de amplitude en periode van een golf proportioneel stijgen met de relaxatie van het medium. Deze resultaten geven aanleiding tot nieuwe mogelijkheden voor medische beeldvorming van contraherende media, maar de huidige resolutie van de technologie is te laag om de in dit hoofdstuk beschouwde effecten in vivo te meten.

**Hoofdstuk 3** verlegt de focus van temporele naar de ruimtelijke variëaties. Dit hoofdstuk analyseert de effecten van wanddikte-variëaties op laagfrequente Lamb-golven, welke vermoedelijk afgebeeld worden in het ventrikelseptum. Om het effect van wanddikte meer in detail te bestuderen, zijn er 2D eindige-elementensimulaties en experimenten opgezet. De resultaten tonen aan dat de variëaties in de cardiale wanddikte een extra fout introduceren in het schatten van de stijfheid op basis van de time-of-flight metingen. Bij analyses van de golfvoortplanting in taps toelopende platen in het frequentiedomein, kan het aannemen van een constante dikte leiden tot grote fouten in de schatting van de schuifmodulus; de foutmarge wordt verkleind door de dikte gelijk te stellen aan de gemiddelde dikte over het meetoppervlak.

**Hoofdstuk 4** onderzoekt of de analyse van Lamb-golven kan worden verbeterd door het toepassen van Local Phase Velocity Imaging (LPVI), een techniek die normaal gebruikt wordt voor toepassingen in visco-elastische media. Het lokaal construeren van

Lamb-dispersiecurves heeft als mogelijk voordeel dat de fout die gemaakt wordt door een constante dikte van de hartspierwand te veronderstellen geminimaliseerd wordt. Dit hoofdstuk past de LPVI-techniek toe op 2D eindige-elementensimulaties om de stijfheid te reconstrueren in kleine gebieden van 4 x 2.7 mm. Deze resultaten zijn vergeleken met die van de oorspronkelijke analyse toegepast op korte M-lijnen (4 mm in lengte). De LPVI-techniek maakt het mogelijk om 2D beelden van de afschuifmodulus te reconstrueren met een gemiddelde nauwkeurigheid van 10% voor vlakke platen en 20% voor tapse platen. Verrassend genoeg leidt het toepassen van de oorspronkelijke analyse op de korte M-lijnen tot resultaten met vergelijkbare nauwkeurigheid, terwijl deze methode traditioneel wordt toegepast op grotere domeinen.

Hoofdstukken 3 en 4 zijn beide gebaseerd op de veronderstelling dat het inverteren van Lamb-dispersiecurven een robuuste methode is om materiaal-parameters zoals de schuifmodulus te schatten. We observeerden echter dat de resultaten sterk afhangen van bepaalde factoren, zoals het beschouwde frequentiebereik, voor het inverteren van de curve. Het doel van **Hoofdstuk 5** was dan ook om de robuustheid en precisie van de Lamb-golf inversiemethode te bestuderen. Analyse van gesimuleerde en experimentele data van een metalen pijp tonen aan dat de sensitiviteit van elke mode van de materiaal-parameters afhangt van de beschouwde frequentie-inhoud, maar ook van de parameter zelf. De resultaten zijn eveneens zeer gevoelig aan ruis: kleine variaties in de geëxtraheerde dispersiecurve kunnen resulteren in grote variaties in de geschatte materiaal-parameter, wanneer meerdere parameters tegelijkertijd beschouwd worden.

Tenslotte worden de belangrijkste bevindingen van dit proefschrift samengevat in **Hoofdstuk 6**. Hierbij worden ook aanbevelingen voor toekomstig onderzoek gegeven en wordt de relevantie van de resultaten van dit proefschrift met oog op klinische applicatie besproken.

# 1

## INTRODUCTION

## 1.1. HEARTS, HEART FAILURE AND HEART STIFFNESS

The heart performs a role of basic necessity to sustain our lives, that is, pumping blood through our entire body. Impairments to blood circulation can have dire consequences: cardiovascular diseases are in fact the number one cause of death in the world [1]. In particular, heart failure, consisting of the heart being unable to pump enough blood to meet metabolic requirements, is a chronic syndrome with a prevalence of over 23 millions worldwide and a high mortality (45-60% patients die within five years from the diagnosis) [2]. About half of all cases of heart failures consist of diastolic heart failure, which is associated with an impairment of the diastolic phase (i.e. the relaxation) of the left ventricle [3]: due to this diastolic dysfunction, the left ventricle cannot expand adequately to accommodate the influx of blood [4], leading to the inability to increase blood stroke volume and to a large increase of diastolic pressure for even small increases of blood volume [3].

Currently, there is no specific treatment for diastolic heart failure, as its pathophysiology is still poorly understood [5]. Early diagnoses may help in monitoring and understanding the mechanisms behind the development of diastolic heart failure, potentially helping in developing effective treatments. Moreover, addressing early possible risk factors (e.g. hypertension, obesity, smoking [3]), it may be possible to prevent the development of this syndrome in the first place. However, obtaining an early diagnosis is challenging, because symptoms of diastolic heart failure (fatigue, shortness of breath) are absent or hard to detect before the heart's conditions have deteriorated considerably [5]. Moreover, the symptoms themselves are the same as in systolic heart failure, which is related to problems of cardiac contraction and, therefore, require different treatments [6]. Since diastolic dysfunction is an underlying contributor to the development of diastolic heart failure, early detection of the deterioration of diastolic functions could help provide an early diagnosis [5].

To detect diastolic dysfunction, it is necessary to identify some parameter that is informative of diastolic function, that is measurable, and possibly that is quantifiable. Moreover, a non-invasive test would be preferable for the purpose of early detection, as it involves less risks and discomforts for the patient, and it could potentially be performed routinely. Currently, tissue doppler echocardiography and Doppler (blood) flow measurements are the two most commonly used non-invasive techniques in clinical assessment of diastolic dysfunction [5]. However, these techniques measure effects of diastolic impairment (variations in blood flow and tissue mobility), rather than the conditions of the muscle itself. A potentially more informative parameter to assess diastolic dysfunction has been identified in the stiffness of the cardiac muscle: in fact, diastolic dysfunction is associated with an increased left ventricular chamber stiffness [3], and cardiac stiffness has been found to present significantly higher values in patients with diastolic heart failures, compared to healthy hearts [7, 8].

It is useful to note that many studies aimed at measuring cardiac stiffness non-invasively use the term "stiffness" somewhat loosely, generally referring to the intrinsic elastic properties of a material, such as the shear modulus or the Young's modulus [9–17], rather than its actual stiffness, an extrinsic property (e.g. the Young's modulus of an aluminium spring is different from its stiffness). For the purpose of this thesis, the term stiffness will also be used in the loose sense of "resistance to (any) deformation", and the exact intrinsic elastic property considered will be specified where appropriate.

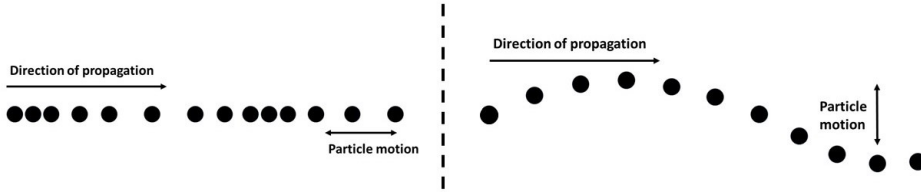


Figure 1.1: Depiction of a longitudinal (left) and a transversal (right) waves.

In general, stiffness is a well understood physical property commonly measured with mechanical tests. While mechanical tests would clearly be inadequate for monitoring the cardiac stiffness of patients, as they would involve invasive, expensive and likely harmful surgeries, it is possible to also measure stiffness non-invasively by exploiting wave physics, for instance by using ultrasounds to perform so-called shear wave elastography (SWE) measurements[9, 10, 14–16].

## 1.2. WAVES IN SOLIDS

### WAVES IN BULK MEDIA AND WAVE PROPERTIES

To understand how ultrasounds can be used to measure non-invasively the stiffness of an organ inside the body, let us first start by briefly discussing waves. A wave is a physical quantity that travels through a medium following a specific law, the wave equation:

$$\frac{\partial^2 u}{\partial t^2} = c^2 \nabla^2 u \quad (1.1)$$

where  $c$  represents the speed at which the quantity  $u$  propagates [18]. A shear wave is a transverse wave in a solid, with the quantity  $u$  perpendicular to the direction of propagation. Possibly the easiest way to visualize a transverse wave is to picture a wave on a string: if we move e.g. up and down one end of the string, the displacement we cause is transmitted across the entire length of the string; the individual particle motion is vertical (as we had applied to the end of the string), but the direction in which the displacement propagates is that of the string, e.g. horizontal. In contrast, a compressional wave is a longitudinal wave in a solid in which the displacement is parallel to the direction of propagation (see Fig. 1.1). The traveling displacement is represented by  $u$  in the equation above, which, in this case, describes how the perturbation we apply to one end of the string propagates to the other.

There are three key features of waves that are important for SWE:

- The first is that the speed  $c$  depends on the material properties of the medium. In the simple case of a bulk elastic solid,  $c_s = \sqrt{(G/\rho)}$ , that is the speed of a shear wave ( $c_s$ ) depends on the density  $\rho$  and the shear modulus  $G$  of the medium. This means that, assuming that one knows the density of the medium, one can reconstruct its shear modulus by measuring the speed of a shear wave.
- The second important feature is that waves are (partially) reflected at the interface between two media with different properties. As a consequence, receiving a re-

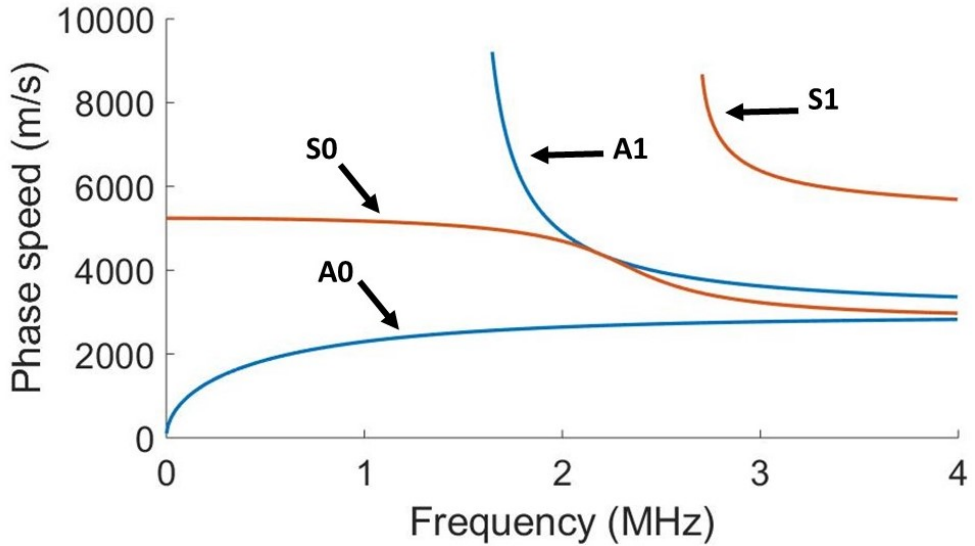


Figure 1.2: The first two symmetric (red) and antisymmetric (blue) Lamb modes, calculated for a 1 mm thick steel plate.

flected signal and knowing the speed of the wave and the time between send and receive, it is possible to derive the location of the interfaces, eventually reconstructing entire images (this is, for instance, the principle behind the echolocation abilities of bats). Moreover, the inhomogeneous structure of many organs (e.g. the myocardial fibers in the heart) also generate diffuse reflections, referred to as scattering, providing a signal from throughout the entire thickness of the organ, rather than just from the surface.

- Finally, a wave consists of the transmission of a perturbation from a particle to its neighbours; as long as the amplitude of this perturbation does not exceed the rupturing limit of the medium, it does not cause any damage to it, making it the ideal tool for non-invasive, non-destructive measurements.

## LAMB WAVES

If the medium in which the wave propagates has a plate-like geometry, i.e. two of its dimensions are considerably larger than the third, boundary effects alter the propagation and the wave is said to be "guided" by the boundaries in the third dimension. This situation was first described by Horace Lamb [19], and guided waves in plates are often referred to as Lamb waves. The theory of Lamb waves treats plates with one finite dimension (the thickness) and two infinite dimensions, in a purely elastic and isotropic medium. While, in principle, such ideal plates do not really exist, Lamb wave theory still gives a good account of wave behaviour in plate-like geometry, and has been successfully applied to non-destructive testing applications in a variety of situations [20–29]. As such, throughout this thesis, the term "Lamb wave" will be used to describe any wave propagating in a plate-like

medium, regardless of deviations from the ideal situation described in the theory.

According to Lamb theory, two infinite sets of propagation modes can be excited when inducing wave propagation in a plate. Each of these modes is classified as either symmetric or antisymmetric, depending on the distribution of  $u$  with respect to the plate thickness; moreover, all the modes within a class are ordered sequentially based on the lowest frequency at which they appear: the zeroth order modes are present at all frequencies, the first order modes are only excited at frequencies higher than a cut-off value  $f_0$ , and so on (see, for instance, Fig. 1.2). Notably, the amplitude distribution of each individual mode in the plate varies as a function of frequency and depth, e.g. an antisymmetric mode, at a given frequency, could have a null amplitude near the surface of the plate, while having a large amplitude halfway through the thickness [30]. Moreover, every mode is associated with a characteristic dispersion curve, i.e. for every mode, the phase speed of a wave depends on its frequency, as well as the plate thickness.

From a SWE perspective, this guided wave behaviour complicates considerably the relation between speed and stiffness, and the relation described above for bulk media does not hold anymore. In order to reconstruct the shear modulus  $G$  when analysing Lamb waves, the dispersion curve of the wave should first be measured, for instance by analysing the propagation data in the frequency-wavenumber domain [12, 22, 23]. Another approach consists in generating several monochromatic waves with different frequencies, and then measuring the phase speed of each wave independently [31]. In any case, the dispersion curve can then be compared to theoretical ones (for which  $G$  is known) with a fitting algorithm, until the best matching curve is identified [12, 22, 23].

### 1.3. ULTRASOUND SHEAR WAVE ELASTOGRAPHY

Ultrasound machines are widely used in clinical practice, as they are a safe, non-invasive, cheap and fast tool to obtain images of the inside of a patient (called echographies). In essence, an ultrasound transducer produces images using the wave properties described in the previous section: an ultrasonic longitudinal sound pulse (i.e. a soundwave with frequencies higher than human hearing range, typically in the order of MHz for clinical transducers) is sent through the body, and the transducer then records the reflected waves generated by the interfaces between organs and by the inhomogeneities of each tissue. Analysing the arrival times of the reflected 'echoes', it is possible to reconstruct an image of the structure that generated them. This approach is referred to as "Pulse-echo" imaging.

Traditionally, the transducer is used to excite focused beams that reconstruct a single line in an image; the focus location is then moved and the acquisition repeated, until the entire image is reconstructed, line by line. This procedure, however, can take tens of milliseconds to reconstruct a single image. Framerates in the order of the kHz can be achieved by using the transducers to transmit plane waves instead, insonifying the entire region of interest with one single pulse [32]. This can be necessary when imaging fast phenomena, such as the propagation of shear waves in the cardiac muscle, which can take place over a time of just a few milliseconds. The cost of the higher framerate is typically a lower spatial resolution and a worse contrast, but this can be improved by compounding few acquisitions at different angles [32].

The idea behind ultrasound SWE, then, is fairly simple: the ultrasound transducer is used to perform pulse-echo imaging of a tissue deformed by a travelling shear wave. By

acquiring a rapid sequence of several images, the propagation of the deformation can be recorded and used to calculate the speed of the wave. Typically, this is done by extracting the tissue motion over time along a single line, which in this thesis will be referred to as M-line (a motion line). Finally, knowing the propagation speed, the elastic properties of the medium (e.g. its shear modulus) can be determined. This approach has already been demonstrated to be successful for several applications [11, 33].

Shear waves analysed in cardiac SWE can have a natural origin, e.g. being generated by the closure of the aortic valve [10, 13, 15, 34, 35]. Alternatively, a shear wave can also be induced by using the transducer to transmit a focused ultrasound beam into the heart muscle, generating a force that pushes on the tissue, the so-called acoustic radiation force [17, 36–38]. Either source can, in principle, be used for SWE.

While the basic idea of ultrasound SWE, as described above, is simple enough, in practice there is a number of challenges that need to be overcome to obtain measurements with diagnostic value for cardiac application. Roughly speaking, these challenges fall into one of three categories: signal acquisition, e.g. how to obtain larger and sharper images; signal processing, e.g. how to identify and track the wave from the images; and data interpretation, i.e. how to correctly translate the wave motion into a measure of stiffness. This thesis investigates questions essentially related to the third category, as explained in the following paragraphs, trying to expand the knowledge necessary to interpret measurements in terms of muscle stiffness.

#### 1.4. HEART MODELLING

While acquiring clear images of wave propagation and accurately reconstructing its space-time trajectory are necessary to perform SWE, they are not sufficient to determine the stiffness of the muscle. In fact, the relation  $c_s = \sqrt{(G/\rho)}$  holds only for a wave traveling in an elastic, homogeneous, isotropic bulk medium. In contrast, the heart muscle is comprised of sheets of muscle fiber with different orientations, i.e. it is anisotropic; it exhibits also viscous behaviours, and is therefore viscoelastic; its thickness can be comparable to the wavelength of shear waves traversing it, breaking down the assumption of bulk material; finally, as the heart performs its pumping function, its properties vary in time with the contraction-relaxation cycle of each heartbeat. Without knowing how each of these effects (and how all of them together) affect the propagation speed that is measured, it is not possible to reliably reconstruct the stiffness of the cardiac muscle.

When performing a SWE measurement, all of the effects described above are present at once, compounded to the intrinsic challenges of data acquisition (e.g. imaging artefacts, noise...). For this reason, it is generally impractical to use experiments to understand how shear waves are affected by any particular feature. A more flexible approach consists of first developing a model, i.e. a simplified description that only contains the features one wants to analyse; the model can then be gradually extended to include more and more features, until it provides a complete description of the phenomenon under investigation. To give a simple example, one might want to understand how a rock moves in free-fall from the surface to the bottom of a sea. The simplest model would describe the free-fall movement in vacuum, where gravity can be understood; in parallel, an experiment could be run to determine the effect of buoyancy in sea water; next, a rock could be let fall in

a water tank filled with sea water, where now gravity and buoyancy are known, to understand the effects of viscous drag; then, the water might be forced to circulate in controlled patterns, to analyse the effect of underwater currents. Depending on what exact information one needs, the model could be further extended by adding new variables, one by one. At the end of this process, a complete description of a free-falling rock in the sea is found. With this description, one can interpret with confidence why the rock landed at a certain location instead of another, and can even make predictions as to where the rock will land next.

According to the definition of model given above, a model could consist of an equation (for example the Maxwell's equations of electromagnetism) or a simplified experiment (such as those presented in chapters 2 and 3 of this thesis). Typically, an equation is the most effective description that can be given, as it represents a mathematical truth about a specific set of conditions; however, most real-world situations are too complex to be described with an exact analytical model. On the other end of the spectrum, simplified experiments can be devised and implemented more easily, but they provide far less control over the phenomenon under investigation (i.e. it is not always possible to truly isolate a single feature), and the results are in any case affected by experimental uncertainty. Yet another approach consists of developing a computational model, where equations that cannot be solved analytically can be approximated numerically. The disadvantage of this approach is that an error in the implementation of the simulation can lead to un-physical results (i.e. wrong results that violate the laws of physics): compared to e.g. experiments, not only the interpretation of the result could be wrong, but the result itself could also be incorrect. For this reason, simulations typically need experimental validation. However, once the numerical implementation of a simulated experiment is validated, it offers results that are free of experimental uncertainty and noise, while also allowing full control over all the parameters included in the model.

A considerable research effort is already directed at modeling the mechanical properties of cardiac tissue. Several studies focus on measuring the shear modulus, the viscoelasticity or the varying fiber orientations of the heart muscle [14, 36, 38–41], while others aim at formulating models to describe such features [42–45]. Fewer studies are concerned with explicitly relating specific cardiac features to SWE measurements, for instance analysing the impact on wave propagation of anisotropy, viscoelasticity and septal finite geometry [12, 46–48].

## 1.5. THESIS GOAL AND OUTLINE

The goal of this thesis is to further the understanding of how different features of the heart muscle impact the analysis and interpretation of shear wave measurements. To achieve this goal, we used a combination of theoretical modeling, *in-vitro* and *in-silico* experiments.

In particular:

**Chapter 2** is dedicated to investigating how the temporal behaviour of the cardiac muscle (i.e. the contractions and relaxations of the heart cycle) affects wave propagation. By using a combination of analytical, numerical and experimental tools, the main physical phenomena affecting a one-dimensional (1D) wave due to the temporal stiffness

variation are explored and discussed in terms of cardiac SWE applications.

In **Chapter 3**, a two-dimensional (2D) model is developed to account for the Lamb wave behaviour expected to take place in the interventricular septum. In particular, finite element simulations and experiments on a tissue-mimicking phantom investigate how Lamb waves are affected by thickness variations as can be present in a human heart. These results are then used to discuss their impact on the accuracy of cardiac SWE, highlighting the need for local measurements of Lamb waves.

**Chapter 4** investigates whether the Local Phase Velocity Imaging (LPVI) analysis, recently proposed for SWE in the liver[49, 50], can also be applied to Lamb wave physics in the heart. In this chapter, the LPVI technique is employed to analyse data obtained from 2D finite element simulations, and it is then compared to the standard combination of M-line data extraction and 2D Fourier transformation, showing that both methods can reconstruct local elastic properties comparably well in a simulated interventricular septum.

**Chapter 5** is dedicated to analyzing the reliability and limits of Lamb wave inversion approaches, which are commonly used (including in chapters 3 and 4 of this thesis) to reconstruct the material properties of a medium from the extracted Lamb curves. In this chapter, simulated data as well as data extracted from experiments on a metal pipe are used to determine the sensitivity of the zeroth-order Lamb modes with respect to compressional speed, shear speed and thickness of a medium, as well as the precision with which these parameters can be extracted.

In **Chapter 6**, the main results of this thesis are summarised and discussed in the perspective of cardiac SWE and clinical applications.

## REFERENCES

- [1] WHO, <https://www.who.int/news-room/fact-sheets/detail/the-top-10-causes-of-death>, (World Health Organization).
- [2] A. L. Bui, T. B. Horwich, and G. C. Fonarow, *Epidemiology and risk profile of heart failure*, (2011).
- [3] R. Gary and L. Davis, *Diastolic heart failure*, Heart and Lung: Journal of Acute and Critical Care **37**, 405 (2008).
- [4] M. R. Zile and D. L. Brutsaert, *New concepts in diastolic dysfunction and diastolic heart failure: Part I: Diagnosis, prognosis, and measurements of diastolic function*, Circulation **105** (2002), 10.1161/hc1102.105289.
- [5] G. D. Plitt, J. T. Spring, M. J. Moulton, and D. K. Agrawal, *Mechanisms, diagnosis, and treatment of heart failure with preserved ejection fraction and diastolic dysfunction*, (2018).
- [6] K. Komamura, *Similarities and differences between the pathogenesis and pathophysiology of diastolic and systolic heart failure*, (2013).

- [7] W. H. Gaasch, H. J. Levine, M. a. Quinones, and J. K. Alexander, *Left ventricular compliance: mechanisms and clinical implications*. The American journal of cardiology **38**, 645 (1976).
- [8] D. Westermann, M. Kasner, P. Steendijk, F. Spillmann, A. Riad, K. Weitmann, W. Hoffmann, W. Poller, M. Pauschinger, H.-P. Schultheiss, and C. Tschope, *Role of Left Ventricular Stiffness in Heart Failure With Normal Ejection Fraction*, *Circulation* **117**, 2051 (2008).
- [9] C. Pislaru, M. Urban, I. Nenadic, and J. Greenleaf, *Shearwave dispersion ultrasound vibrometry applied to in vivo myocardium*, in *2009 Annual International Conference of the IEEE Engineering in Medicine and Biology Society* (IEEE, 2009) pp. 2891–2894.
- [10] C. Pislaru, P. A. Pellikka, and S. V. Pislaru, *Wave propagation of myocardial stretch: Correlation with myocardial stiffness*, *Basic Research in Cardiology* **109** (2014), 10.1007/s00395-014-0438-5.
- [11] J. E. Brandenburg, S. F. Eby, P. Song, H. Zhao, J. S. Brault, S. Chen, and K.-N. An, *Ultrasound Elastography: The New Frontier in Direct Measurement of Muscle Stiffness*, *Archives of Physical Medicine and Rehabilitation* **95**, 2207 (2014).
- [12] A. Caenen, M. Pernot, D. A. Shcherbakova, L. Mertens, M. Kersemans, P. Segers, and A. Swillens, *Investigating Shear Wave Physics in a Generic Pediatric Left Ventricular Model via *In Vitro* Experiments and Finite Element Simulations*, *IEEE Transactions on Ultrasonics, Ferroelectrics, and Frequency Control* **64**, 349 (2017).
- [13] H. J. Vos, B. M. van Dalen, I. Heinonen, J. G. Bosch, O. Sorop, D. J. Duncker, A. F. W. van der Steen, and N. de Jong, *Cardiac Shear Wave Velocity Detection in the Porcine Heart*. *Ultrasound in medicine & biology* **43**, 753 (2017).
- [14] M. Strachinaru, J. G. Bosch, B. M. van Dalen, L. van Gils, A. F. van der Steen, N. de Jong, M. L. Geleijnse, and H. J. Vos, *Cardiac Shear Wave Elastography Using a Clinical Ultrasound System*, *Ultrasound in Medicine and Biology* (2017), 10.1016/j.ultrasmedbio.2017.04.012.
- [15] M. Strachinaru, J. G. Bosch, L. van Gils, B. M. van Dalen, A. F. L. Schinkel, A. F. W. van der Steen, N. de Jong, M. Michels, H. J. Vos, and M. L. Geleijnse, *Naturally occurring shear waves in healthy volunteers and hypertrophic cardiomyopathy patients*, *Ultrasound in medicine & biology* **00**, 1977 (2019).
- [16] L. B. Keijzer, M. Strachinaru, D. J. Bowen, M. L. Geleijnse, A. F. van der Steen, J. G. Bosch, N. de Jong, and H. J. Vos, *Reproducibility of Natural Shear Wave Elastography Measurements*, *Ultrasound in Medicine & Biology* **45**, 3172 (2019).
- [17] O. Villemain, M. Correia, E. Mousseaux, J. Baranger, S. Zarka, I. Podetti, G. Soulat, T. Damy, A. Hagège, M. Tanter, M. Pernot, and E. Messas, *Myocardial Stiffness Evaluation Using Noninvasive Shear Wave Imaging in Healthy and Hypertrophic Cardiomyopathic Adults*, *JACC: Cardiovascular Imaging* **12**, 1135 (2019).

- [18] J. Achenbach, *Wave Propagation in Elastic Solids* (Elsevier, 1973).
- [19] H. Lamb, *On Waves in an Elastic Plate*, Proceedings of the Royal Society A: Mathematical, Physical and Engineering Sciences **93**, 114 (1917).
- [20] Y.-C. Lee and S.-W. Cheng, *Measuring Lamb wave dispersion curves of a bi-layered plate and its application on material characterization of coating*, IEEE Transactions on Ultrasonics, Ferroelectrics, and Frequency Control **48**, 830 (2001).
- [21] J. L. Deán, C. Trillo, Á. F. Doval, and J. L. Fernández, *Determination of thickness and elastic constants of aluminum plates from full-field wavelength measurements of single-mode narrowband Lamb waves*, The Journal of the Acoustical Society of America **124**, 1477 (2008).
- [22] I. Z. Nenadic, M. W. Urban, S. A. Mitchell, and J. F. Greenleaf, *Lamb wave dispersion ultrasound vibrometry (LDUV) method for quantifying mechanical properties of viscoelastic solids*, Physics in Medicine and Biology **56**, 2245 (2011).
- [23] M. Bernal, I. Nenadic, M. W. Urban, and J. F. Greenleaf, *Material property estimation for tubes and arteries using ultrasound radiation force and analysis of propagating modes*, The Journal of the Acoustical Society of America **129**, 1344 (2011).
- [24] M. Sale, P. Rizzo, and A. Marzani, *Semi-analytical formulation for the guided waves-based reconstruction of elastic moduli*, Mechanical Systems and Signal Processing **25**, 2241 (2011).
- [25] J. Foiret, J.-G. Minonzio, C. Chappard, M. Talmant, and P. Laugier, *Combined estimation of thickness and velocities using ultrasound guided waves: A pioneering study on in vitro cortical bone samples*, IEEE Transactions on Ultrasonics, Ferroelectrics, and Frequency Control **61**, 1478 (2014).
- [26] M. Ponschab, D. A. Kiefer, and S. J. Rupitsch, *Simulation-Based Characterization of Mechanical Parameters and Thickness of Homogeneous Plates Using Guided Waves*, IEEE Transactions on Ultrasonics, Ferroelectrics, and Frequency Control **66**, 1898 (2019).
- [27] T. Tran, M. Sacchi, D. Ta, V.-H. Nguyen, E. Lou, and L. Le, *Nonlinear Inversion of Ultrasonic Dispersion Curves for Cortical Bone Thickness and Elastic Velocities*, Annals of Biomedical Engineering **47**, 2178 (2019).
- [28] C. Grünsteidl, T. Berer, M. Hettich, and I. Veres, *Using zero-group-velocity lamb waves to determine thickness and bulk sound velocities of isotropic plates*, in *AIP Conference Proceedings*, Vol. 2102 (2019) p. 050016.
- [29] L. Zhu, X. Duan, and Z. Yu, *On the Identification of Elastic Moduli of In-Service Rail by Ultrasonic Guided Waves*, Sensors **20**, 1769 (2020).
- [30] J. Rose, *Ultrasonic Guided Waves in Solid Media*, Vol. 9781107048 (2014) pp. 1–512.

- [31] J. Ormachea, K. J. Parker, and R. G. Barr, *An initial study of complete 2D shear wave dispersion images using a reverberant shear wave field*, *Physics in Medicine & Biology* **64**, 145009 (2019).
- [32] M. Tanter and M. Fink, *Ultrafast imaging in biomedical ultrasound*, *IEEE Transactions on Ultrasonics, Ferroelectrics, and Frequency Control* **61** (2014), 10.1109/tuffc.2014.6689779.
- [33] G. Ferraioli, C. Tinelli, B. Dal Bello, M. Zicchetti, G. Filice, and C. Filice, *Accuracy of real-time shear wave elastography for assessing liver fibrosis in chronic hepatitis C: A pilot study*, *Hepatology* **56**, 2125 (2012).
- [34] H. Kanai, *Propagation of spontaneously actuated pulsive vibration in human heart wall and in vivo viscoelasticity estimation*, *IEEE Transactions on Ultrasonics, Ferroelectrics, and Frequency Control* **52**, 1931 (2005).
- [35] P. Santos, A. M. Petrescu, J. Pedrosa, M. Orłowska, V. Komini, J.-U. Voigt, and J. D'hooge, *Natural Shear Wave Imaging in the Human Heart: Normal Values, Feasibility, and Reproducibility*, *IEEE Transactions on Ultrasonics, Ferroelectrics, and Frequency Control* **66**, 442 (2019).
- [36] M. Couade, M. Pernot, E. Messas, A. Bel, M. Ba, A. Hagege, M. Fink, and M. Tanter, *In Vivo Quantitative Mapping of Myocardial Stiffening and Transmural Anisotropy During the Cardiac Cycle*, *IEEE Transactions on Medical Imaging* **30**, 295 (2011).
- [37] M. Pernot, W.-N. Lee, A. Bel, P. Mateo, M. Couade, M. Tanter, B. Crozatier, and E. Messas, *Shear Wave Imaging of Passive Diastolic Myocardial Stiffness*, *JACC: Cardiovascular Imaging* **9**, 1023 (2016).
- [38] P. Song, X. Bi, D. C. Mellema, A. Manduca, M. W. Urban, J. F. Greenleaf, and S. Chen, *Quantitative Assessment of Left Ventricular Diastolic Stiffness Using Cardiac Shear Wave Elastography*, *Journal of Ultrasound in Medicine* **35**, 1419 (2016).
- [39] E. D. Verdonk, S. A. Wickline, and J. G. Miller, *Anisotropy of ultrasonic velocity and elastic properties in normal human myocardium*, *J Acoust Soc Am* **92**, 3039 (1992).
- [40] C. Pislaru, M. W. Urban, S. V. Pislaru, R. R. Kinnick, and J. F. Greenleaf, *Viscoelastic properties of normal and infarcted myocardium measured by a multifrequency shear wave method: Comparison with pressure-segment length method*, *Ultrasound in Medicine and Biology* **40**, 1785 (2014), arXiv:NIHMS150003 .
- [41] I. Z. Nenadic, M. W. Urban, C. Pislaru, D. Escobar, L. Vasconcelos, and J. F. Greenleaf, *In vivo open- and closed-chest measurements of left-ventricular myocardial viscoelasticity using lamb wave dispersion ultrasound vibrometry (LDUV): A feasibility study*, *Biomedical Physics and Engineering Express* **4** (2018), 10.1088/2057-1976/aabe41.
- [42] G. A. Holzapfel and R. W. Ogden, *Constitutive modelling of passive myocardium: a structurally based framework for material characterization*, *Philosophical Transactions of the Royal Society A: Mathematical, Physical and Engineering Sciences* **367**, 3445 (2009).

- [43] T. C. Gasser and C. Forsell, *The numerical implementation of invariant-based viscoelastic formulations at finite strains. An anisotropic model for the passive myocardium*, Computer Methods in Applied Mechanics and Engineering **200**, 3637 (2011).
- [44] T. S. E. Eriksson, A. J. Prassl, G. Plank, and G. A. Holzapfel, *Influence of myocardial fiber/sheet orientations on left ventricular mechanical contraction*, Mathematics and Mechanics of Solids **18**, 592 (2013).
- [45] O. Gültekin, G. Sommer, and G. A. Holzapfel, *An orthotropic viscoelastic model for the passive myocardium: continuum basis and numerical treatment*, Computer methods in biomechanics and biomedical engineering **19**, 1647 (2016).
- [46] M. W. Urban, B. Qiang, P. Song, I. Z. Nenadic, S. Chen, and J. F. Greenleaf, *Investigation of the effects of myocardial anisotropy for shear wave elastography using impulsive force and harmonic vibration*, Physics in Medicine and Biology **61**, 365 (2015).
- [47] A. Caenen, D. Shcherbakova, B. Verheghe, C. Papadacci, M. Pernot, P. Segers, and A. Swillens, *A versatile and experimentally validated finite element model to assess the accuracy of shear wave elastography in a bounded viscoelastic medium*, IEEE Transactions on Ultrasonics, Ferroelectrics, and Frequency Control **62**, 439 (2015).
- [48] A. Gregory, M. Bayat, M. Denis, M. Mehrmohammadi, M. Fatemi, and A. Alizad, *An experimental phantom study on the effect of calcifications on ultrasound shear wave elastography*, Proceedings of the Annual International Conference of the IEEE Engineering in Medicine and Biology Society, EMBS **2015-Novem**, 3843 (2015).
- [49] P. Kijanka and M. W. Urban, *Local Phase Velocity Based Imaging: A New Technique Used for Ultrasound Shear Wave Elastography*, IEEE Transactions on Medical Imaging **38** (2019), 10.1109/TMI.2018.2874545.
- [50] P. Kijanka and M. W. Urban, *Local Phase Velocity Based Imaging (LPVI) of Viscoelastic Phantoms and Tissues*, IEEE Transactions on Ultrasonics, Ferroelectrics, and Frequency Control (2020), 10.1109/tuffc.2020.2968147.

# 2

## MODELING WAVE PROPAGATION IN TEMPORALLY RELAXING MEDIA FOR CARDIAC SHEAR WAVE ELASTOGRAPHY

---

Parts of this chapter have been published in the Journal of the Acoustical Society of America, 2020, 147(5), pp. 3091-3099, "*Fundamental modeling of wave propagation in temporally relaxing media with applications to cardiac shear wave elastography*", **A. Sabbadini**, L.B.H. Keijzer, H.J. Vos, N. de Jong, and M.D. Verweij

## Abstract

Shear wave elastography (SWE) might allow non-invasive assessment of cardiac stiffness by relating shear wave propagation speed to material properties. However, after aortic valve closure, when natural shear waves occur in the septal wall, the stiffness of the muscle decreases significantly, and the effects of such temporal variation of medium properties on shear wave propagation have not been investigated yet. The goal of this work is to fundamentally investigate these effects. To this aim, qualitative results were first obtained experimentally using a mechanical setup, and were then combined with quantitative results from finite difference simulations. The results show that the amplitude and period of the waves increase, during propagation, proportionally to the relaxation of the medium, and that reflected waves can originate from the temporal stiffness variation. These general results, applied to literature data on cardiac stiffness throughout the heart cycle, predict as a major effect a period increase of 20% in waves propagating during a healthy diastolic phase, whereas only a 10% increase would result from the impaired relaxation of an infarcted heart. Therefore, cardiac relaxation can affect the propagation of waves used for SWE measurements and might even provide direct information on the correct relaxation of a heart.

## 2.1. INTRODUCTION

Cardiac diseases are a major cause of death in developed countries. Early diagnoses might help prevent the development of life-threatening conditions by detecting signs of deterioration before cardiac functionality becomes compromised. Such diagnoses may be obtained by monitoring the stiffness of the cardiac muscle, which has been observed to correlate with the health condition of the heart [1–3]. In order to monitor the material properties of the heart, however, non-invasive techniques must be employed, as invasive measurements are highly uncomfortable and potentially harmful for patients.

Shear Wave Elastography (SWE) exploits wave propagation phenomena to explore the elastic properties of a material, and it has already been proven to be a viable tool in clinical applications [4–7]. Its application to cardiac settings, however, is hindered by a challenge intrinsic to the functioning of the heart: the heart cycle.

As the heart performs its pumping function, its stiffness increases and decreases cyclically to allow for the heart chambers to fill with blood and expel it. Aortic valve closure, which provides one of the sources of waves that can be employed for cardiac SWE [8–13], takes place at the beginning of the isovolumic relaxation of the muscle; due to the muscle relaxation, the waves generated at this time could experience a change in propagation speed of  $\approx 15\%$  in just 10 ms (estimated based on the stiffness variation measured in isolated perfused rabbit hearts [14]). While SWE performed on waves naturally occurring in the heart could be more precisely called "natural" SWE, we will refer to it simply as SWE, because the phenomena involved are similar to those of shear waves from non-natural sources (e.g. acoustic radiation force pushes).

Several models are employed in literature to describe the mechanical properties of the cardiac tissue [15–18], however, to the best of our knowledge, all the models employed for elastography assume the mechanical properties of the medium to be constant or, at most, slowly varying [19] in the timescales of the propagating wave. This assumption may hold true for mechanically inactive organs, yet its validity is questionable in the context of SWE measurements performed during diastolic relaxation.

In fact, the existence of measurable effects of time-varying medium properties on propagating waves has already been established in the field of electromagnetism, with theoretical descriptions of media changing smoothly or instantaneously [20–27]. These studies predict that a wave that propagates at varying speed (i.e. in a medium with temporally varying dielectric or magnetic constant) is subjected to a variation in amplitude and oscillation period; additionally, reflected waves are generated at time-discontinuities of the medium, similarly to what happens at the spatial interface of two media. Experimental studies [20, 28] confirmed the predictions regarding amplitude and frequency changes by observing magnetic waves propagating in media subjected to an externally modulated magnetic field. To the best of our knowledge, reflected waves were not observed experimentally. It remains an open question whether these effects are present also in elastic waves, and whether they should be taken into account while performing cardiac elastography.

The goal of the present study is to observe and describe the effects that a temporally varying propagation speed has on mechanical waves, in order to assess their relevance to shear wave elastography of the heart. While a live heart itself could be in principle used as a medium to perform these studies, it would be impractical, since its complicated geome-

try and material properties would make it hard to reliably isolate and identify the specific effects of temporal variations. For this reason, we have chosen to model a simplified setting in which speed variations represent the only complication to 1D wave propagation. We have developed an experimental setup consisting of rotating metal rods suspended by nylon wires (a wave machine), in which the tension can be controlled in real time to alter propagation speed. The rotational displacement of the rods can then travel through the setup as a 1D torsional wave with varying speed. Moreover, we developed finite difference simulations that describe these phenomena numerically. We employed the setup to obtain a first, qualitative confirmation that mechanical waves can also be affected by variations over time of medium properties. The simulation, on the other hand, allowed us to investigate quantitatively how the time-dependent effects are related to the dynamical parameters of the system, i.e. the amount of speed variation and the rate at which this happens.

We apply our findings to data on rabbit hearts [14] to predict the effects of muscle relaxation on cardiac elastography measurements, and we discuss their relevance and possible applications as a new diagnostic tool.

## 2.2. SETUP

### THE WAVE MACHINE

We have built a modified Wave Machine [29] in which the speed of the wave can be controlled during propagation by means of tension variations. As shown in Fig. 2.1, the setup consists of two wooden frames, placed at 3.63 m from each other, that support three wires on which 32 aluminum rods are suspended. Each rod is 60 cm long and has a 1 cm x 1 cm square cross-section. The central wire is made of steel and runs through a hole in the midpoint of the long side of the rod, providing a pivot around which the rods can rotate freely; bolts are fixed to the central wire before and after each rod, to prevent them from translational movements. The other two wires, symmetrically placed at both sides of the steel wire, are made of nylon and can freely slide through their holes in the rods, so that stretching of these wires does not cause translation of the rods. The nylon wires provide the restoration force that opposes rotational displacements from the mutual angular position of the rods. During experiments, the amplitude of the applied perturbation had a gaussian-like shape, as this was the easiest to produce by hand. When a rotational perturbation is applied to one of the rods, it propagates along the setup through the nylon wires, effectively creating a discretized one-dimensional torsional wave. This system can be seen as a discrete approximation of the continuous case in which the distance between two consecutive rods approaches zero. For our case the propagation of the torsional wave can approximately be described by the wave equation

$$\frac{2r^2 FL}{IN} \frac{\partial^2 \theta}{\partial z^2} = \frac{\partial^2 \theta}{\partial t^2} \quad (2.1)$$

where  $r = 0.060 \pm 0.001$  m is the distance between steel and nylon wires,  $F$  is the variable tension in each wire,  $L = 3.410 \pm 0.005$  m is the distance between the two extremal rods,  $I = 0.0049 \pm 0.0004$  kg·m<sup>2</sup> is the moment of inertia of a rod,  $N = 32$  is the total number of

rods and  $\theta$  is their angular displacement. This yields a torsional wave speed

$$c = \sqrt{\frac{2r^2 FL}{IN}} \quad (2.2)$$

2

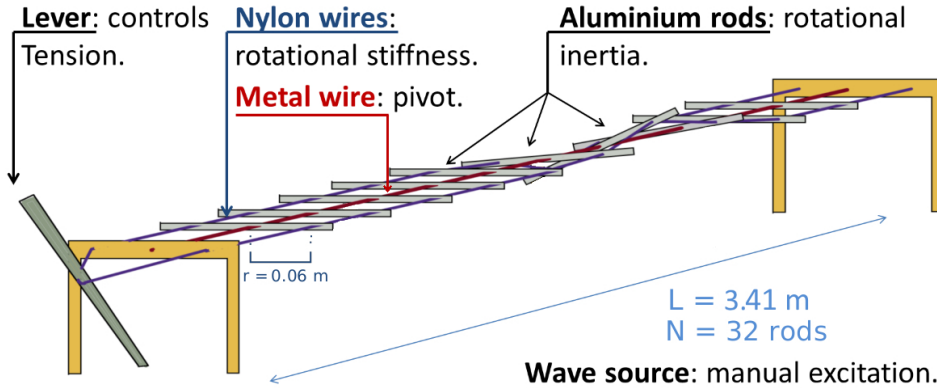


Figure 2.1: Experimental setup: the central wire (red) provides the pivot around which the bars rotate; the two nylon wires (blue) provide the restoration force to enable waves. The lever can be used to control tension in the wires.

### TENSION CONTROL

The tension in the wires could be manually controlled, during experiments, by means of a mechanical lever connected to the nylon wires: pulling the lever would result in stretching of the wires, with a consequent increase in tension. Relaxation of a muscle can be mimicked by pre-stretching the wires, then releasing the lever over a transition time  $\tau$  during wave propagation; with a framerate of 60 frames per second, it was not possible to determine  $\tau$  from the video recordings.

To verify the reliability of Eq. 2.2, a first experiment was run with a force gauge (Force Gauge TMT-5020, OCS.tec GmbH & Co. KG, Neuching, Germany) connected to one end of the nylon wire, so as to compare the values of  $c$  derived from the equation and those measured directly. During this experimental validation, the tension read by the force gauge was  $F = 13.75 \pm 0.2$  N, corresponding to a calculated speed of  $c = 1.50 \pm 0.14$  m/s, a value comparable, within the experimental tolerance, with the speed measured directly from the video recordings,  $c = 1.65 \pm 0.02$  m/s. While the value of speed determined from the tension measurement suffered from a relatively high experimental uncertainty, the uncertainty of the direct speed measurement depends essentially on the framerate of the recording, allowing for more precise measurements. In our experiments, therefore, the propagation speed was measured by acquiring and analysing video-recordings of the wave. Although not necessary, the tension of the pre-stretched nylon wires could be estimated from the speed measurements via Eq. 2.2: with a speed  $c_1 = 3.00 \pm 0.02$  m/s, the

tension was estimated to be  $57.0 \pm 0.1$  N. With the lever in its rest position, on the other hand, the wave travelled at a measured speed of  $c_2 = 1.40 \pm 0.02$  m/s, corresponding to a tension of  $F = 12.4 \pm 0.1$  N.

## 2

### DATA ACQUISITION

A digital single lens reflex camera (Nikon D5300, Nikon Corporation, Tokyo, Japan) with framerate of 60 frames per second, facing the cross section of the rods, was used to record the propagating wave from one side, with a field of view of approximately 2 m that allowed the imaging of 18 rods in the center of the setup. In order to increase the contrast between the setup and the background, the tips of the rods were painted with an orange phosphorescent paint that reacts to ultraviolet (UV) light. We performed the experiments in a dark room illuminated only by 5 UV 60-W lamps, so that the bright orange glow of the extremities of the rods would be easily distinguishable from the background. This allowed us to isolate and track their motion in post-processing, using the software ImageJ (National Institute of Health, Bethesda, Maryland, U.S.) to isolate the motion of each individual bar, and then importing all data in Matlab (version r2016b, MathWorks, Natick, MA, U.S.A.). Frames of the recorded propagating wave are shown in Fig. 2.2, while Fig. 2.3 shows a single videoframe and its numerical reconstruction.

### 2.3. RESULTS

During the experiments, the nylon wires were first pre-stretched to the maximum tension of 57 N. A single unipolar wave pulse was then manually generated by perturbing the first metal rod, and the tension was subsequently dropped to 12.4 N by releasing the lever during propagation. In order to avoid the superposition of boundary reflections with the waves we wanted to study, the release of the lever was timed so that the waveform would always be in the center of the system when the tension dropped. The tension drop happens in a fraction of a period. Fig. 2.4 shows the propagation measured during an experiment: the axes represent the time elapsed and the spatial coordinates of each rod expressed by rod number; due to the limited field of view of the camera, the extremal rods were not imaged and therefore do not appear in the plot. The color scheme represents the amplitude of rotation of each bar, so that the bright yellow 'bands' essentially correspond to the positive forward traveling wave. At time  $t \approx 1.5$  s the effects of the tension drop can be seen. A reflected wave appears as the broad band that moves backwards from right to left, with its negative amplitude represented in dark blue. In addition, broadening of the waves in the vertical (time) direction represent an increased time-period, and their increased brightness indicates a growth in amplitude.

We note a remarkable similitude with the behaviour of waves crossing the spatial discontinuity between two media, the main difference being that, in the case of a temporal discontinuity, it is wavelength that is conserved, while the period changes. In order to better understand the parallelism, let us look at a wave equation in which the wave speed depends on the spatial coordinate

$$c^2(z) \frac{\partial^2 \theta}{\partial z^2} = \frac{\partial^2 \theta}{\partial t^2} \quad (2.3)$$

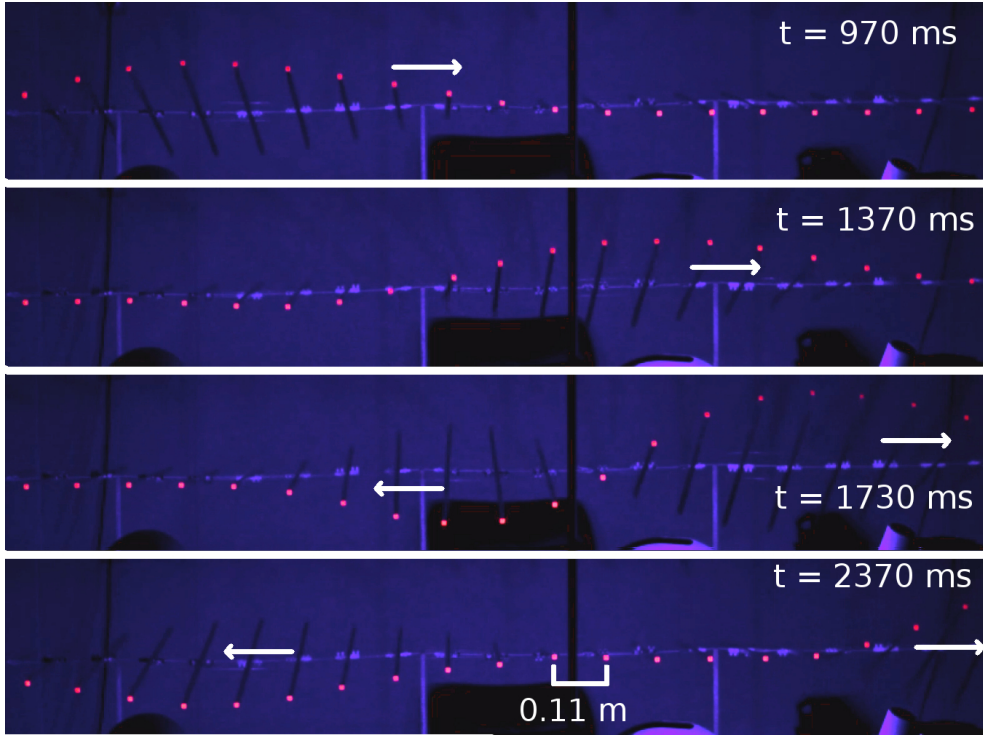


Figure 2.2: Snapshots in time of a wave propagating in the experimental setup. From  $t = 1730$  ms onwards, a reflected wave can also be seen propagating backwards.

Next, we consider the current situation, in which the wave speed depends on time, giving the equation

$$c^2(t) \frac{\partial^2 \theta}{\partial z^2} = \frac{\partial^2 \theta}{\partial t^2} \quad (2.4)$$

By defining a new parameter  $s(t) = 1/c(t)$  called *slowness*, we can rewrite the equation as

$$s^2(t) \frac{\partial^2 \theta}{\partial t^2} = \frac{\partial^2 \theta}{\partial z^2} \quad (2.5)$$

This resembles Eq. 2.3, but with the roles of  $z$  and  $t$  being interchanged.

From the wave behaviour at a spatial discontinuity, it is known that the spatial period of the wave (i.e. the wavelength) varies proportionally to  $c$ , whereas its temporal period remains constant. By considering Eq. 2.5 and performing the same reasoning as above, that is inverting the roles of space and time, we can expect that at a temporal discontinuity the time period will vary proportionally to  $s$ , whereas the spatial period will remain constant.

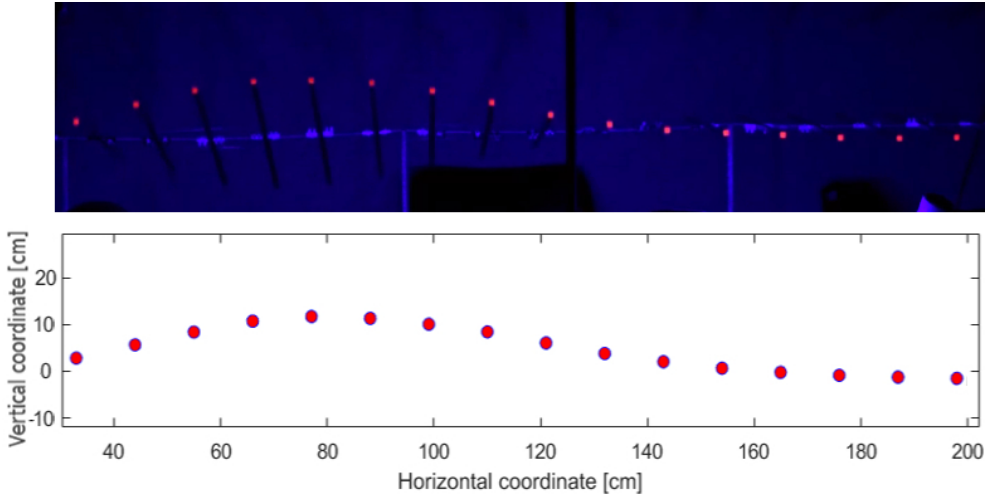


Figure 2.3: Snapshot of the wave propagating in the setup (above) and reconstructed points after image processing (below).

We then proceeded to implement in Matlab a 1D first order explicit Finite Difference scheme to solve Eq. 2.1 numerically and simulate the behavior of the setup in different circumstances. In order to test the viability of the simulation to investigate these phenomena, we compared its results with experimental data: the parameters of the wave function, the space and the time discretizations were all chosen to match those of the experimental setup, i.e. spatial steps of 11 cm (the distance between rods) and time steps of 16 ms (the time between video-frames). The wave was simulated as a Gaussian pulse with an  $e^{-1}$  width of 0.3 s. A comparison between this function and the excursion of the third rod (the first one to be imaged in our measurements) is shown in Fig. 2.5.

Figure 2.6 shows a comparison between simulation and experiment, by plotting the amplitude over time of two rods. The rods were chosen so that one would oscillate once before the tension lever was released, while the other would be crossed by the wave only after the sudden tension drop, which was simulated to happen in 16 ms, i.e. one time-step. The results of the simulation (solid line in Fig. 2.6) are in qualitative agreement with the experiment in terms of amplitudes and period of the incident, transmitted and reflected wave around the transition phase. This validates our numerical approach. Having thus established its reliability, we continued our study by performing simulations only, in order to perform a systematic, quantitative study.

First, we ran simulations to determine the relation between the deceleration of the wave and the formation of transmitted and reflected waves. We computed the behavior of a 1-cycle, sinusoidal wave as could be generated on a 1D string. The spatial discretization was refined to a spacing of 0.01 m to increase spatial sampling of the waves, and the time discretization was shortened to steps of 0.1 ms, ensuring stability of the numerical scheme (Courant number  $C_{num} \leq 0.028$ ) as well as correct sampling of all phenomena. Fig. 2.7 shows how the amplitude and period of the transmitted and the reflected waves change as a function of  $c_1/c_2$ , for fixed duration  $\tau = 10$  ms of the deceleration. We can see that

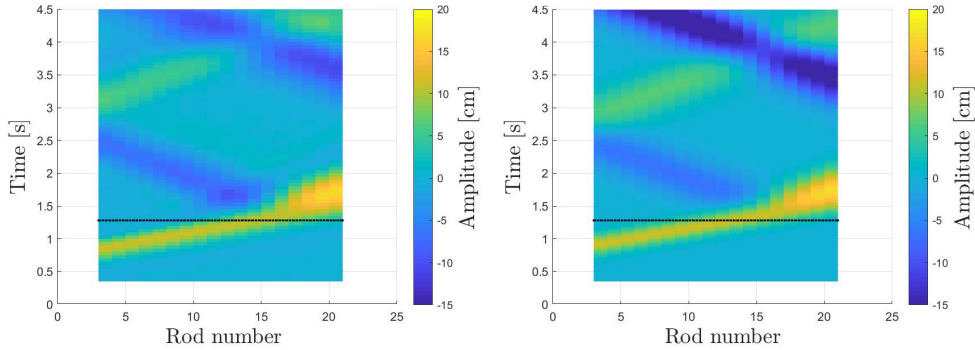


Figure 2.4: Experimental (left) and simulated (right) wave propagation in space-time. The color map represents the amplitude of the rotation of the bars: the bright yellow 'band' shows the waves with positive amplitude, the darker areas correspond to reflected waves with negative amplitude, while the brightening and the broadening in the vertical direction, starting around  $t = 1.5$  s, represent the period and amplitude increase, respectively. The dotted line shows the time at which the tension in the system is suddenly dropped.

both amplitude and period increase linearly with the ratio between the initial and final propagation speed ( $c_1$  and  $c_2$ , respectively), in agreement with the relations  $A_T/A_I = (c_2 + c_1)/2c_2$  and  $A_R/A_I = (c_2 - c_1)/2c_2$  detailed in the Appendix, and the relation  $T = c/\lambda$  with constant wavelength  $\lambda$ ; here,  $A$  represents the amplitude of the wave,  $T$  the period, and the subscripts  $I$ ,  $R$ , and  $T$  represent the initial, reflected, and transmitted waves, respectively. When referring to the period of the wave before and after the tension drop, the subscripts 1 and 2 will be used, so that the two periods will be indicated by  $T_1$  and  $T_2$  respectively.

Furthermore, we investigated the effects of a deceleration taking place over longer spans of time, up to about twice the period of the wave. In our numerical model, for  $t < t_1$  the speed was 3 m/s; the speed then decreased linearly from 3 to 1 m/s, between  $t_1$  and  $t_2 = t_1 + \tau$ , and was consequently kept at a constant value of 1 m/s for  $t > t_2$ . As shown in Fig. 2.8, as the ratio  $\tau/T_1$  between transition time and wave period increases, the amplitude of transmitted and reflected wave decreases; the phase of the reflected wave appears to be opposite of that of the incident wave. Moreover, we can also notice that two reflected waves are actually present when  $\tau/T_1 \geq 1$ , whereas for shorter transition times there appears to be only one, albeit distorted, reflected wave. The variation in period of the wave does not seem to be affected by  $\tau$ , as shown in Fig. 2.9. Based on the results of these simulations, we conclude that reflected waves are generated at points in time when the acceleration of the wave is discontinuous; if two such points are separated by less than  $T_1$ , two reflected waves will be generated, but they will partially overlap with each other, appearing to be a single, distorted waveform. On the other hand, if the distance in time between the two points is greater than  $T_1$ , both distinct waveforms will be visible.

The results of the simulations detailed above offer an overview of the general effects that the temporal variation of a medium has on a propagating wave. In order to assess the relevance of these effects for cardiac SWE, we can input in our model realistic values of stiffness variation of the cardiac muscle to predict how the relaxation would affect a propagating shear wave. Let us first consider the diastolic phase of a heart in which the muscle

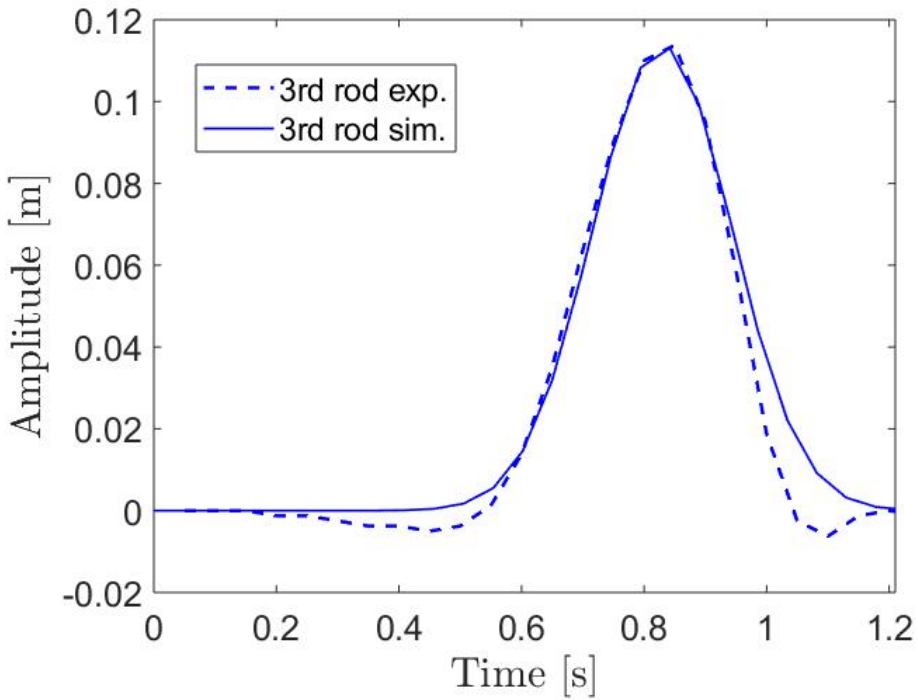


Figure 2.5: Comparison between the experimentally measured excursion of the third metal rod and the gaussian pulse used in the simulation as source of the wave.

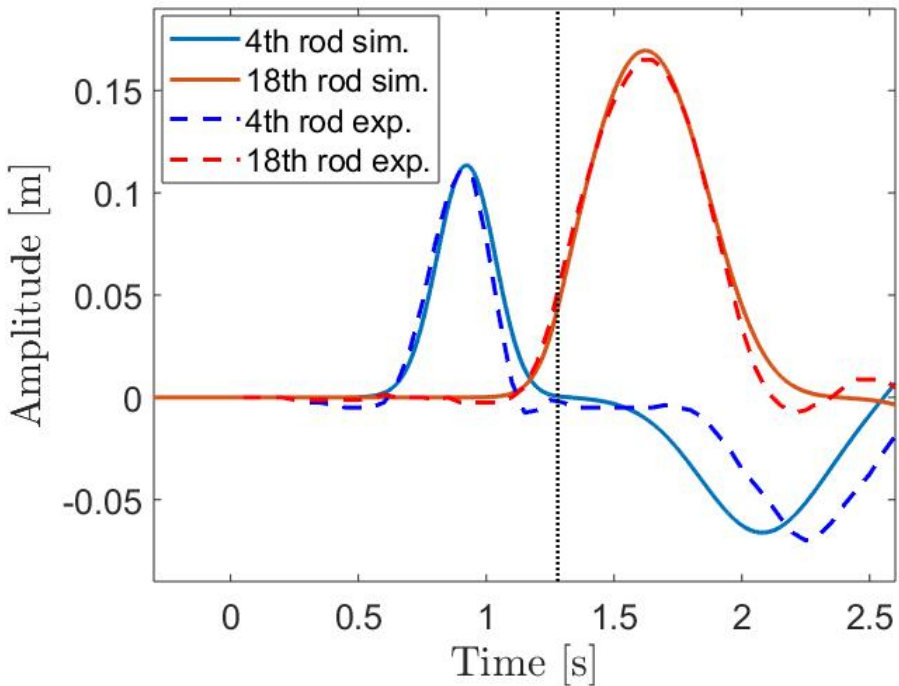


Figure 2.6: Comparison between simulation and experiment in the oscillation of two rods, reached by the wave-front respectively before and after the tension drop. The drop occurs at the time indicated by the vertical dotted line.

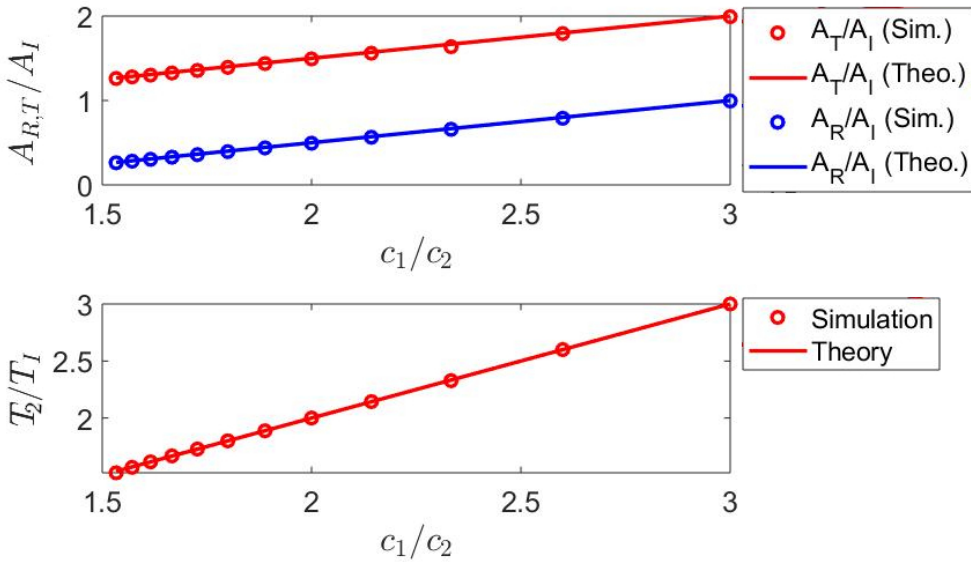


Figure 2.7: Amplitude ratios  $A_{R,T}/A_I$  and period ratios  $T_2/T_1$  as function of  $c_1/c_2$ . Both amplitude and period can be seen to increase linearly with the decrease in speed. The blue curve shows the absolute value of the amplitude of the reflected wave, which, for a decelerating propagation, would be negative.

isovolumic relaxation phase can be modeled by an exponential decrease in stiffness with time constant  $\alpha = 50$  ms, as was measured in Langendorff perfused rabbit hearts [14]. Let us further consider that a shear wave traveling through the muscle is imaged (e.g. by means of ultrasound scanners) for a duration of  $\delta = 10$  ms during this phase. Fig. 2.7 and Fig. 2.9 showed that the variation in period of the wave depends only on the ratio between initial and final speed,  $T_2/T_1 = c_1/c_2$ . The ratio itself can be easily computed knowing  $\alpha$  and the  $\delta$ , since  $c_1/c_2 = e^{\delta/2\alpha}$ . Considering  $\alpha = 50$  ms and  $\delta = 10$  ms, one could expect to observe an increase in wave period of 20%. On the other hand, an infarcted heart might have a relaxation constant  $\alpha = 100$  ms [14]; under the same measuring conditions, one would then observe an increase in wave period of just 10%. Therefore, when reconstruction of the shear wave in space-time domain is possible, the broadening of the tracked shear wave in time could be used as an indirect measure of the relaxation that took place. The amplitude variation, however, being in the order of 3% and 2% for healthy and unhealthy hearts respectively, would be unlikely to be detected in realistic measurements.

## 2.4. DISCUSSION

Our results confirm that mechanical waves show a response to temporal variations of the medium comparable to the behavior of electromagnetic waves detailed in literature: the amplitude and the period of the traveling wave increase proportionally to the decrease in propagation speed, the wavelength is unaffected, and reflected waves can be generated at points of discontinuity in the acceleration.

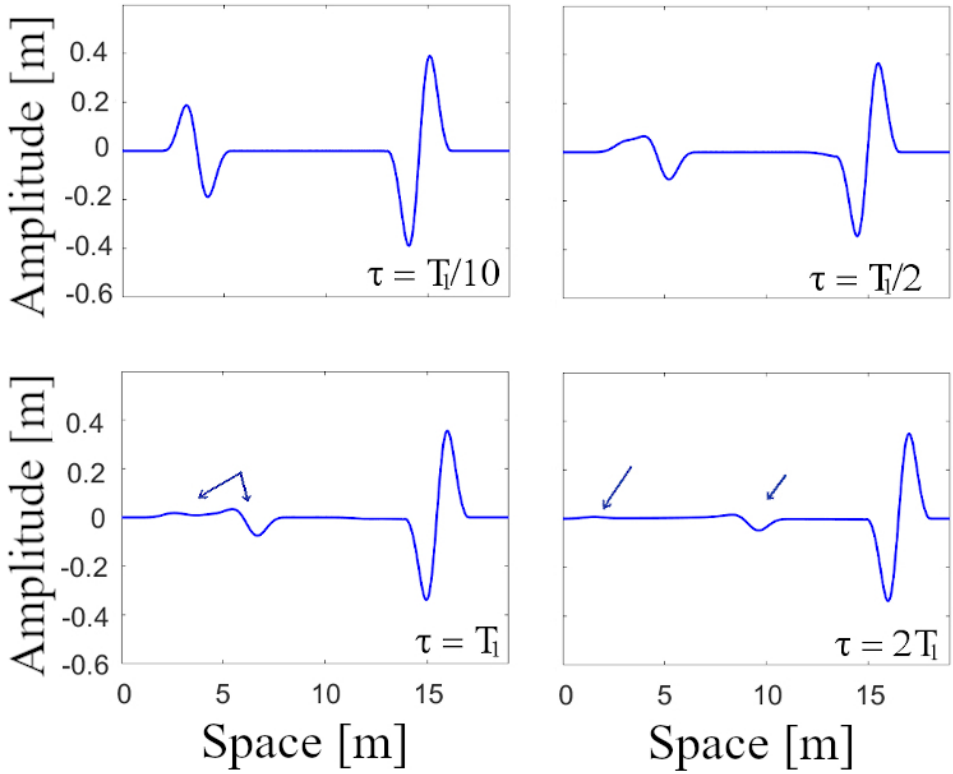


Figure 2.8: Snapshots of a wave after having propagated in a slowly relaxing medium, for different relaxation times  $\tau$ . We can observe that the amplitudes decrease with increasing  $\tau$ , and that a second reflected wave appears when  $\tau/T_1 > 1$ . The arrows point at the two reflected waves.

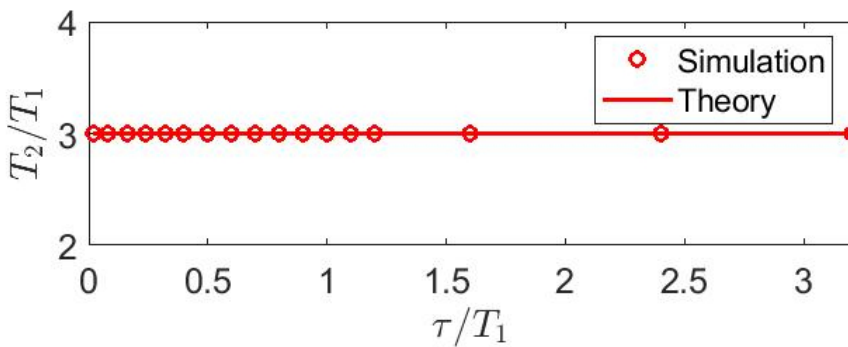


Figure 2.9:  $T_2/T_1$  as function of deceleration time  $\tau/T_1$ . The period of the wave is unaffected by the relaxation time  $\tau$ .

Based on our numerical results, the predicted effects of cardiac relaxation are of particular interest: in fact, not only would a measured wave be affected by the relaxation of the muscle, it would actually be affected by the specific relaxation curve within the measurement. In other words, if two muscles relax at different rates, they may in principle be told apart by observing the variation in amplitude and period of waves traveling through them. The variations in period, in particular, could potentially be employed to directly help diagnoses of diastolic impairment (i.e. reduced muscle relaxation), which is connected to diastolic heart failure. It should be noted that these results show a relation between initial and final period (or frequency), without any assumption about the initial value itself; therefore, the results are independent of the frequencies involved, and can apply to the frequency ranges typical of naturally occurring shear waves, as well as artificially induced ones.

As promising as these results may be, however, their practical implementation still presents challenges. First of all, the amplitude increase caused by diastolic relaxation is expected to be small and could be hard to measure during *in-vivo* experiments, due to signal attenuation and noise. Moreover, because the relaxation of the muscle happens smoothly, there are no discontinuities to give rise to clearly observable reflected waves. Therefore, the only effect of temporal variations to be visible in clinical measurements may be the shift in wave period, and measurements with high time-resolution could be necessary to distinguish the different shifts of a healthy and a diseased heart. For example, for an initial frequency of 50 Hz, the time difference between an increase in the period by 10% and 20% is 2 ms, corresponding to a minimum imaging framerate of 500 Hz, while an initial frequency of 100 Hz would require a minimum framerate of 1000 Hz to discern the different period increases. Finally, due to the anisotropic, viscoelastic, three-dimensional nature of the heart, additional effects will compound to those produced by muscle relaxation, so that more complex models will be required in order to analyze data accurately.

Another matter to be noted is that the results presented in this study only show explicitly the effects of a wave that is generated before the relaxation begins; the relaxation of the medium takes place entirely during the propagation of the wave, and the effects are determined after the entire process has ended. However, when the closure of the aortic valve generates a wave, the cardiac muscle has already started relaxing; moreover, a SWE measurement based on such a wave would be over well before the cardiac relaxation process ended. Therefore, one could question whether the predictions formulated for real hearts can truly be trusted based solely on our numerical study. We argue that this is indeed the case: Fig. 2.7 and Fig. 2.9 show that the variation in period of the wave depends only on the ratio between initial and final speeds  $c_1/c_2$ , where  $c_1$  and  $c_2$  correspond to the speed of the wave at the beginning and at the end of a measurement; this means that, for fixed  $c_1/c_2$ , the variation in period will always be the same, regardless of whether the speed varies with a step function or a smooth curve. As mentioned above, the difference with our simulations, introduced by the smoothness of the diastolic relaxation, lies in the absence of reflected waves, which are generated at discontinuities. It is important to notice that, during a fixed measuring time, different relaxation curves (as could characterize healthy and diseased hearts) will result in different values of  $c_1/c_2$ , therefore affecting the propagating wave differently.

Finally, we consider a wave produced by mitral valve closure, which may also be used

to perform SWE. The mitral valve closes at the onset of systole, the contracting phase of the heart cycle, and, due to the stiffening of the muscle, waves traveling during this phase experience an increase in propagation speed. Based on our results, we expect that the amplitude and period of an accelerating wave will decrease proportionally to the increase in speed, and reflected waves will be once again generated at discontinuities in the acceleration.

From an experimental point of view, compared with other approaches proposed in literature to investigate waves in temporally varying media, the use of our setup shows several advantages. To begin with, the setup allows to observe the full phenomenon in its complexity, including not only the initial and final state of the wave, but its transition phase as well. Moreover, it can be easily built and modified so as to tailor the wave parameters (speed, amplitude) to specific needs, and the tension can be varied directly and in real time during an experiment; thanks to these features, more complex interactions (e.g. combining temporal variations with viscous behaviors) could be investigated with minor modifications of the setup.

There are a few limitations in our choice of setup as well: in particular, non-ideal matching of wires and rods, non-ideal fixed boundaries, and friction, are all factors that play a role in altering the behavior of the wave, degrading the match between experiment and idealized numerical simulation, as can be observed e.g. for the reflected wave in Fig. 6 at times greater than 1.5 seconds. Moreover, due to the limited resolution and spatial window with which the motion of the bars can be detected by the camera, only wave amplitudes between 3 and 20 cm could be reliably detected. This meant that only a restricted parameter space could be practically investigated with the experimental setup. Nevertheless, the setup provided useful qualitative information, as well as a validation of our numerical approach; together, experiments and simulations proved to be a robust tool to investigate waves in time-dependent media.

## 2.5. CONCLUSIONS

We conclude that the variation over time of the stiffness of a medium, such as the beating heart, produces an inversely proportional variation in amplitude and period of a wave traveling through it. Furthermore, if the stiffness variation presented discontinuities, reflected waves would be generated. Based on the results of our numerical simulations and literature data, we predict that a healthy diastolic relaxation will affect propagating waves differently than an impaired process, producing a wave period increase twice as large as the one that might be observed in a dysfunctional organ. This difference may potentially be exploited to directly obtain information on diastolic functionality with one SWE measurement.

## 2.6. APPENDIX: REFLECTION AND TRANSMISSION COEFFICIENTS

We show here how the reflection and transmission coefficients can be calculated for a 1D transverse wave travelling on a string that undergoes an instantaneous material property variation (e.g. a decrease in tension). This situation can be considered to be the temporal equivalent of a wave travelling across the interface between two different, ideally bonded, strings. Let us assume that the instantaneous variation happens at time  $t_0 = 0$ , and let

we consider an initial wave function  $\psi_i = f_I(x - c_1 t)$  for all  $t < 0$ . As we have seen, after the temporal discontinuity, in the setup two waves are present, a transmitted wave  $\psi_T = f_T(x - c_2 t)$  and a reflected wave  $\psi_R = f_R(x + c_2 t)$ . Notice that the transmitted and reflected waves travel at the same speed  $c_2$ , with opposite signs. We can then consider two instants in time, before (B) and after (A) the discontinuity, and define two waveforms

$$\psi_B = \psi_i = f_I(x - c_1 t), \quad (2.6)$$

and

$$\psi_A = \psi_T + \psi_R = f_T(x - c_2 t) + f_R(x + c_2 t), \quad (2.7)$$

representing the deformation of the string in these two instants. Let us now make two considerations:

1. The deformation of the string has to evolve continuously from  $\psi_B$  to  $\psi_A$  at all coordinates  $x$  (a discontinuity of  $\psi$  between two consecutive instants requires movements at infinite speeds). Therefore, it follows that for all  $x$ :

$$\psi_B(x, 0) = \psi_A(x, 0) \quad (2.8)$$

$$\implies f_I(x) = f_R(x) + f_T(x).$$

2. The vertical speed of each individual particle in the string also needs to be continuous over time (a discontinuity of  $\frac{\partial \psi(x, t)}{\partial t}$  in time would require infinite acceleration). We can write this condition as:

$$\left. \frac{\partial \psi_B(x, t)}{\partial t} \right|_{t=0} = \left. \frac{\partial \psi_A(x, t)}{\partial t} \right|_{t=0} \quad (2.9)$$

$$\implies -c_1 f_I'(x) = -c_2 f_T'(x) + c_2 f_R'(x).$$

Integrating the equation above and setting the integration constant to 0, we find that:

$$c_1 f_I(x) = c_2 (f_T(x) - f_R(x)). \quad (2.10)$$

We can then solve Eqs. (A.3) and (A.5) for  $f_R$  and  $f_T$  in terms of  $f_I$ , finding:

$$f_R(x) = \frac{c_2 - c_1}{2c_2} f_I(x), \quad (2.11)$$

$$f_T(x) = \frac{c_2 + c_1}{2c_2} f_I(x). \quad (2.12)$$

We have thus shown that the ratios of the amplitudes of initial, reflected and transmitted waves ( $A_I$ ,  $A_R$ , and  $A_T$ , respectively) are equal to

$$A_R/A_I = \frac{c_2 - c_1}{2c_2}, \quad (2.13)$$

and

$$A_T/A_I = \frac{c_2 + c_1}{2c_2}. \quad (2.14)$$

## REFERENCES

- [1] W. H. Gaasch, H. J. Levine, M. a. Quinones, and J. K. Alexander, *Left ventricular compliance: mechanisms and clinical implications*. The American journal of cardiology **38**, 645 (1976).
- [2] R. R. Chaturvedi, T. Herron, R. Simmons, D. Shore, P. Kumar, B. Sethia, F. Chua, E. Vasiliadis, and J. C. Kentish, *Passive stiffness of myocardium from congenital heart disease and implications for diastole*, Circulation **121**, 979 (2010).
- [3] C. Pislaru, P. A. Pellikka, and S. V. Pislaru, *Wave propagation of myocardial stretch: Correlation with myocardial stiffness*, Basic Research in Cardiology **109** (2014), 10.1007/s00395-014-0438-5.
- [4] Y. K. Mariappan, K. J. Glaser, and R. L. Ehman, *MAGNETIC RESONANCE ELASTOGRAPHY: A REVIEW*, Clinical anatomy (New York, N.Y.) **23**, 497 (2010).
- [5] J. F. Deprez, E. Brusseau, J. Fromageau, G. Cloutier, and O. Basset, *On the potential of ultrasound elastography for pressure ulcer early detection*, Medical Physics **38**, 1943 (2011).
- [6] M. Dhyani, A. Anvari, and A. E. Samir, *Ultrasound elastography: liver*, Abdominal Imaging **40**, 698 (2015).
- [7] L. Sang, X.-m. Wang, D.-y. Xu, and Y.-f. Cai, *Accuracy of shear wave elastography for the diagnosis of prostate cancer: A meta-analysis*, Scientific Reports **7**, 1949 (2017).
- [8] H. Kanai, *Propagation of Vibration Caused by Electrical Excitation in the Normal Human Heart*, Ultrasound in Medicine and Biology (2009), 10.1016/j.ultrasmedbio.2008.12.013.
- [9] M. Strachinaru, J. G. Bosch, B. M. van Dalen, L. van Gils, A. F. van der Steen, N. de Jong, M. L. Geleijnse, and H. J. Vos, *Cardiac Shear Wave Elastography Using a Clinical Ultrasound System*, Ultrasound in Medicine and Biology (2017), 10.1016/j.ultrasmedbio.2017.04.012.
- [10] H. Vos, B. van Dalen, I. Heinonen, J. Bosch, O. Sorop, D. Duncker, A. van der Steen, and N. de Jong, *Cardiac shear wave velocity detection in the porcine heart*, Ultrasound in Medicine and Biology **43**, 753 (2017), cited By 12.
- [11] L. Keijzer, J. Bosch, M. Verweij, N. De Jong, and H. Vos, *Intra-scan variability of natural shear wave measurements*, (2018) cited By 0.
- [12] A. Petrescu, P. Santos, M. Orłowska, J. Pedrosa, S. Bézy, B. Chakraborty, M. Cvijic, M. Dobrovie, M. Delforge, J. D'hooge, and J.-U. Voigt, *Velocities of naturally occurring myocardial shear waves increase with age and in cardiac amyloidosis*, JACC: Cardiovascular Imaging (2019), <https://doi.org/10.1016/j.jcmg.2018.11.029>.

- [13] P. Santos, A. Petrescu, J. Pedrosa, M. Orłowska, V. Komini, J.-U. Voigt, and J. D'Hooge, *Natural shear wave imaging in the human heart: Normal values, feasibility, and reproducibility*, IEEE Transactions on Ultrasonics, Ferroelectrics, and Frequency Control **66**, 442 (2019), cited By 0.
- [14] M. Vejdani-Jahromi, J. Freedman, Y.-J. Kim, G. E. Trahey, and P. D. Wolf, *Assessment of Diastolic Function Using Ultrasound Elastography*, Ultrasound in Medicine & Biology **44**, 551 (2018).
- [15] G. A. Holzapfel and R. W. Ogden, *Constitutive modelling of passive myocardium: a structurally based framework for material characterization*, Philosophical Transactions of the Royal Society A: Mathematical, Physical and Engineering Sciences **367**, 3445 (2009).
- [16] T. C. Gasser and C. Forsell, *The numerical implementation of invariant-based viscoelastic formulations at finite strains. An anisotropic model for the passive myocardium*, Computer Methods in Applied Mechanics and Engineering **200**, 3637 (2011).
- [17] T. S. E. Eriksson, A. J. Prassel, G. Plank, and G. A. Holzapfel, *Influence of myocardial fiber/sheet orientations on left ventricular mechanical contraction*, Mathematics and Mechanics of Solids **18**, 592 (2013).
- [18] O. Gültekin, G. Sommer, and G. A. Holzapfel, *An orthotropic viscoelastic model for the passive myocardium: continuum basis and numerical treatment*, Computer methods in biomechanics and biomedical engineering **19**, 1647 (2016).
- [19] H. Kanai, *Propagation of spontaneously actuated pulsive vibration in human heart wall and in vivo viscoelasticity estimation*, IEEE Transactions on Ultrasonics, Ferroelectrics, and Frequency Control **52**, 1931 (2005).
- [20] B. A. Auld, J. H. Collins, and H. R. Zapp, *Signal Processing in a Nonperiodically Time-Varying Magnetoelastic Medium*, Proceedings of the IEEE **56**, 258 (1968).
- [21] S. M. Rezende and F. R. Morgenthaler, *Magnetoelastic Waves in Time-Varying Magnetic Fields. I. Theory*, Journal of Applied Physics **40**, 524 (1969).
- [22] L. Felsen and G. Whitman, *Wave propagation in time-varying media*, IEEE Transactions on Antennas and Propagation **18**, 242 (1970).
- [23] R. Fante, *Transmission of electromagnetic waves into time-varying media*, IEEE Transactions on Antennas and Propagation **19**, 417 (1971).
- [24] F. Fedotov, A. Nerukh, T. Benson, and P. Sewell, *Investigation of electromagnetic field in a layer with time-varying medium by volterra integral equation method*, Journal of Lightwave Technology **21**, 305 (2003).
- [25] C. Bing-Kang, Y. Zhang-Ying, and G. Ben-Qing, *Solution of Electromagnetic Wave in Time-Varying Media in Two-Dimensional Space*, Chinese Physics Letters **23**, 595 (2006).

- [26] A. Nerukh, T. Remayeva, N. Sakhnenko, and D. N. Chigrin, *Evolution of Waves Induced by Time Change of Medium Permittivity in a Sphere*, in *AIP Conference Proceedings*, Vol. 1176 (AIP, 2009) pp. 140–142.
- [27] A. G. Hayrapetyan, J. B. Götte, K. K. Grigoryan, S. Fritzsche, and R. G. Petrosyan, *Electromagnetic wave propagation in spatially homogeneous yet smoothly time-varying dielectric media*, *Journal of Quantitative Spectroscopy and Radiative Transfer* **178**, 158 (2016).
- [28] V. L. Preobrazhenskii and Y. K. Fetisov, *Magnetostatic waves in a time-dependent medium*, *Soviet Physics Journal* **31**, 898 (1988).
- [29] J. N. Shive and R. Weber, *Similarities in Physics* (1982).

# 3

## **TAPERING OF THE INTERVENTRICULAR SEPTUM CAN AFFECT ULTRASOUND SHEAR WAVE ELASTOGRAPHY: AN IN VITRO AND IN SILICO STUDY**

## Abstract

Shear wave elastography (SWE) has the potential of determining cardiac tissue stiffness from non-invasive shear wave speed measurements, important e.g. for predicting heart failure. Previous studies showed that waves traveling in the interventricular septum (IVS) may display Lamb-like dispersive behaviour, introducing a thickness-frequency dependency in the wave speed. However, the IVS tapers across its length, which complicates wave speed estimation by introducing an additional variable to account for. The goal of this work is to assess the impact of tapering thickness on SWE. The investigation is performed by combining in-vitro experiments with acoustic radiation force (ARF) and 2D finite element simulations, to isolate the effect of the tapering curve on ARF-induced and natural waves in the heart. The experiments show a 11% deceleration during propagation from the thick to the thin end of an IVS-mimicking tapered phantom plate. The numerical analysis shows that neglecting the thickness variation in the wavenumber-frequency domain can introduce errors of more than 30% in the estimation of the shear modulus, and that the exact IVS shape, rather than the absolute amount of tapering, determines the dispersive behaviour of the wave. These results suggest that septal geometry should be accounted for when deriving cardiac stiffness with SWE.

### 3.1. INTRODUCTION

Shear Wave Elastography (SWE) has been the subject of research, over the past decades, because of its potential to improve clinical diagnoses by non-invasively determining tissue stiffness [1–3] in radiology. In particular, SWE could have important applications in the field of cardiac imaging [4–8] as a way to assess the stiffness of the heart muscle, which has been identified as a relevant parameter in the diagnosis of heart failure [9, 10].

In cardiac ultrasound SWE, waves are typically tracked along the interventricular septum (IVS), and can have two different excitation sources: either they are generated by the natural physiology of the heart, e.g. valve closure [7, 11–14], or they are generated by an external source, such as acoustic radiation force (ARF) [15–18]. After wave excitation, the waves are recorded using high frame rate imaging, and their propagation pattern in the time domain is used to extract their propagation speed. Under idealized conditions (i.e. in a bulk, purely elastic, time-invariant, linear, isotropic and nearly incompressible material), the speed of a shear wave is proportional to the shear modulus of the medium, following the relation:

$$G = \rho c^2 \quad (3.1)$$

where  $\rho$  is the density of mass (in  $\text{kg}/\text{m}^3$ ),  $c$  is the bulk shear speed (in  $\text{m}/\text{s}$ ), and  $G$  is the shear modulus (in  $\text{Pa}$ ).

However, the IVS is far from these idealized conditions, and waves traveling along the plate-like heart wall show a dispersive behaviour similar to that of Lamb waves [4, 19–22]. These are waves characterized by two infinite sets of guided modes (symmetric and antisymmetric) that propagate with speeds dependent not only on the shear modulus, but also on the thickness of the medium and the frequency of the waves themselves [23]. Moreover, when a plate is loaded by a fluid (as is the case with the IVS, which separates the two blood-filled ventricles), the dispersive behaviour also depends on the properties of that fluid [23, 24], further complicating the relation between wave speed and muscle stiffness. Varying thickness of the IVS could further affect wave propagation speed, and might be one of the underlying causes for the large reported variability of shear wave speeds in literature on healthy volunteers: natural shear wave studies report speeds with differences of up to 60 % between studies [8, 25] and up to 20 % within individual works [8], while studies employing acoustic radiation force can show inter- and intra-study differences of 60 % [17, 18].

Efforts have been made in the cardiac SWE field to account for the dispersive behaviour of the wave in the material characterization algorithms. Instead of studying the wave propagation characteristics in the space-time ( $x-t$ ) domain, various studies [4, 19, 20, 26, 27] have analysed waves in the frequency-wavenumber ( $f-k$ ) domain to reconstruct the dispersion curves. When approaching the IVS as a fluid-loaded elastic plate, the shear modulus can be extracted by fitting a theoretical Lamb wave dispersion curve to the experimental ones. The advantage of this approach is that the dispersion curves allow to directly retrieve the bulk shear speed of a medium rather than the dispersive propagation speed in a plate. The first can be easily translated into the stiffness via Eq. 1, while the latter cannot. In fact, it was shown for ARF-based SWE in flat [28] and curved plates [26] that space-time analyses could underestimate the shear modulus by approximately 50 % and 40 % respectively, while analysis in the frequency-wavenumber domain yielded errors in

shear modulus of approximately 8 % and 4 % respectively, compared to mechanical elasticity tests.

An underlying assumption of the dispersion curve analysis is that the thickness of the plate is constant. However, it is generally known that the cardiac wall thickness can vary by up to a factor 3 from the equatorial point to the apex in healthy volunteers [29], and this variation could be even more dramatic in hypertrophic patients [30]. Thickness variations are expected to have a significant impact on the propagation of guided waves due to their dependency on the frequency-thickness product, which is especially strong at lower frequencies for zero-order modes. In fact, it has already been shown that, when the slowly varying thickness of a waveguide reaches the frequency-thickness cut-off of a certain mode, mode conversion and reflections take place [31–33]. Interestingly, natural and ARF-generated waves are expected to be affected differently by the thickness variation, due to their different frequency contents (up to around 150 Hz and 1000 Hz, respectively [19, 22, 27, 28]).

To the best of our knowledge, the effects of cardiac thickness variations on shear wave propagation characteristics has not been studied yet. The goal of this work is to determine if and how the natural IVS thickness variations could affect cardiac SWE measurements. Therefore, to untangle the complex relationship between wave properties and myocardial material characteristics, we isolated the effects of geometry by studying an elastic plate with varying thickness using numerical simulations and experiments. The experiments were analysed in space-time domain and were used as a proof-of-principle to show that the speed of the waves typically used in SWE varies along the tapered plate. They also served for validation purposes of our simulation settings; the numerical settings were further verified by comparing quantitatively the simulation results in a flat fluid-loaded plate to the theoretical Lamb wave propagation. The simulations allowed a greater degree of flexibility in modelling different excitation sources and geometries: the effects of geometry on both natural and ARF-induced waves were studied in space-time as well as in frequency-wavenumber domain, and it was possible to assess whether the waves are affected only by the total amount of thickness reduction, or rather depend on the specific tapering curve.

## 3.2. METHODS

### 3.2.1. EXPERIMENTAL SETUP

To isolate the effects of tapering on wave propagation, a polyvinyl alcohol tissue-mimicking phantom was created following the recipe in [34]. A mould was shaped to produce a phantom plate with a tapered section: 12 cm long, 5 cm wide and with thickness varying between 9 mm and 3 mm [29]. In terms of geometry, the phantom can be schematically divided into three sections, each 4 cm long: first, a flat section with a constant thickness of 9 mm, followed by a section in which the thickness decreases linearly from 9 mm to 3 mm, and, finally, another flat section with a constant thickness of 3 mm (see Fig. 3.1a). The flat sections of the phantom served two purposes: they extended the propagation medium, reducing boundary effects at the edges of the tapered section, and they provided flat regions of the same sample that were used to obtain reference measurements. The phantom was then entirely submerged in a water tank to simulate the

blood that surrounds the IVS. The plate was held in position halfway across the depth of the water tank by 3D printed supports, ensuring that the central section of the sample was loaded by water on both sides and the sample would not float (see Fig. 3.1b).

SWE measurements were performed using a P-4-2 probe connected to a Verasonics Vantage research platform (Verasonics, Kirkland, WA, U.S.). A wave was generated in the centre of the phantom by focusing a push pulse with frequency of 2 MHz, F-number of 1.9, duration of  $400 \mu\text{s}$  and a focus depth of 40 mm. After wave generation, the probe switched into tracking mode to record the traveling wave for 20.2 ms using high frame rate imaging with plane wave compounding ( $-7 \text{ deg}$ ,  $0 \text{ deg}$ ,  $7 \text{ deg}$ ) [32] resulting in an effective frame rate of 3223.5 Hz.

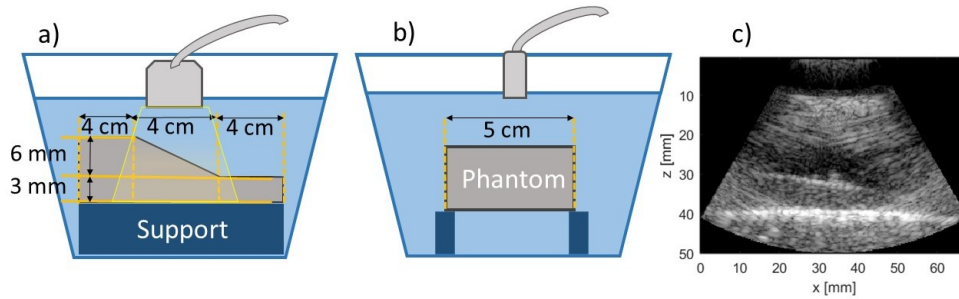


Figure 3.1: Schematic representation of the experimental setup. a) side view; b) rear view; c) B-mode image. The phantom (in light grey) consists of a 4 cm long, 9 mm thick flat section, followed by a 4 cm long section that tapers from 9 to 3 mm, and ends in another 4 cm long flat section, 3 mm thick. 3D printed supports (dark blue) held the phantom halfway through the depth of the tank, while allowing the central section of the plate to be loaded by water on both sides.

### 3.2.2. EXPERIMENTAL DATA ANALYSIS

Analytic data were obtained by beamforming the radio frequency (RF) data using the Verasonics software. One-lag autocorrelation [35] was applied to the IQ-data to obtain the axial particle velocity field. Before calculating the phase differences, the tissue velocity data were smoothed with a Gaussian spatial smoothing filter with total sigma-widths of  $0.47 \text{ deg}$  in the azimuthal direction by  $0.5 \text{ mm}$  in the axial direction. The obtained velocity matrix has a temporal resolution of  $0.3 \text{ ms}$ , and a spatial resolution of  $0.24 \text{ mm}$  in both the lateral (x) and axial (z) direction. All post-processing was performed using Matlab R2018b (MathWorks, Natick, MA, U.S.).

Particle velocity data was extracted along nine M-lines (virtual lines of receivers) approximately  $2 \text{ cm}$  long, which were placed at a depth of  $10 \%$  to  $50 \%$  of the phantom thickness with respect to its top surface, in increments of  $5 \%$ . The velocity data in the lower half of the phantom had too low signal-to-noise ratio (SNR) and was therefore excluded from shear wave speed analysis. The extracted data along each line was then spatially up-sampled to a spacing of  $0.015 \text{ mm}$ . As the ARF was applied in the centre of the x direction, a left and right propagating shear wave was observed. The space-time trajectories of both waves were subsequently analysed by means of a Radon Sum algorithm [36] to determine their slopes, which correspond to wave propagation velocities. The difference in speed of

the left- and right-propagating waves was calculated for all the m-lines. The average and standard deviation of the speed differences were then computed and used to compare wave propagation in the flat and the tapered sections.

### 3.2.3. NUMERICAL CONFIGURATION

The numerical model was implemented in Abaqus CAE (Abaqus Inc., Providence, RI, U.S.A.) using the Finite Element Method (FEM), which has already been extensively used for modelling ARF-based SWE in biological tissue [37–39] and for waves in curved plates [26]. Similar to the experimental geometry, the IVS was modelled as a 2D plate under plane strain assumption, with its thickness tapering linearly from 9 mm to 3 mm [24] and a length of 4 cm, as shown in Fig. 3.2. Symmetric boundary conditions were applied in the x-direction to the left side of the plate in Fig. 3.2 to avoid boundary effects on the wave excitation. The other sides of the plate were surrounded by a 4 cm thick layer of water, the motion of which was coupled to that of the plate through tie-constraints. The outer boundaries of the water were modelled with absorbing boundary conditions to absorb all arriving wave energy. In this model, the plate was described as an isotropic nearly-incompressible elastic material with a density  $\rho$  of 1045 kg/m<sup>3</sup> [26], a Poisson's ratio  $\nu = 0.49999$  [40] and a Young's modulus of  $E = 9$  kPa [18], to represent the cardiac muscle in its diastolic phase. This corresponds to a shear modulus of 3 kPa and thus a bulk shear speed of 1.69 m/s. The water was modelled as an acoustic medium, with a bulk modulus of 2.2 GPa and a density of 1000 kg/m<sup>3</sup>, corresponding to a bulk compressional wave speed of 1483 m/s.

The plate was modelled with quadrilateral elements with a length and thickness of 0.2 mm (in the flat plate) or length of 0.2 mm and thickness between 0.2 and 0.07 mm (for the tapered plates). Based on the bulk shear speed, these mesh sizes resulted in frequencies up to 600 Hz being sampled with at least 15 points per wavelength. The solution computed by Abaqus was then sampled with a temporal resolution of 0.038 ms, corresponding to at least 43 samples per period in the frequency range mentioned. To reduce computation time, the water domain was meshed with quadrilateral elements with length and thickness of 0.2 mm only in proximity of the plate domain. The mesh size was then allowed to increase up to 2 mm at the outer boundaries of the water domain (see also Fig. 3.2).

Natural and ARF waves were simulated by applying a Gaussian-shaped velocity pulse in the transversal direction at the left edge of the plate (see Fig. 3.2), with peak amplitudes of 2 cm/s. The pulse simulating natural waves had a total duration of 10 ms, while the ARF wave was simulated with a 2 ms pulse, corresponding to full-width half-maximum frequency contents of around 100 Hz and 500 Hz respectively.

The wave propagation was simulated for a total duration of 40 ms, which is long enough for one pulse to be excited and reach the opposite side of the plate. The simulations were run using an explicit solver.

### 3.2.4. NUMERICAL MODEL VALIDATION

The model validation of the numerical model consisted of two steps. First, the chosen numerical settings of our FEM model were verified for a fluid-loaded tissue-mimicking plate by comparing the dispersion characteristics of the simulated ARF wave to those of theoretical Lamb waves. For this purpose, we considered a 4 cm long plate with a constant thickness of 9 mm, surrounded by water, as illustrated in the top right panel of Fig. 3.2.

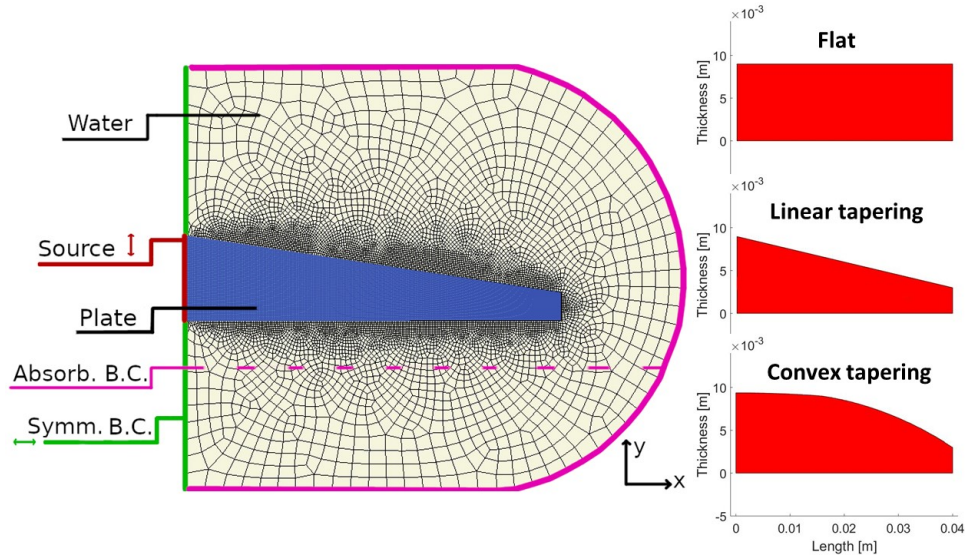


Figure 3.2: The simulation setup. On the left the numerical FE model is shown, with the plate highlighted in blue and the water in grey. The top right image depicts the 9 mm thick flat plate, below which is shown the plate with linear tapering and, at the bottom, the plate with convex tapering.

The material properties of plate and water were the same as described in section 3.2.3. The theoretical A0 curve was calculated with the equation for soft tissue mimicking plates in blood [24]:

$$4k_L^3\beta \cosh(k_L h) \sinh(\beta h) - (k_s^2 - 2k_L^2)^2 \sinh(k_L h) \cosh(\beta h) = k_s^4 \cosh(k_L h) \cosh(\beta h) \quad (3.2)$$

where  $k_L = \omega/c_L$  is the Lamb wave number,  $c_L$  is the frequency dependent Lamb wave velocity,  $k_s = \omega/c_s$  is the shear wave number,  $c_s$  is the bulk shear wave speed,  $\beta = \sqrt{k_L^2 - k_s^2}$ , and  $h$  is half the thickness of the plate.

The A0 mode was chosen for validation because the employed source generated mainly antisymmetric modes, and because the zeroth-order mode is present at all frequencies, thus yielding more data for comparison with a theoretical curve.

Second, a more qualitative validation of our FEM model was performed with the tapered plate model, described in section 3.2.3, by analysing the simulated ARF wave in space-time, as well as the speed difference between left and right halves of the M-lines, in comparison to the experimental ones. The duration of the pulse used in the simulations of this validation step was 5 ms, corresponding to a full-width half-maximum frequency content of around 250 Hz, to better match our experimental data.

### 3.2.5. NUMERICAL DATA ANALYSIS

The simulated data was processed in Matlab. A 2.5 cm long M-line was positioned at a depth of 10 % of the plate thickness. The M-line was drawn 1 cm away from the left edge

of the model (where the source is applied), in order to reduce the effects of proximity to the source [41]. The particle velocity data was then interpolated from the FEM-grid to an equidistant grid with 0.05 mm spacing along each M-line. Distances were consequently measured along the M-lines. Because the simulated wave propagated from one end of the plate to the other, as opposed to being generated in the centre (as was the case in the experiments), a single one-directional shear wave propagated from left to right across the whole plate, from which the Radon Sum algorithm can extract only a single propagation speed. To observe possible decelerations, therefore, the propagation path was split into a left- and a right- half, and each half was analysed with the Radon Sum algorithm separately.

For the wave analysis in the frequency-wavenumber domain, the space-time velocity data recorded on one single M-line (at a depth of 10 % of the plate thickness) was further processed with a Tukey window (with cosine fraction  $r = 0.2$ ) to reduce windowing-related artefacts after Fourier transformation. The data was then converted to the  $f$ - $k$  domain by means of a 2D Fast Fourier Transform, where the areas of maximum amplitude correspond to the dispersion curves. To reduce clutter, an amplitude mask was applied to the  $f$ - $k$  data, filtering out amplitudes below 20 % of the maximum. Only data for frequencies up to 600 Hz was considered during the analysis, to guarantee correct sampling of every wavelength included.

Only for the validation step, nine M-lines were drawn at depths from 10 % to 50 % of the thickness of the plate, with 5 % increments, to enable a comparison with the experiments. The propagation measured on the nine M-lines were then split in left- and right-halves, and the difference between left- and right-speeds at all depths was computed and averaged.

### 3.2.6. NUMERICAL DISPERSION CURVE ANALYSIS AND ERROR MAP RECONSTRUCTION

While space-time domain analysis is still common in cardiac SWE studies, a more appropriate and theoretically sound approach to extract stiffness from wave propagation measurements is to analyse dispersion curves. The approach used to analyse  $f$ - $k$  domain data is summarised in Fig. 3.3. For each of the simulated waves, the data was extracted following the method described in section 2e (panels 1-3 in Fig. 3.3). The extracted curve was then compared to a theoretical A0 curve with a specific bulk shear speed and thickness (panel 4 in Fig. 3.3). A Root Mean Squared Percentage Difference (RMS-PD) error function was introduced to quantify the comparison:

$$Err = \sqrt{\sum_i^N \frac{(100(k_i - k_i^T)/k_i^T)^2}{N}} \quad (3.3)$$

where  $Err$  is the RMS-PD error,  $k_i$  is the wavenumber of the extracted curve at the  $i^{th}$  frequency,  $k_i^T$  is the wavenumber of the chosen theoretical curve at the same frequency, and the sum runs over all  $N$  frequencies at which the curve was extracted. This comparison was repeated for all the theoretical curves within the parameter space (panel 5 in Fig. 3.3), which comprised bulk shear speeds between 0.5 m/s and 3.0 m/s (with resolution of 0.001 m/s) and thicknesses between 2 mm and 10 mm (with resolution of 0.1 mm). Plotting the

RMS-PD value of each comparison in the same figure results in a 2D RMS-PD map (panel 6 in Fig. 3.3). The theoretical A0 curve that best fits the simulated one can then be identified as the minimum in the RMS-PD map. At the same time, the map shows how much the error grows when moving in the parameter space, and allows to fix one parameter (e.g. thickness) and identify which value of the other one generates the lowest RMS-PD.

The shear speeds extracted from the  $x-t$  data and from the best fitting curves in the  $f-k$  domain were converted into values of the shear modulus  $G$  through Eq. 3.1, which is commonly used in most cardiac SWE studies. However, this equation only holds when  $c$  is the bulk shear speed. It should be therefore kept in mind that the speed derived from the  $x-t$  data does not represent the bulk speed, since dispersion is occurring. At the same time, the  $f-k$  analysis extracts the bulk shear speed for a flat plate, which is used as an approximation for the bulk shear speed in tapered plates in this study. To study how to minimize the impact of this approximation, different values of constant thickness were considered when extracting the speed from the RMS-PD maps: the extremal thicknesses of the plate (9 mm and 3 mm), the arithmetic mean of the thickness, and its harmonic mean. It can be shown that, at low frequencies, an A0 wave propagates across a tapered plate in approximately the same time it would take it to propagate across a plate of constant thickness equal to the harmonic mean of the tapered thickness; at higher frequencies, the same result holds true for the arithmetic mean of the tapered thickness.

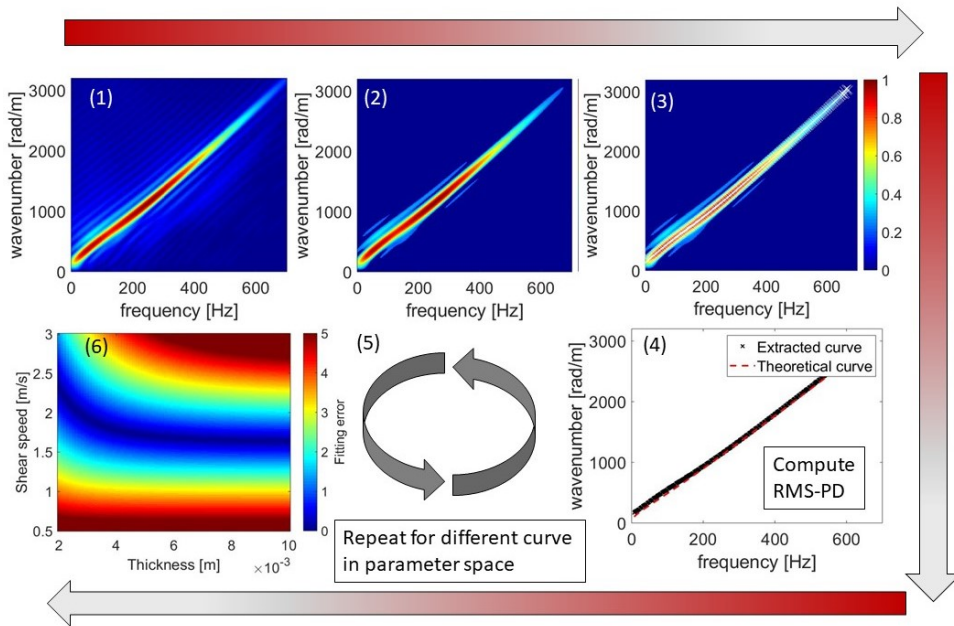


Figure 3.3: Procedure to reconstruct RMS-PD maps. (1) Retrieve  $f-k$  data, (2) mask out 20% lowest amplitudes, (3) identify coordinates of maximal amplitude at every frequency, (4) compare with a theoretical A0 curve corresponding to one point in the parameter space and compute its RMS-PD, (5) repeat for all points in the parameter space, (6) make RMS-PD map for all parameters.

### 3.2.7. EFFECTS OF DIFFERENT IVS SHAPES

Since the real IVS can present a variety of different shapes, we simulated another tapered plate with the same material properties as before, the same total amount of tapering (i.e. a thickness variation between 9 and 3 mm), but a different shape, specifically a convex one (see Fig. 3.2). This model, in combination with the linearly tapered plate, allowed us to investigate whether the effects of tapering depend on how the thickness varies over space or rather just on the total thickness variation. For the purpose of this comparison, the M-lines in the two tapered plates were drawn along their entire modelled length to ensure the same initial and final plate thickness along the M-line.

### 3.3. RESULTS

In this section we will first present the results of the experiments on a tapered phantom (Fig. 3.4 and 3.5), showing that waves propagate differently when they travel towards the thin or the thick ends of the plate. Then we show numerical results that allow a comparison of the simulations with theory and with the experiments (Fig. 3.6 and 3.7), for validation purposes. All subsequent results (Fig. 3.8 and 3.9, Tables 3.1 and 3.2) are produced by simulations to investigate in more detail the effects of tapering on the propagation of Lamb waves.

#### 3.3.1. EXPERIMENTS

Experiments were conducted on a PVA phantom to assess whether there are measurable differences in the propagation of a wave along flat and tapered sections of a plate. Fig. 3.4 show snapshots of the propagating wave in two sections of the phantom (the upper panels depict the flat part of the phantom, whereas the lower panels illustrate the tapered part of the phantom). Three key features can be observed in the propagation patterns. First, the waves propagating in the tapered section attenuate less rapidly than the one in the flat section. Second, the wave traveling in the flat section develops, during propagation, a split in left and right wavefronts at depths greater than approximately 20 % of the thickness; this feature has already been reported in literature [26] and is probably associated to the presence of the A1 mode besides the A0 mode. Third, close to the top surface in the flat section, the split is not present and the attenuation appears to be weaker.

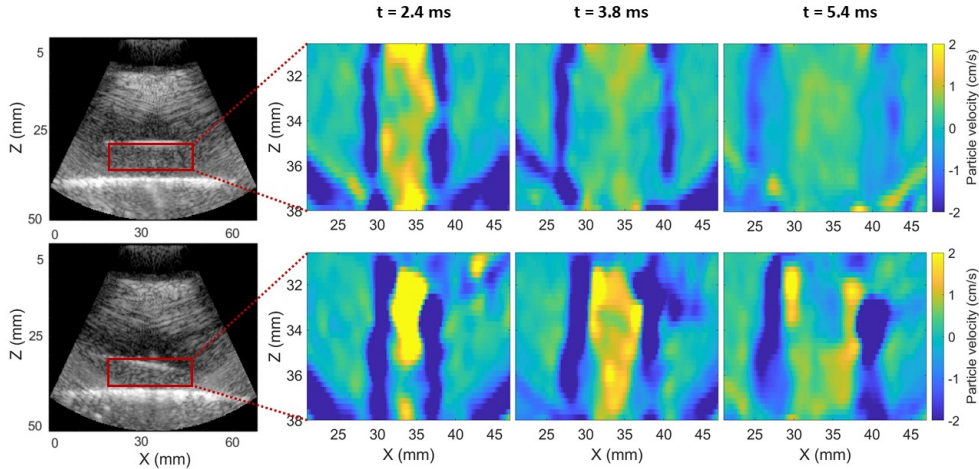


Figure 3.4: Snapshots of experimental wave propagation recorded in the flat (above) and tapered (below) sections of the PVA phantom, and B-mode view of the two sections (rightmost column). The ARF push was applied at  $t = 0.0$  ms and was centered at  $x = 34$  mm. The colours in the propagation snapshots represent particle velocity.

In Fig. 3.5, the two panels show the experimental wave propagation measured along a single M-line at a depth of about 10% of the plate thickness in the flat (left panel) and

tapered (right panel) sections. In the flat section, both branches of the wave propagate with a speed of 1.55 m/s, whereas, in the tapered section, the two branches have different speeds: the branch propagating towards the thicker end travels at 1.13 m/s, while the other branch travels at 1.07 m/s. Analyzing nine M-lines across the phantom thickness in the flat section, the average speed difference (with standard deviation) between left and right branch is  $0.01 \pm 0.04$  m/s, which is negligible in magnitude with respect to the standard deviation. In contrast, performing the same analysis on data measured in the tapered section, and taking into account nine M-lines again, the average difference between left and right speeds is  $0.16 \pm 0.07$  m/s, which is considerably larger than its standard deviation. We can conclude that tapering causes the wave to decelerate during propagation towards the thinner end. An example wave propagation pattern of the top M-line in the tapered plate is shown in the right panel of Fig. 5, where the wave branches traveling towards the thick and thin ends have speeds of 1.13 m/s and 1.07 m/s, respectively.

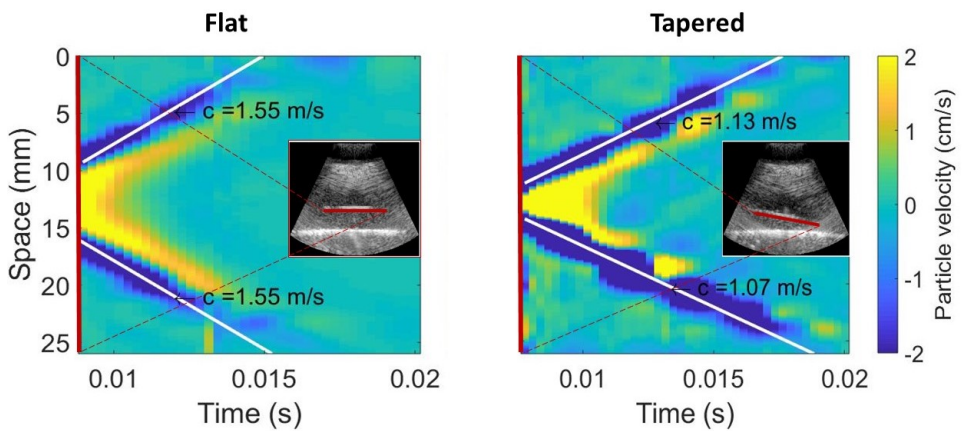


Figure 3.5: Experimental wave propagation recorded in the flat section (left) and tapered section (right) of a PVA phantom. The m-line (in red) was placed at about 1 mm of depth with respect to the top surface of the phantom (red line in the B-mode panels), centred with respect to the lateral coordinate of the focus of the ARF push beam. The propagation speed of the two wave branches is comparable in the flat section, whereas it decreases with thickness in the tapered part of the phantom.

### 3.3.2. SIMULATIONS

#### VALIDATION

The two panels in Fig. 3.6 present the propagation of simulated ARF waves obtained in the flat plate along a 2.5 cm long M-line placed at a depth of 0.9 mm in  $x-t$  and  $f-k$  domains (left and right panels, respectively). In the  $x-t$  domain plots, the superimposed white lines show the propagation trajectory estimated by the Radon Sum algorithm, corresponding to speeds of 1.35 m/s and 1.38 m/s. The white line in the  $f-k$  domain plots represent the theoretical A0 mode, computed for a flat 9 mm thick fluid-loaded plate. The gradient of this line indicates a propagation speed that ranges between 0.5 m/s for  $f = 10$  Hz and 1.4 m/s for  $f = 600$  Hz. In particular, the good match between the simulated and the theoretical A0 curves (RMS-PD of 0.12 %) confirms that the numerical settings employed

in our model are adequate for reliable simulations.

To compare numerical and experimental results, the speeds were further analysed separately for the left and right halves of nine M-lines at depths between 0.9 mm and 4.5 mm. The speed difference between left and right branches was averaged over these nine M-lines, yielding an average difference of  $0.01 \pm 0.02$  m/s, confirming that the simulated wave does not undergo variations of speed in a plate with constant thickness. Moreover, performing the same analysis for the simulated tapered plate, the average propagation speed difference between left and right halves was found to be  $0.10 \pm 0.05$  m/s, confirming that the simulations capture correctly the deceleration introduced by tapering.

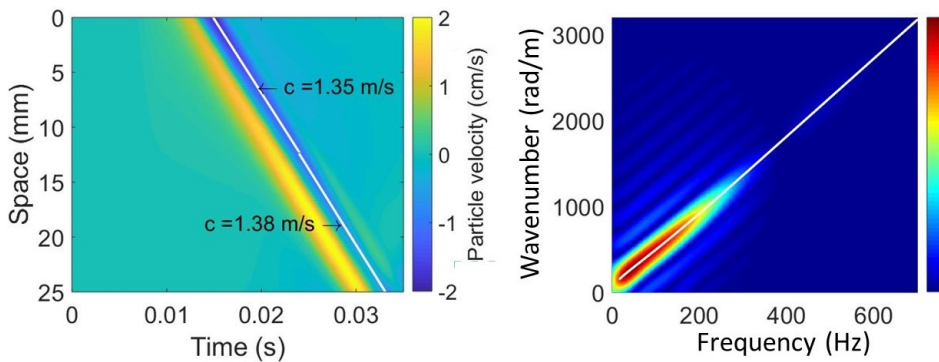


Figure 3.6: Simulated ARF wave propagation obtained along a 2.5 cm long m-line in a 4 cm long, 9 mm thick flat plate, at a depth of 0.9 mm. On the left, the wave is represented in the  $x-t$  domain: the colour scheme represents particle velocity and the white lines show a Radon Sum estimation of the trajectory of the wave. On the right, the wave is represented in the  $f-k$  domain, with the white line representing the theoretical A0 dispersion curve for a plate surrounded by water with the same geometry and medium properties. The colour scheme represents the magnitude of the Fourier-transformed velocity recorded along the M-line.

Figure 3.7 shows snapshots of the propagation of the simulated ARF waves propagating in a flat 9 mm thick plate (top) and a plate with thickness tapering between 9 mm and 3 mm (bottom). Comparing qualitatively the experimental and simulated propagation snapshots in the flat plate, we can notice that the three features identified in the experimental data are also present, to some extent, in the simulations: the wave appears to attenuate less in the tapered plate and closer to the surfaces, and the wavefront in the central section of the simulated plate presents a distortion similar to the wavefront splitting observed in the experiments. In the simulated data, however, a wavefront with positive amplitude also appears in front of the original wave, which was not observed in the experimental data and which appears to increase in amplitude during propagation.

#### ARF VERSUS NATURAL WAVES IN A LINEARLY TAPERED PLATE

Due to their different frequency contents, natural and ARF-generated waves can be expected to be affected differently by the tapering of the plate. To investigate this, Fig. 3.8 shows two simulated waves (one ARF-based and one natural) in the  $x-t$  domain, tracked on an M-line at a depth of 10 % of the plate thickness. The black lines indicate the Radon sum extracted trajectory. While the ARF-induced wave propagates with an essentially con-

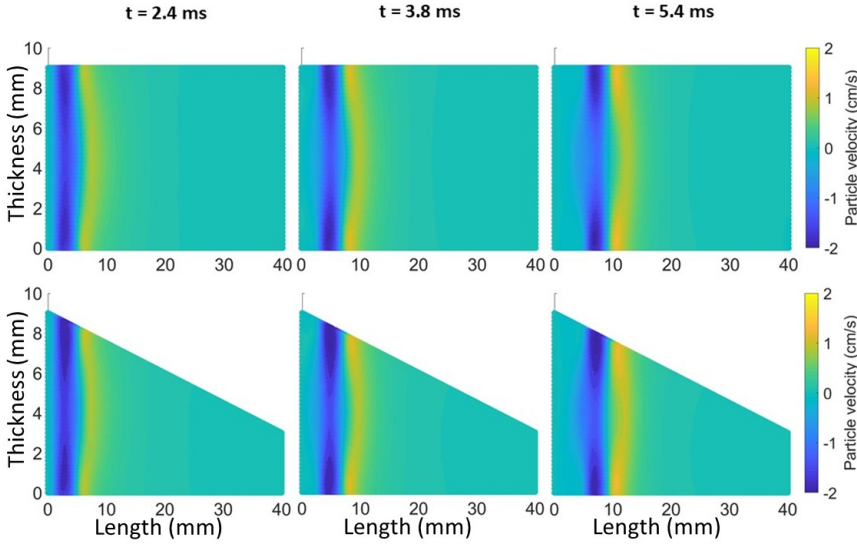


Figure 3.7: Snapshots of the propagation of a simulated ARF wave in a 4 cm long, 9 mm thick flat plate (top) and 9 mm to 3 mm tapered plate (bottom), both submerged in water.

stant speed along the entire length of the M-line (1.40 m/s in the first half, 1.39 m/s in the second half), it is clear that the  $x-t$  trajectory of the natural wave is curved: two lines with different inclinations fit the first and the second halves of the trajectory, resulting in speeds of 1.27 m/s and 0.99 m/s, respectively. This result is in agreement with theoretical expectations, since the phase speed of the A0 mode is lower at lower frequency-thickness products.

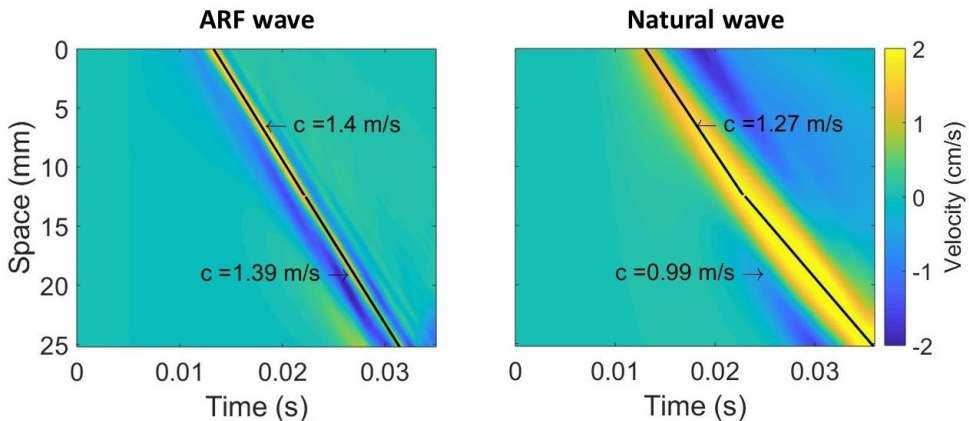


Figure 3.8: Space-time propagation of ARF waves (left) and -naturally generated waves (right) in a plate with linear tapering between 9 and 3 mm. The black lines show the Radon Sum estimation of the wave trajectories, considering the first and the second half of the travel path separately.

Figure 3.9 displays the error maps corresponding to an ARF wave (left panel) and a natural wave (right panel), computed as described in Fig. 3.3. As can be observed in Fig. 3.9, the RMS-PD maps for ARF waves and naturally generated waves are quite different, with the natural waves showing a greater sensitivity to the thickness parameter, as can be expected: at the higher frequencies typical of ARF waves, the A0 curve is flat and insensitive to thickness variations, whereas at the low frequencies of natural waves the dispersion curve is slanted and the phase speed varies considerably with the thickness. Indeed, with natural waves, depending on which thickness value is used as input to identify the best-fitting bulk shear speed, the value of the latter can vary greatly. Moreover, it can be seen for both waves that neglecting the tapering and assuming a thickness of 9 mm results in a higher RMS-PD than, for instance, assuming a thickness of 6 mm (corresponding to the average thickness of the plate). Underestimating the thickness also leads to higher RMS-PD, as well as higher estimated speed for both waves.

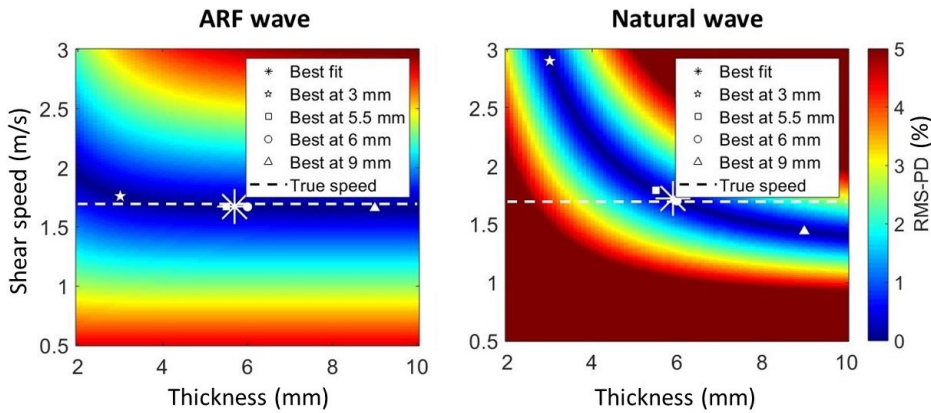


Figure 3.9: RMS-PD maps for the ARF (left) and natural (right) waves in a with plate linear tapering between 9 and 3 mm. The white star shows the coordinates of the curve with minimal RMS-PD; the white filled polygons indicate the coordinates of the best fitting curves at a fixed thickness of 3 mm (star), 5.5 mm (square), 6 mm (circle), and 9 mm (triangle). The dashed line shows the true value of bulk shear speed in the simulated material. The colour scheme represents the amplitude of the fitting error, i.e. the RMS-PD value.

To obtain Table 3.1, first the curves with lowest RMS-PD were identified for different fixed values of plate thickness. Then, the shear modulus  $G$  was computed (via Eq. 3.1) using the corresponding bulk shear speed. Finally, the value of  $G$  thus obtained was compared with the input value of the simulation. As can be seen from this table, assuming an unchanged equatorial thickness of 9 mm leads to underestimation of  $G$ , resulting in especially large errors when analysing natural waves (4 % underestimation for ARF waves, 27 % underestimation for natural waves). Furthermore, as was already visible from the error distribution portrayed in Fig. 3.9, underestimating the thickness of the plate (e.g. assuming a thickness of 3 mm) can lead to overestimations of  $G$  for both wave types, especially severe in the case of natural waves. Finally, Table 3.1 reports the results of assuming a constant thickness corresponding to either the arithmetic mean (6 mm) or harmonic mean (5.5 mm) of the plate thickness.

Error in shear modulus estimation						
Excitation type	$x-t$ domain analysis	$f-k$ domain analysis				
		$h = 9$ mm	$h = 6$ mm	$h = 5.5$ mm	$h = 3$ mm	Best fit
ARF	-34.7% (left)	-4.0%	-2.9%	-2.8%	+7.9%	-2.9%
	-35.6% (right)					
Natural	-46.2% (left)	-27.8%	+0.7%	+11.6%	+192.9%	+3.0%
	-67.3% (right)					

Table 3.1: Percentage error in the estimation of modelled  $G$  (3 kPa), based on the bulk shear speed extracted from  $x-t$  data and by fitting the simulated A0 of a linearly tapering plate. For the A0 fitting, theoretical curves were considered corresponding to flat plates with different constant values of thickness. 6 mm is the arithmetic mean of the thickness of the plate, 5.5 mm is its harmonic mean. The best fitting curve for the ARF data corresponds to a thickness of 5.7 mm, while for the natural wave it corresponds to a thickness of 5.9 mm. In the  $x-t$  domain column, two percentages are given, representing the values computed for the left and right halves of the M-lines. The positive sign indicates overestimation, the negative sign underestimation.

#### ARF VERSUS NATURAL WAVES IN A CONVEX TAPERED PLATE

The RMS-PD maps for the curves extracted for the convex plate were used to produce Table 3.2, from which it can be seen that the shape plays a role on how the wave is affected by the tapering. The difference between the  $G$  estimated for the left and right halves of the M-line in  $x-t$  domain is smaller in the convex plate, meaning that the wave decelerates less during propagation. Moreover, we note that fitting the A0 mode assuming a thickness of 6 mm, a viable solution in the linearly tapered plate, now can result in severe overestimation of the shear modulus, especially for the natural waves. Smaller deviations from the actual implemented shear modulus are obtained by setting the thickness to either 6.9 or 7.7 mm, the harmonic mean and arithmetic mean of the thickness of the convex slab, respectively. Moreover, the bulk shear speed of the curve with lowest RMS-PD for a thickness of 3 mm was greater than 3 m/s, outside the boundaries of the parameter space considered to build the RMS-PD maps (as indicated by  $> +213.5\%$  in Table 3.2).

### 3.4. DISCUSSION

#### 3.4.1. EFFECTS OF TAPERING ON SWE MEASUREMENTS

In this work, we have investigated how cardiac SWE measurements of material properties may be affected by the tapering of the IVS. The effects of tapering have already been investigated [31–33] in the non-medical field for waves with relatively high frequency contents (e.g. from 0.7 MHz to 3.3 MHz [32]), where multiple higher order symmetric and anti-symmetric modes are present. These studies showed that such higher modes, which only appear above well-defined values of the frequency-thickness product, can be reflected or converted into lower order modes when the thickness decreased sufficiently. However, the waves analysed in cardiac SWE have a relatively low frequency content (typically within 1000 Hz [19, 22, 27, 28]) and are therefore characterized mainly by the zero-order modes

Error in shear modulus estimation							
Excitation type	$x-t$ domain analysis	$f-k$ domain analysis					
		$h = 9$ mm	$h = 7.7$ mm	$h = 6.9$ mm	$h = 6$ mm	$h = 3$ mm	Best fit
ARF	-25.7% (left)	-2.9%	-1.7%	-1.7%	-1.7%	+10.4%	-1.7%
	-27.7% (right)						
Natural	-35.6% (left)	-5.2%	+7.9%	+19.2%	+39.3%	>+213.5%	+12.9%
	-44.7% (right)						

Table 3.2: Percentage error in the estimation of modelled  $G$  (3 kPa), based on the bulk shear speed extracted from  $x-t$  data and by fitting the simulated A0 of a linearly tapering plate. For the A0 fitting, theoretical curves were considered corresponding to flat plates with different constant values of thickness. 7.7 mm is the arithmetic mean of the thickness of the plate, 6.9 mm is its harmonic mean. The lowest RMS-PD curve at a thickness of 3 mm, for the natural wave, corresponded to a bulk shear speed greater than 3 m/s, outside the boundaries of the parameter space considered. The best fitting curve for the ARF data corresponds to a thickness of 6.7 mm, while for the natural wave it corresponds to a thickness of 7.3 mm. In the  $x-t$  domain column, two values of percentages are given, representing the values computed for the left and right halves of the M-lines.

and the first-order modes: the former are present at all frequency-thickness products, and, for the latter, cardiac thickness reductions are not large enough for mode conversion. Therefore, the effects described in literature would be hardly observed in the context of cardiac SWE.

Nevertheless, the thickness variation of the IVS can introduce effects that are relevant for cardiac SWE, especially for natural waves, as these are characterised by a stronger dispersion due to their lower frequency-thickness product. Both experiments and simulations showed that the wave speed extracted in the  $x-t$  domain can vary considerably along the plate with decreasing thickness, especially for waves with lower frequency contents (a  $\sim 10$  % speed decrease between the two branches in the experimental ARF data, and  $\sim 29$  % speed variation in the simulations of the natural waves, as shown in Figs. 3.5 and 3.8). As shown in Table 3.1, shear moduli obtained from the wave speed in the  $x-t$  domain severely underestimate the input value of  $G = 3$  kPa for both ARF ( $G = 2$  kPa) and natural waves ( $G = 1.7$  kPa and  $G = 1.0$  kPa for left and right wave, respectively) simulations. For comparison, the values of  $G$  extracted from  $x-t$  data in the simulated flat plate are  $G = 2.1$  kPa for the ARF wave and  $G_{NAT} = 1.8$  kPa for the natural wave. From these results, we conclude that thickness variations exacerbate the error that is already introduced by analysing waves in the IVS in the  $x-t$  domain, with an additional decrease in stiffness estimation of 3 % for ARF waves and even 27 % for natural waves.

Interestingly, as we mentioned in the introduction, Keijzer et al. [8] have recently reported that by using  $x-t$  domain analysis, a variability of up to approximately 40 % in the speed of naturally induced aortic valve closure (AVC) waves can be found between different studies, with variations in the order of 20 % between measurements within each study. As shown in Fig. 3.8, even the same measurement of natural wave propagation in a tapered plate could yield speeds that vary by 30 % from each other using the time domain analysis. It is also reasonable to assume that different hearts would present slightly different shapes, even among healthy volunteers, potentially increasing further the difference between measurements, as suggested by Tables 3.1 and 3.2. Based on our results, therefore, we suggest that geometry of the IVS plays a role in the variability of the speeds being reported.

In principle, analysing the propagation data in the  $f-k$  domain should provide a more

robust method of deriving  $G$ , since fitting the dispersion curves allows to determine the value of the bulk shear speed, which is directly related to the shear modulus [4, 11, 19, 20, 26, 27]. However, as is apparent from Tables 3.1 and 3.2, knowledge on the specific shape of the observed IVS is necessary in order to perform the fit correctly. Our results show, in fact, that neglecting the thickness variations can lead to considerable over- and underestimation of the shear modulus, and that a significant role is played by the exact shape of the plate, as opposed to the overall thickness reduction. The relevance of accounting for the correct thickness of the plate was also observed, for plates of constant thickness, by Maksuti et al. [42], who showed the error introduced by inaccurate thickness assumptions in arterial SWE.

The RMS-PD maps demonstrate a sub-region of the parameter space corresponding to dispersion curves with  $\text{RMS-PD} < 1\%$  (see Fig. 3.9). Within this region, especially for natural waves, small variations on the thickness axis can lead to big variations of the bulk shear speed with minimum RMS-PD, while still generating very similar dispersion curves. When using the global minimum of the RMS-PD map, even small errors in the reconstruction of the experimental or simulated dispersion curve could then lead to the wrong parameters. For this reason, it is our opinion that the global minimum of the two-parameters space should be avoided for reconstructing material properties of the IVS; rather, a priori knowledge of one of the two parameters (e.g. the thickness) should be used as input to identify the other.

In terms of clinical applications, our results confirm that  $f$ - $k$  data, rather than  $x$ - $t$  data, should be used to estimate the shear modulus from SWE measurements, as had already been suggested in literature [26, 42]. The thickness of the IVS can be measured for instance from B-mode images and used as input in the fitting procedure employed for the dispersion curves. In particular, to obtain more reliable results when there are thickness variations over the M-line, the thickness at each point should be measured and combined to compute some mean value, as opposed to averaging the total thickness variation. If precise information about the thickness is not available, our results suggest that overestimating the thickness leads to smaller errors than underestimating it, which is due to the shape of the dispersion curve of the A0 dispersion curve and corresponds with earlier observations [42]. A major challenge to this application, however, lies in the reconstruction of the experimental dispersion curve: resolution in the  $f$ - $k$  domain depends on the size (in space and time) of the acquisition of the  $x$ - $t$  signal, which is typically limited in cardiac applications to a few milliseconds over a couple of centimetres (determined by acquired field-of-view for the IVS) [22, 26]. The resulting resolution in the  $f$ - $k$  domain is thus low and potentially compounded to imaging artefacts and gross motion of the heart, which could lead to inaccuracies in the reconstruction of the dispersion curve, therefore affecting the result of the fit. This issue can be especially significant for natural waves, due to their longer wavelengths.

From a theoretical point of view, it is incorrect to talk about Lamb dispersion curves in plates of varying thickness, as these curves are defined for flat plates. Regardless, as a practical attempt to extract the shear modulus from wave measurements, it may still be useful to fit the known curves of a fluid-loaded flat plate to the  $f$ - $k$  data. Performing the fit by using the average thickness of the plate, for example, yielded relatively accurate results for the linearly tapered plate; however, it did not show any advantage over using the max-

imal thickness for the fit performed for the convex plate. Moreover, while the harmonic mean could be expected to provide a better approximation (since a wave traveling in a flat plate of equivalent thickness propagates with the same average speed as one traveling in a tapered plate), it did not yield better results. This suggests that an average thickness can be a useful first approximation that should be improved upon.

### 3.4.2. SIMULATIONS VERSUS EXPERIMENTS

The numerical settings of the simulations were validated by comparing the A0 curve of a simulated flat plate with the corresponding theoretical curve, showing a good correspondence between the two. Furthermore, the deceleration introduced by tapering observed in experiments is also present in the simulation data, confirming that our simulations can reliably reproduce wave physics also in the case of a tapered plate. To some extent, the main features of the propagation patterns in  $x-t$  domain of the experimental data are visible also in the simulations. However, in the simulations of the flat plate the splitting of the wavefront is not as clearly visible as in the experiments. Moreover, in the simulations, a positive wavefront appears during propagation, while this is not observed in the experimental data. The imperfect match between the simulated and experimental patterns could have several causes: for one, the wave source employed in our numerical study was meant to simulate the frequency content of the experimental wave, but the space-time distribution of the simulated source in the plate was kept much simpler. Additionally, the modelled plate is perfectly elastic, homogeneous and isotropic, whereas the plate used for the experiments could contain imperfections due to fabrication, which could in turn affect the wave patterns.

### 3.4.3. LIMITATIONS

In order to model a realistic cardiac shape, the fabricated phantom resulted in a relatively wide and thin plate with density just slightly higher than that of water. When submerged, the phantom tended to float around and curl at the thin edges. To prevent these effects, 3D printed PLA supports were fabricated and placed underneath and on top of the plate at two opposite ends. While the supports were never included in the field of view of the probe during experiments, their presence and contacts with the plate may also have affected the wave propagation by changing the actual boundary conditions of the wave guide.

To show the effects of tapering on propagation in  $x-t$  domain, we reported two values of speeds (corresponding to the first and second halves of the propagation). This approximation is useful to offer a clear, simple view of the effect of tapering, especially in the experimental data, where the resolution may not be high enough to discern local, small-magnitude variations. However, the propagation speed is a continuous function of space, since the tapering is, and the propagation trajectory is curved. By reporting only two values of constant speed, information on the precise variation of propagation speed over space is therefore lost.

Finally, to isolate the effects of tapering, several simplifications were made in our experimental and numerical models compared to actual cardiac settings: the IVS was modelled as a purely elastic, isotropic plate, whereas cardiac tissue is known to show both viscoelastic and anisotropic behaviour, as well as inhomogeneities near the valves. In conjunction with the three-dimensional curvature of a real IVS, all these parameters would

likely affect the trajectory, attenuation and dispersion of the propagating waves. Such effects were beyond the scope of this study, but should be included in future work to produce a more realistic model for the interpretation of SWE measurements in terms of medium properties.

### 3.5. CONCLUSIONS

In conclusion, this work shows experimentally and numerically that the specific (variable) thickness of the IVS can affect the estimation of the shear modulus obtained by SWE, especially when low frequency waves, such as natural waves, are tracked. Experiments show a deceleration of 11 % with the decreasing thickness. The numerical results show that neglecting tapering in  $f$ - $k$  analyses can result in errors greater than 30 % in shear modulus estimation, and that  $x$ - $t$  analyses are even less accurate. Finally, the exact tapering curve of the plate, rather than its absolute thickness variation, determines these effects, and more accurate results can be obtained when the constant thickness value considered for the  $f$ - $k$  analysis equals the mean thickness of the plate.

## REFERENCES

- [1] J. E. Brandenburg, S. F. Eby, P. Song, H. Zhao, J. S. Brault, S. Chen, and K.-N. An, *Ultrasound Elastography: The New Frontier in Direct Measurement of Muscle Stiffness*, Archives of Physical Medicine and Rehabilitation **95**, 2207 (2014).
- [2] L. C. Carlson, T. J. Hall, I. M. Rosado-Mendez, L. Mao, and H. Feltovich, *Quantitative assessment of cervical softening during pregnancy with shear wave elasticity imaging: an *in vivo* longitudinal study*, Interface Focus **9**, 20190030 (2019).
- [3] G. Ferraioli, C. Tinelli, B. Dal Bello, M. Zicchetti, G. Filice, and C. Filice, *Accuracy of real-time shear wave elastography for assessing liver fibrosis in chronic hepatitis C: A pilot study*, Hepatology **56**, 2125 (2012).
- [4] C. Pislaru, M. Urban, I. Nenadic, and J. Greenleaf, *Shearwave dispersion ultrasound vibrometry applied to in vivo myocardium*, in *2009 Annual International Conference of the IEEE Engineering in Medicine and Biology Society* (IEEE, 2009) pp. 2891–2894.
- [5] C. Pislaru, M. W. Urban, S. V. Pislaru, R. R. Kinnick, and J. F. Greenleaf, *Viscoelastic properties of normal and infarcted myocardium measured by a multifrequency shear wave method: Comparison with pressure-segment length method*, Ultrasound in Medicine and Biology **40**, 1785 (2014), arXiv:NIHMS150003 .
- [6] M. Strachinaru, J. G. Bosch, B. M. van Dalen, L. van Gils, A. F. van der Steen, N. de Jong, M. L. Geleijnse, and H. J. Vos, *Cardiac Shear Wave Elastography Using a Clinical Ultrasound System*, Ultrasound in Medicine and Biology (2017), 10.1016/j.ultrasmedbio.2017.04.012.
- [7] M. Strachinaru, J. G. Bosch, L. van Gils, B. M. van Dalen, A. F. L. Schinkel, A. F. W. van der Steen, N. de Jong, M. Michels, H. J. Vos, and M. L. Geleijnse, *Naturally occurring shear waves in healthy volunteers and hypertrophic cardiomyopathy patients*, Ultrasound in medicine & biology **00**, 1977 (2019).
- [8] L. B. Keijzer, M. Strachinaru, D. J. Bowen, M. L. Geleijnse, A. F. van der Steen, J. G. Bosch, N. de Jong, and H. J. Vos, *Reproducibility of Natural Shear Wave Elastography Measurements*, Ultrasound in Medicine & Biology **45**, 3172 (2019).
- [9] W. H. Gaasch, H. J. Levine, M. a. Quinones, and J. K. Alexander, *Left ventricular compliance: mechanisms and clinical implications*. The American journal of cardiology **38**, 645 (1976).
- [10] D. Westermann, M. Kasner, P. Steendijk, F. Spillmann, A. Riad, K. Weitmann, W. Hoffmann, W. Poller, M. Pauschinger, H.-P. Schultheiss, and C. Tschope, *Role of Left Ventricular Stiffness in Heart Failure With Normal Ejection Fraction*, Circulation **117**, 2051 (2008).
- [11] H. Kanai, *Propagation of spontaneously actuated pulsive vibration in human heart wall and in vivo viscoelasticity estimation*, IEEE Transactions on Ultrasonics, Ferroelectrics, and Frequency Control **52**, 1931 (2005).

- [12] C. Pislaru, P. A. Pellikka, and S. V. Pislaru, *Wave propagation of myocardial stretch: Correlation with myocardial stiffness*, *Basic Research in Cardiology* **109** (2014), 10.1007/s00395-014-0438-5.
- [13] H. J. Vos, B. M. van Dalen, I. Heinonen, J. G. Bosch, O. Sorop, D. J. Duncker, A. F. W. van der Steen, and N. de Jong, *Cardiac Shear Wave Velocity Detection in the Porcine Heart*. *Ultrasound in medicine & biology* **43**, 753 (2017).
- [14] P. Santos, A. M. Petrescu, J. Pedrosa, M. Orlowska, V. Komini, J.-U. Voigt, and J. D'hooge, *Natural Shear Wave Imaging in the Human Heart: Normal Values, Feasibility, and Reproducibility*, *IEEE Transactions on Ultrasonics, Ferroelectrics, and Frequency Control* **66**, 442 (2019).
- [15] M. Couade, M. Pernot, E. Messas, A. Bel, M. Ba, A. Hagege, M. Fink, and M. Tanter, *In Vivo quantitative mapping of myocardial stiffening and transmural anisotropy during the cardiac cycle*, *IEEE Transactions on Medical Imaging* **30**, 295 (2011).
- [16] M. Pernot, W.-N. Lee, A. Bel, P. Mateo, M. Couade, M. Tanter, B. Crozatier, and E. Messas, *Shear Wave Imaging of Passive Diastolic Myocardial Stiffness*, *JACC: Cardiovascular Imaging* **9**, 1023 (2016).
- [17] P. Song, X. Bi, D. C. Mellema, A. Manduca, M. W. Urban, J. F. Greenleaf, and S. Chen, *Quantitative Assessment of Left Ventricular Diastolic Stiffness Using Cardiac Shear Wave Elastography*, *Journal of Ultrasound in Medicine* **35**, 1419 (2016).
- [18] O. Villemain, M. Correia, E. Mousseaux, J. Baranger, S. Zarka, I. Podetti, G. Soulat, T. Damy, A. Hagege, M. Tanter, M. Pernot, and E. Messas, *Myocardial Stiffness Evaluation Using Noninvasive Shear Wave Imaging in Healthy and Hypertrophic Cardiomyopathic Adults*, *JACC: Cardiovascular Imaging* **12**, 1135 (2019).
- [19] H. Kanai, *2H-5 Regional Differences in Phase Velocity of Pulsive Wave Propagating Along the Heart Wall*, in *2006 IEEE Ultrasonics Symposium* (IEEE, 2006) pp. 760–763.
- [20] I. Z. Nenadic, M. W. Urban, S. A. Mitchell, and J. F. Greenleaf, *Lamb wave dispersion ultrasound vibrometry (LDUV) method for quantifying mechanical properties of viscoelastic solids*, *Physics in Medicine and Biology* **56**, 2245 (2011).
- [21] N. Bekki and S. A. Shintani, *Simple Dispersion Equation Based on Lamb-Wave Model for Propagating Pulsive Waves in Human Heart Wall*, *Journal of the Physical Society of Japan* **84**, 124802 (2015).
- [22] H. J. Vos, B. M. van Dalen, J. G. Bosch, A. F. van der Steen, and N. de Jong, *Myocardial passive shear wave detection*, in *2015 IEEE International Ultrasonics Symposium (IUS)* (IEEE, 2015) pp. 1–4.
- [23] J. Rose, *Ultrasonic Guided Waves in Solid Media*, Vol. 9781107048 (2014) pp. 1–512.
- [24] M. Bernal, I. Nenadic, M. W. Urban, and J. F. Greenleaf, *Material property estimation for tubes and arteries using ultrasound radiation force and analysis of propagating modes*, *The Journal of the Acoustical Society of America* **129**, 1344 (2011).

- [25] B. Brekke, L. C. Nilsen, J. Lund, H. Torp, T. Bjastad, B. H. Amundsen, A. Stoylen, and S. A. Aase, *Ultra-high frame rate tissue doppler imaging*, *Ultrasound in Medicine and Biology* **40** (2014), 10.1016/j.ultrasmedbio.2013.09.012.
- [26] A. Caenen, M. Pernot, D. A. Shcherbakova, L. Mertens, M. Kersemans, P. Segers, and A. Swillens, *Investigating Shear Wave Physics in a Generic Pediatric Left Ventricular Model via *In Vitro* Experiments and Finite Element Simulations*, *IEEE Transactions on Ultrasonics, Ferroelectrics, and Frequency Control* **64**, 349 (2017).
- [27] I. Z. Nenadic, M. W. Urban, C. Pislaru, D. Escobar, L. Vasconcelos, and J. F. Greenleaf, *In vivo open- and closed-chest measurements of left-ventricular myocardial viscoelasticity using lamb wave dispersion ultrasound vibrometry (LDUV): A feasibility study*, *Biomedical Physics and Engineering Express* **4** (2018), 10.1088/2057-1976/aabe41.
- [28] E. Maksuti, E. Widman, D. Larsson, M. W. Urban, M. Larsson, and A. Bjällmark, *Arterial Stiffness Estimation by Shear Wave Elastography: Validation in Phantoms with Mechanical Testing*, *Ultrasound in Medicine and Biology* **42**, 308 (2016).
- [29] P. H. M. Bovendeerd, J. Rijcken, D. H. Van Campen, A. J. G. Schoofs, K. Nicolay, and T. Arts, *Optimization of Left Ventricular Muscle Fiber Orientation*, (1999) pp. 285–296.
- [30] A. J. Baxi, C. S. Restrepo, D. Vargas, A. Marmol-Velez, D. Ocazonez, and H. Murillo, *Hypertrophic cardiomyopathy from A to Z: Genetics, pathophysiology, imaging, and management*, *Radiographics* **36** (2016), 10.1148/rg.2016150137.
- [31] Younho Cho, *Estimation of ultrasonic guided wave mode conversion in a plate with thickness variation*, *IEEE Transactions on Ultrasonics, Ferroelectrics and Frequency Control* **47**, 591 (2000).
- [32] M.-C. El-Kettani, F. Luppé, and A. Guillet, *Guided waves in a plate with linearly varying thickness: experimental and numerical results*, *Ultrasonics* **42**, 807 (2004).
- [33] M. E.-C. El-Kettani, M. V. Predoi, and P. Marical, *5K-6 Experimental and Numerical Studies on Lamb Waves Conversion in a Waveguide with Gaussian Section Variation*, in *2006 IEEE Ultrasonics Symposium* (IEEE, 2006) pp. 1185–1188.
- [34] L. Keijzer, A. Sabbadini, J. G. Bosch, M. D. Verweij, A. F. Van Der Steen, N. De Jong, and H. J. Vos, *Diffuse shear wave elastography in a thin plate phantom*, in *IEEE International Ultrasonics Symposium, IUS* (2017).
- [35] C. Kasai, K. Namekawa, A. Koyano, and R. Omoto, *Real-Time Two-Dimensional Blood Flow Imaging Using an Autocorrelation Technique*, *IEEE Transactions on Sonics and Ultrasonics* **32**, 458 (1985).
- [36] N. C. Rouze, M. H. Wang, M. L. Palmeri, and K. R. Nightingale, *Robust estimation of time-of-flight shear wave speed using a Radon sum transformation*, *Proceedings - IEEE Ultrasonics Symposium* **57**, 21 (2010).

- [37] M. L. Palmeri, A. C. Sharma, R. R. Bouchard, R. W. Nightingale, and K. R. Nightingale, *A finite-element method model of soft tissue response to impulsive acoustic radiation force*, IEEE Transactions on Ultrasonics, Ferroelectrics, and Frequency Control **52** (2005), 10.1109/TUFFC.2005.1561624.
- [38] I. Z. Nenadic, B. Qiang, M. W. Urban, L. H. De Araujo Vasconcelo, A. Nabavizadeh, A. Alizad, J. F. Greenleaf, and M. Fatemi, *Ultrasound bladder vibrometry method for measuring viscoelasticity of the bladder wall*, Physics in Medicine and Biology **58** (2013), 10.1088/0031-9155/58/8/2675.
- [39] A. Caenen, D. Shcherbakova, B. Verhegghe, C. Papadacci, M. Pernot, P. Segers, and A. Swillens, *A versatile and experimentally validated finite element model to assess the accuracy of shear wave elastography in a bounded viscoelastic medium*, IEEE Transactions on Ultrasonics, Ferroelectrics, and Frequency Control **62**, 439 (2015).
- [40] M. L. Palmeri, B. Qiang, S. Chen, and M. W. Urban, *Guidelines for finite-element modeling of acoustic radiation force-induced shear wave propagation in tissue-mimicking media*, IEEE Transactions on Ultrasonics, Ferroelectrics, and Frequency Control **64** (2017), 10.1109/TUFFC.2016.2641299.
- [41] S. L. Lipman, N. C. Rouze, M. L. Palmeri, and K. R. Nightingale, *Impact of Acoustic Radiation Force Excitation Geometry on Shear Wave Dispersion and Attenuation Estimates*, Ultrasound in Medicine and Biology **44** (2018), 10.1016/j.ultrasmedbio.2017.12.019.
- [42] E. Maksuti, F. Bini, S. Fiorentini, G. Blasi, M. W. Urban, F. Marinozzi, and M. Larson, *Influence of wall thickness and diameter on arterial shear wave elastography: A phantom and finite element study*, Physics in Medicine and Biology **62** (2017), 10.1088/1361-6560/aa591d.

# 4

## **LOCAL DISPERSION ANALYSIS IN BOUNDED MEDIA: AN IN-SILICO STUDY FOR CARDIAC APPLICATIONS**

## Abstract

Previous studies reported that the accuracy of Lamb wave analysis for cardiac elastography is affected by local thickness variations. A technique referred to as Local Phase Velocity Imaging (LPVI) was recently proposed for local elasticity measurements in bulk viscous tissues (e.g. the liver). The goal of the present work is to assess whether the same method can be employed to improve Lamb wave analysis in cardiac elastography. To achieve this, finite element models simulated the propagation of a shear wave in cardiac-mimicking plates of different geometries (e.g. with constant or varying thickness). The LPVI was applied to these datasets, showing that it can correctly reconstruct A0 and A1 dispersion curves. However, when comparing the shear modulus reconstructed by using a small (4 mm by 2.7 mm) LPVI window and an M-line of the same length, at various locations throughout a flat plate, LPVI did not show any significant improvement compared to the M-line analysis. These results were also confirmed in a tapered geometry, where using a long M-line yielded the most accurate estimate of the shear modulus, despite local thickness variations.

## 4.1. INTRODUCTION

Shear Wave Elastography (SWE) can provide clinically relevant information about biological tissues by measuring the speed of a shear wave propagating through them and relating it to the stiffness [1, 2]. An ultrasound transducer is used to non-invasively image the propagation of the pulsed wave, which can be induced by external means (e.g. by the transducer itself) [3–5] or by the natural physiology of the organ under investigation, e.g. the closing of a heart valve [6–8].

The most common approach to determine stiffness from a shear wave measurement makes use of time-of-flight measurements, i.e. tracking the movement over time of a specific feature of the pulsed wave (e.g. the peak particle displacement or peak particle velocity) to determine the propagation speed [3, 5, 7–14]. This approach assumes that the measured speed depends only on the stiffness and the density of the medium, which is the case for the shear speed in a bulk elastic material. However, time-of-flight measurements are inadequate to reconstruct stiffness in media where the propagation speed, or more precisely, the phase speed is dispersive, i.e. dependent on the frequency of the wave [15, 16].

A different approach consists in analysing the tracked wave in the frequency-wavenumber ( $f$ - $k$ ) domain. This can be done by considering the space-time propagation along one line of virtual receivers (M-line) and applying to this data a 2D Fast Fourier Transform (FFT). Data in the  $f$ - $k$  domain is useful to analyse waves with a dispersive behaviour, such as can be caused by viscosity or geometry. Several studies have reported reconstructing the dispersion curves and then using inversion algorithms, such as least-square fitting, to find the bulk shear speed and, therefore, the shear modulus of the medium [16–19]. Notably, when using the M-line approach, the longer the M-line, the higher the accuracy of the resolution in the transformed domain; as such, local information is usually lost with this approach.

Several methods to reconstruct local material properties with shear wave measurements have been proposed over the past few years. For instance, Ormachea, Parker et al. showed the possibility of reconstructing local wavenumbers by analysing diffuse, reverberant wavefields [20, 21]. Other approaches, specifically aimed at reconstructing local viscoelastic properties, employed the analysis of phase and amplitude decay of a single shear wave at varying distances from the source [22], or local model-based estimators to analyse the shear wave patterns [23, 24].

Recently, Kijanka and Urban proposed a local phase velocity imaging technique involving the local analysis of shear wave propagation in a short-space frequency-wavenumber domain [25, 26], based on a local wavenumber analysis procedure used in non-destructive testing [27]. In particular, this method was shown to retrieve local phase speeds more accurately than other methods [25], allowing for instance the imaging of small inclusions. Moreover, the LPVI approach was used to accurately and locally reconstruct viscosity-induced dispersion curves [26]. In contrast with the more common M-line approach, the results shown with the LPVI technique were extracted from relatively small windows (in the order of millimetres, as opposed to the centimetres typical of M-lines).

The LPVI approach could also be beneficial for performing SWE in media whose thickness is comparable to the wavelength of the shear wave, such as arterial walls [17], car-

diac muscle [6, 28] and the cornea [29], where Lamb (or at least Lamb-like) behaviour is observed. Lamb waves are characterised by two infinite sets of guided modes, either symmetric or antisymmetric. Each mode corresponds to a curve that associates every frequency to a different value of phase speed, depending on the material properties and the thickness of the plate [30, 31]. The benefit offered by LPVI would be to reconstruct Lamb dispersion curves locally, therefore accounting for local parameter variations (e.g. of thickness).

Reconstructing a Lamb mode locally would be particularly important for cardiac applications, since the thickness of the interventricular septum (IVS) can vary considerably from base to apex [32]. In fact, as we showed in the previous chapter, this thickness variation can introduce errors in stiffness estimation, when analysing in the  $f-k$  domain data extracted from an M-line (referred to in this paper as “ $f-k$  domain M-line approach”) [33]. These errors were especially significant (up to more than 200 % deviation from the true stiffness) when analysing low frequency waves, since Lamb dispersion is more pronounced at low frequencies.

The present work investigates whether the LPVI technique could prove useful for cardiac SWE to improve local stiffness estimation. More specifically, we aim to answer three questions: (i) whether LPVI can reconstruct Lamb dispersion curves in a muscle-like flat plate, (ii) whether in such a medium LPVI is more accurate in stiffness estimation than the  $f-k$  domain M-line approach, and (iii) whether LPVI improves stiffness estimation in more realistic cardiac geometries (tapered plates) for low frequency waves. To perform this study, finite element simulations are used to model waves with low and high frequency content (10-200 Hz and 10-600 Hz, respectively) in both flat and tapered septal models. The validity and accuracy of the LPVI approach is studied for various LPVI window sizes in a flat IVS-like plate for a high frequency wave (10- 600 Hz), simulating an Acoustic Radiation Force (ARF) push pulse. The resulting reconstructed 2D stiffness map was compared with that of the traditional  $f-k$  domain analysis of M-lines. Finally, LPVI is applied to a low frequency simulation (10-200 Hz), representing cardiac natural waves, in a linearly tapered plate, and its results are again compared to the stiffness estimations of the  $f-k$  domain analysis of M-lines.

## 4.2. METHODS

### 4.2.1. NUMERICAL SETUP

The simulated data was obtained using the same numerical implementation employed in the previous chapter, where a detailed description can be found. In brief, Abaqus CAE (Abaqus Inc., Providence, RI, U.S.A.) was used to model a 4 cm long, elastic, quasi-incompressible plate immersed in water. The thickness of the plate was either 9 mm, or decreased from 9 mm to 3 mm from the left to the right ends (see Fig. 4.1). The shear modulus  $G$  was equal to 3 kPa, the bulk shear speed was 1.69 m/s, the density 1045 kg/m<sup>3</sup> and the Poisson's ratio was 0.49999.

The plate was meshed with quadrilateral elements with a length and thickness of 0.1 mm (for the flat plate) or length of 0.2 mm and thickness between 0.2 and 0.07 mm (for the tapered plate). These mesh sizes ensure that frequencies up to 600 Hz are sampled with at least 15 points per wavelength, based on the bulk shear speed. The solution computed

by Abaqus was then sampled with a temporal resolution of 0.038 ms, corresponding to at least 43 samples per period in the frequency range mentioned.

A Gaussian-shaped vertical displacement pulse with peak amplitude of 0.2 mm was applied to the left edge of the plate in the transversal direction (see Fig. 4.1), simulating the wave source. The pulse simulating natural waves had a total duration of 10 ms, while the ARF wave was modelled with a 2 ms pulse, corresponding to full-width half-maximum frequency contents of around 100 Hz and 500 Hz, respectively [4, 16, 34, 35]. The wave propagation was simulated for a total duration of 40 ms, using an explicit solver.

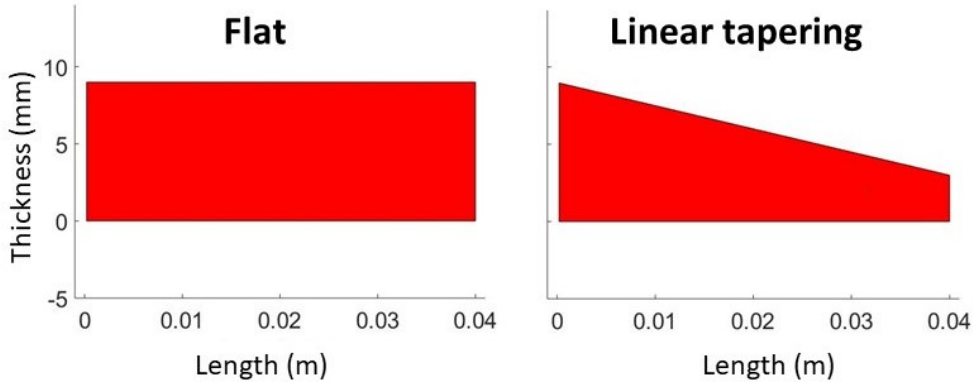


Figure 4.1: The two geometries of plates that were simulated: flat (left) and linearly tapered (right). In both, the thickness at the left side is 9 mm. In the tapered plate, the thickness decreases linearly until it reaches 3 mm at the right side.

#### 4.2.2. LPVI ANALYSIS

While a detailed description of the LPVI method can be found in the works of Kijanka and Urban [25], we report briefly the implementation employed in the present work.

The simulated dataset in Abaqus is a 3D matrix of displacements at coordinates  $t$ - $x$ - $y$  (time, lateral direction, axial direction). The basic blueprint of the LPVI approach consists of applying a 1D Fast Fourier Transform (FFT) in the time direction, converting the dataset into a  $f$ - $x$ - $y$  matrix. Then, for each frequency of interest  $f_i$ , the 2D matrix  $f_i$ - $x$ - $y$  is windowed, zeroing out all data outside of the window. The data inside the window is then transformed using a 2D FFT along the spatial dimensions, resulting in the matrix  $K(f_i, k_{x;m}, k_{y;n})$ , where  $k_{x;m}$  and  $k_{y;n}$  are the wavenumbers in the lateral and axial direction, respectively. For a given  $f_i$ , the maximum of  $K$  is assumed to correspond to the dispersion curve. Therefore, the wavevector  $(k_{x;i}, k_{y;i})$  at the maximum of  $K(f_i, k_{x;m}, k_{y;n})$  is identified and used to calculate the phase speed at frequency  $f_i$ :

$$|V(f_i, k_{x;i}, k_{y;i})| = |\mathbf{max}_{(m,n)}(V(f_i, k_{x;m}, k_{y;n}))|, \quad (4.1)$$

$$k_i = \sqrt{k_{x;i}^2 + k_{y;i}^2}, \quad (4.2)$$

$$C_{ph}^i = 2\pi f_i / k_i \quad (4.3)$$

In our implementation, before applying the FFT in the temporal direction, the particle displacement values corresponding to the last 0.18 ms were artificially tapered to zero with a cosine window; then, the entire matrix was padded on both ends of the  $t$  axis with 212 zero elements; finally, the matrix was artificially down-sampled, increasing the distance of consecutive points on the  $t$ -axis by a factor 10. This processing steps reduced windowing-related artefacts in the Fourier domain, while increasing the frequency step to a  $\Delta f$  of about 4 Hz.

To isolate a local region of interest, a 2D Tukey window was applied at each frequency to the  $f_i$ - $x$ - $y$  data. Each side of the Tukey window had an  $r$ -factor of 0.33. Several window widths were investigated, ranging from 4 mm to 29 mm (i.e. from 10 % to approximately 70 % of the plate length), while in the  $y$ -direction the window height was kept to 30 % of the local thickness: in a flat plate, this meant a height of 2.7 mm; in a tapered plate, the window was also tapered, so that, at each  $x$ -coordinate, the height of the window corresponded to 30 % of the plate thickness there. In the tapered plate, it was not possible to directly apply a 2D FFT to the entire window as the mesh grid is not rectangular. Therefore, the window was first transformed with a 1D FFT into a  $f_i$ - $k_x$ - $y$  matrix, then the  $y$  data at each  $k_x$  coordinate was also transformed into wavenumbers.

Repeating this procedure for different frequencies  $f_i$  results in reconstructing the dispersion curve of the wave, localised within the given window.

#### 4.2.3. $f$ - $k$ DOMAIN M-LINE ANALYSIS

For the  $f$ - $k$  domain M-line analysis, space-time simulated propagation was tracked along a single line, centred at the centre point of the window used for the LPVI approach. This data was further processed with a Tukey window with cosine fraction  $r = 0.2$ . A 2D FFT was then applied to transform the propagation data to the  $f$ - $k_x$  domain, in which the areas of maximum amplitude were assumed to correspond to the dispersion curves. The  $f$ - $k_x$  data was then masked, filtering out amplitudes below 20 % of the maximum.

#### 4.2.4. SHEAR MODULUS ESTIMATION

The curves extracted from the M-lines and the LPVI windows were then compared to the theoretical zero-order antisymmetric (A0) curves, each with a different combination of bulk shear speed and thickness. As was done in Chapter 3, a Root Mean Squared Percentage Difference (RMS-PD) error function was introduced to quantify the correspondence:

$$E = \sqrt{\sum_i^N \frac{(100(k_i - k_i^T) / k_i^T)^2}{N}} \quad (4.4)$$

where  $E$  is the RMS-PD error,  $k_i$  is the wavenumber of the extracted curve at the  $i^{th}$  frequency,  $k_i^T$  is the wavenumber of the chosen theoretical curve at the same frequency, and the sum runs over all  $N$  frequencies at which the curve was extracted. The RMS-PD was then calculated for theoretical curves corresponding to bulk shear speeds between 0.5 and 3m/s with a resolution of 0.001 m/s and thicknesses between 2 and 10 mm with a resolution of 0.1 mm. The bulk shear speed of the extracted curve was then estimated by identifying the theoretical curve with lowest RMS-PD, for a fixed value of thickness equal to the average thickness of the plate in the region of interest. Finally, the shear modulus was calculated as  $G = \rho c^2$ , where  $\rho$  is the density of mass ( $\text{kg/m}^3$ ) and  $c$  is the bulk shear speed.

#### 4.2.5. SHEAR MODULUS 2D MAPS

2D shear modulus maps were obtained for the flat plate by moving the centre position of the window and the M-line within the plate. The window width and M-line length had a constant value of 4 mm. The height of the window was 2.7 mm. The  $x$ -coordinate of the window centre ranged between 6 and 34 mm, whereas the  $y$ -coordinate varied between 15 % and 85 % of the local thickness of the plate. Before calculating the RMS-PD values, all the reconstructed curves were further processed by removing all the points ( $k_{x,m}$ ,  $k_{y,n}$ ) that were further from the theoretical A0 curve than half the distance between the theoretical curves for the A0 and A1 modes. This data removal was performed to guarantee that only data corresponding to the A0 mode was used for calculating the RMS-PD, and no interference with data of the A1 curve would occur.

### 4.3. RESULTS

#### 4.3.1. VALIDATION OF LPVI IN A PLATE (FLAT PLATE, ARF WAVE)

Our implementation of the LPVI algorithm was first tested using a relatively long window (2 cm long) in a flat plate with ARF pulse excitation. The height of the window was 2.7 mm. The window was centred at different  $x$ -coordinates, ranging from 1 cm to 3 cm, while the  $y$ -coordinate of the centre of the window remained fixed at 7.65 mm. For each location of the window, the phase speed was extracted using the LPVI at two frequencies, 100 Hz and 400 Hz. The extracted phase speeds are shown in Fig. 4.2, together with the theoretical values expected for the A0 mode at the same frequencies. Calculating the average phase speed and standard deviation at each frequency, we conclude that the speeds extracted using the LPVI approach are consistent with the theoretical values (see Table 4.1).

	Average $c_{ph}$	Standard deviation	Theoretical $c_{ph}$
<b>100 Hz</b>	1.296 m/s	0.016 m/s	1.292 m/s
<b>400 Hz</b>	1.410 m/s	0.015 m/s	1.421 m/s

Table 4.1: Extracted phase speed at 100 Hz and 400 Hz, averaged over 11 locations along the  $x$ -axis, with standard deviation and reference theoretical value for the A0 mode.

Next, we employed the LPVI to reconstruct the dispersion curve within the 2 cm long,

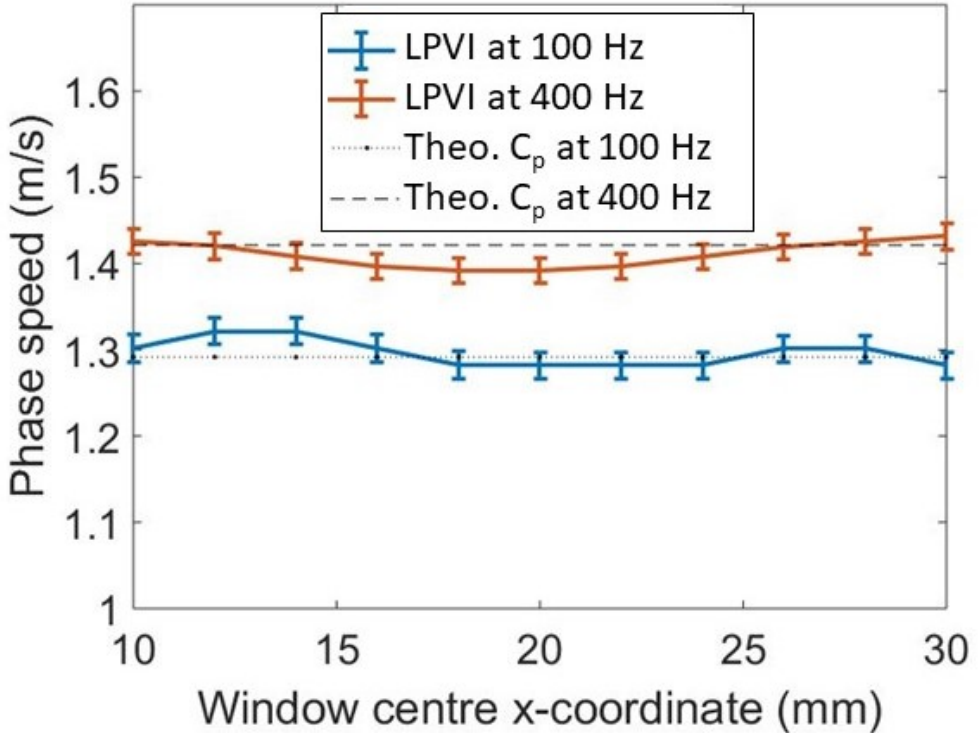


Figure 4.2: Phase speeds extracted using the LPVI technique at different  $x$  coordinates at frequencies of 100 Hz (blue) and 400 Hz (red) for a simulated ARF-induced wave. The error bars show the standard deviation. The dotted and dashed lines represent the theoretical phase speeds of the A0 Lamb mode at those frequencies, respectively.

2.7 mm high window, at frequencies between 10 Hz and 600 Hz with a sampling interval of 5 Hz. Along the  $x$ -axis, the centre of the window coincided with the centre of the plate. Along the  $y$ -axis, two locations of the centre of the window were considered (see Fig. 4.3): close to the top surface (7.65 mm) and at the axial centre of the plate (4.5 mm). The LPVI-derived and theoretical dispersion characteristics matched well for the window near the top surface (left panel of Fig. 4.3). For the axial centre of the plate (right panel of Fig. 4.3), both the A0 and A1 modes are detected by the LPVI technique. This agrees with the findings of our previous chapter.

#### 4.3.2. COMPARING LPVI AND $f$ - $k$ DOMAIN M-LINE AT DIFFERENT EXTRACTION LENGTHS (FLAT PLATE, ARF WAVE)

The accuracy of the shear modulus estimation with the LPVI method was investigated for a fixed window height of 2.7 mm and window widths varying between 4 mm and 29.2 mm. The centre of the window was placed at  $x$ - and  $y$ - coordinates of 2 cm and 7.65 mm, respectively; this location was chosen to avoid proximity to the boundaries on the  $x$ -axis,

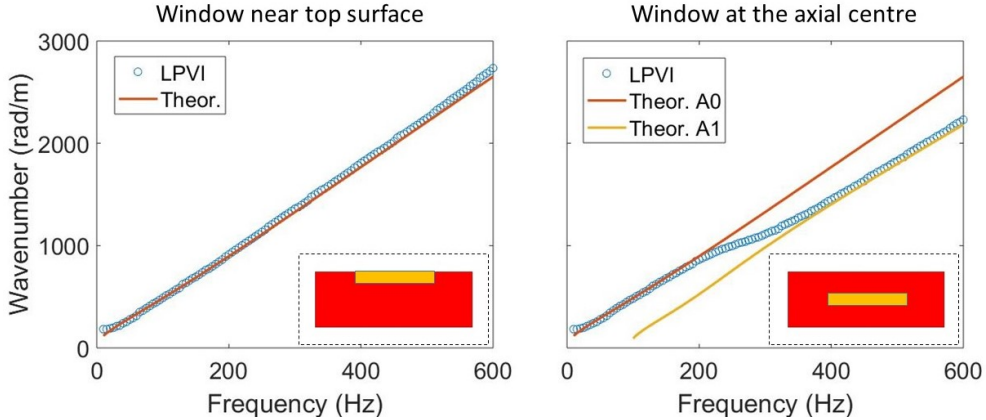


Figure 4.3: Dispersion curves reconstructed with the LPVI technique (blue circles) and obtained with a simulated ARF-induced wave, for windows centred vertically near the top surface (left plot) and near the plate axial centre (right plot). The red and yellow lines represent the theoretical dispersion curves for the A0 and A1 modes, respectively. In the bottom right corner the plate (in red) and the LPVI window (in yellow) are shown.

while also ensuring that only the A0 mode was included in the analysis. Each window was then compared to an M-line with the same length and centre-point coordinates. Figure 4.4 shows the results of this comparison, expressing the extracted values of  $G$  as percentage deviations from the true value (3 kPa). At the coordinates considered here, the LPVI yields more accurate values of  $G$  than the  $f$ - $k$  domain M-line analysis when the window width and M-line length are shorter than 24 mm. Window widths smaller than 4 mm were also tested, but failed to reconstruct the A0 mode (data not shown).

Subsequently, a LPVI window and an M-line of 4 mm were used to reconstruct the 2D shear stiffness map of the plate. Figure 4.5 shows, for both approaches, the variation between reconstructed and true values of the shear modulus  $G$ , expressed as a percentage of the true value. The absolute mean variation from the theoretical value and its standard deviation are reported in Table 4.2 for both approaches, showing comparable results: on average, the error in  $G$  for the LPVI approach is roughly 2 % lower than that of the  $f$ - $k$  domain M-line analysis.

	Average $ \Delta G/G $	Standard deviation
<b>LPVI</b>	10.8 %	15.9 %
<b>M-line</b>	13.0 %	17.3 %

Table 4.2: Average and standard deviation of the absolute percentage deviation from the true value of  $G$ , retrieved from the 2D maps obtained using the LPVI and M-line approaches for the flat plate.

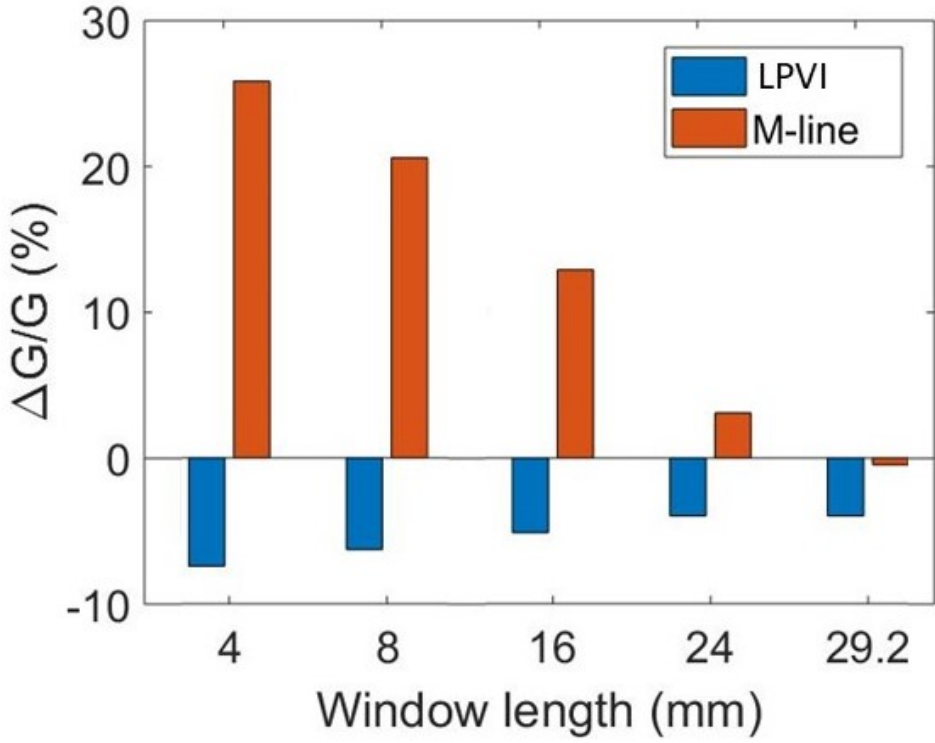


Figure 4.4: Percentage deviation of the extracted bulk shear speed from the true value in a flat plate, for different sizes of LPVI windows (in blue) and M-lines (in red). The A0 curves were extracted between 10 and 600 Hz from a simulation of ARF-induced waves.

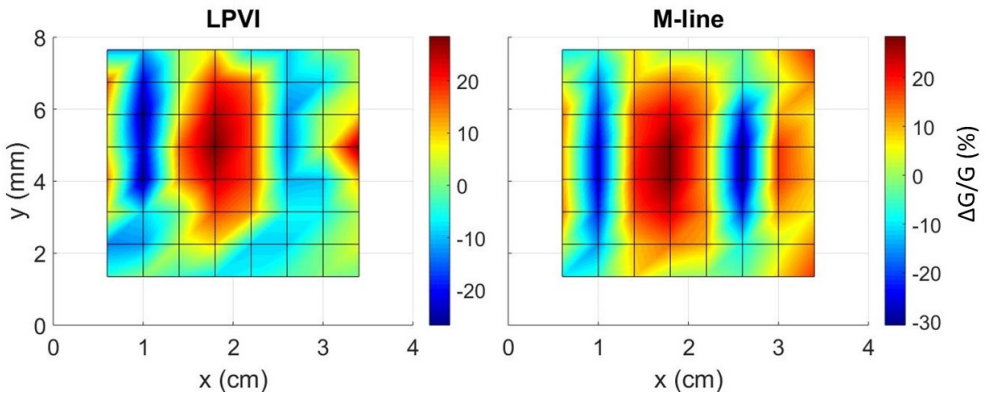


Figure 4.5: 2D shear modulus maps of the flat plate, reconstructed using an LPVI window (left) and an M-line (right) with a length of 4 mm. The colors represent the percentage deviation from the true value of  $G$  (3 kPa).

### 4.3.3. LPVI IN TAPERED PLATES (LINEARLY TAPERED PLATE, NATURALLY-INDUCED WAVE)

The performance of the LPVI-technique for natural cardiac waves, which are more sensitive to thickness variations due to their lower frequency content (up to 200 Hz), is demonstrated in Fig. 4.6 for a linearly tapered plate. Similarly to Fig. 4.5, Fig. 4.6 shows the 2D shear stiffness maps reconstructed using the LPVI approach (left) and the  $f$ - $k$  domain M-line analysis, using a 4 mm long and 2.7 mm high window and a 4 mm long M-line. The average and standard deviation of the absolute percentage deviations from the true value of  $G$  (3 kPa) is shown in Table 4.3. On average, both methods show an absolute deviation of around 18 % from the true value of  $G$ . For comparison, the value of  $G$  reconstructed by analysing a 2 cm long M-line in the middle of the plate is just 1.9 % larger than the true value.

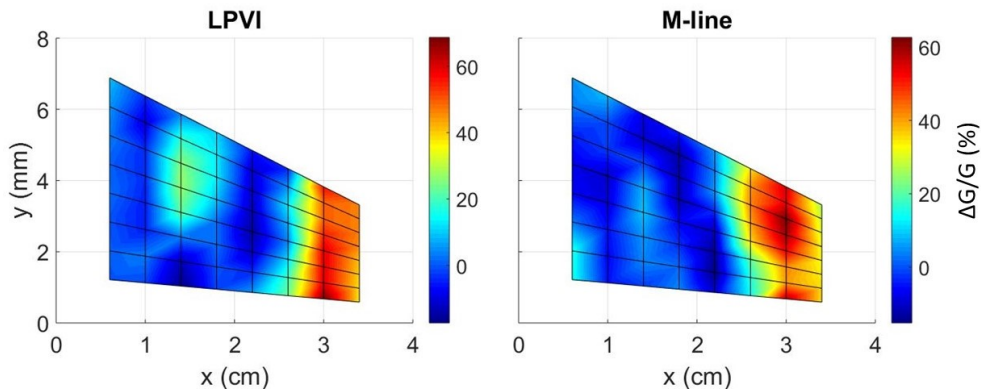


Figure 4.6: 2D shear modulus maps of the tapered plate, reconstructed using an LPVI window (left) and an M-line (right) with a length of 4 mm. The colors represent the percentage deviation from the true value of  $G$  (3 kPa).

	Average $ \Delta G/G $	Standard deviation
<b>LPVI</b>	18.8 %	23.3 %
<b>M-line</b>	18.7 %	22.6 %

Table 4.3: Average and standard deviation of the absolute percentage deviation from the true value of  $G$ , retrieved from the 2D maps obtained using the LPVI and M-line approaches for the tapered plate.

The tapered plate was then analysed at its axial centre and different  $x$ -coordinates, from 0.6 to 3.4 cm, using 4 mm long LPVI windows of different heights: one as thick as 30 % of the local plate thickness, the other spanning the entire local thickness. The resulting values of  $G$  are shown in Fig. 4.7, expressed as percentage variations from the true value (3 kPa) and compared to those obtained from a 4 mm long and 40 mm long M-lines at the same locations. In both geometries, the long M-line yields the most accurate result; both window heights produce, on average, comparable results (approximately 18 % of average

error), slightly more accurate than the short M-line (approximately 21 % of average error).

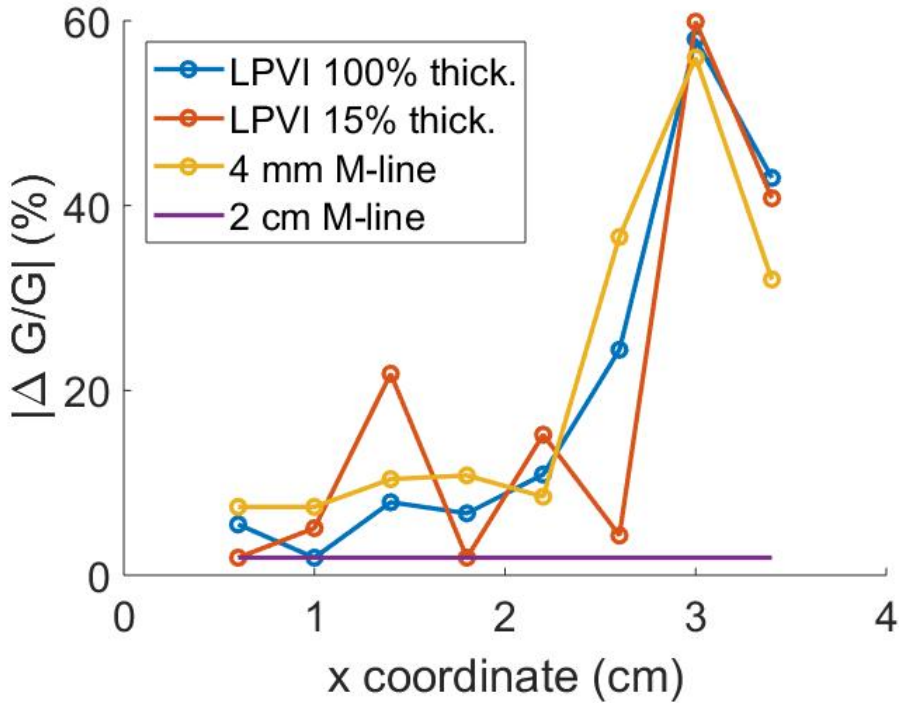


Figure 4.7: Comparison between the extracted values of  $G$  from the LPVI approach and the  $f$ - $k$  domain M-line analysis. The LPVI windows were 4 mm long, with heights equal to 30 % and 100 % of the local thickness of the plate. The two M-lines considered were 4 mm and 2 cm long.

#### 4.4. DISCUSSION

In this chapter we have investigated whether the LPVI technique, proposed in literature for viscoelastic bulk media [25, 36], can be applied to bounded elastic media. More specifically, we have investigated this technique for SWE applied to the heart muscle, which poses intrinsic challenges that could not be addressed in studies focusing on bulk media: (i) the dispersive behaviour of waves due to the plate-like structure of the IVS is different from the dispersive behaviour due to viscosity, (ii) several modes of propagation can be present at once, and (iii) the ability to detect specific Lamb modes that are excited will depend on the depth within the plate. For example, a 4 mm square window as was used in the previous studies could simultaneously collect data from regions with different modes. Moreover, while the accuracy of the LPVI approach was validated in the studies mentioned above, it was not compared to the  $f$ - $k$  domain M-lines approach with similar line lengths. As such, the performance of the LPVI approach remained to be determined for plate structures.

The implementation of the LPVI technique in our work differs slightly from that de-

scribed in literature. In particular, our work only involves a single propagating wave, as opposed to two pulses coming from opposite directions. Moreover, in our case the choice of dimensions for the LPVI window was at least partially determined by the physics involved in our study: 2.7 mm was the largest window height that still allowed to only detect the A0 mode near the top surface of the plates, and as such it was considered the best value to investigate the validity of the LPVI approach. On the other hand, the width of 4 mm was selected as the shortest width that could still reconstruct the A0 mode. Smaller windows, probably due to the limited number of datapoints they contained (less than 3 points per fixed  $y$ -coordinate for a 2 mm wide window), failed to reconstruct dispersion curves at most locations.

Applying the LPVI to a simulated shear wave in a flat plate, we have observed that this technique can, indeed, reconstruct Lamb dispersion curves in cardiac-mimicking settings. By using a rectangular window of 2.7 mm height and 2 cm length, we were able to study separate regions characterised by different modes, showing that the A1 mode coexists with A0 near the axial centre of the plate, whereas close to the top only A0 is excited (see Figure 4.3). This confirms previous observations obtained from  $f$ - $k$  domain M-line analyses [15, 16, 33]. Notably, the curve reconstructed near the axial centre transitions smoothly from A0 to A1 (see Fig. 4.3).

As is shown in Fig. 4.4, the LPVI method can reconstruct the bulk shear speeds of ARF-generated waves more accurately than an M-line of equal length and positioning. Intuitively, this result could be expected, since the LPVI method makes use of more data, i.e. data coming from a 2D window as opposed to a 1D line, to reconstruct the same information. Comparing the results of the two approaches at different locations, however, as is shown in Fig. 4.5, shows that the improvement provided by the LPVI approach is not the same everywhere. In fact, on average, the two methods produce comparable results. Moreover, both methods show a similar non-uniform pattern in the spatial distribution of their deviation from the true  $G$ . A possible explanation for this might be that, due to the proximity to the source location, the guided mode is not fully developed yet (see also the Supplementary Materials at the end of this chapter); however, further research will be necessary to investigate the validity of this hypothesis, possibly considering longer plates where larger distances from the source can be analysed. Regardless, it should be noted that the error in parameter estimation is relatively low, on average: a 10 % deviation from the true  $G$  corresponds to an error in estimated shear speed of approximately 0.08 m/s (about 5 % of the true value); this would likely not affect the overall accuracy of a clinical measurement, where the variations in measured shear speeds are usually much higher [14].

From a theoretical point of view, Lamb dispersion modes are derived for a plate with a constant thickness. As we have previously reported, errors can occur when the thickness of plate varies, especially for low-frequency (i.e. highly dispersive) waves. In that case, the average thickness can reduce the error, but it is an inadequate approximation if there are large variations over the length of the measurement section considered. If this length is small, on the other hand, the approximation should describe a situation closer to the truth and, therefore, yield more accurate results. While we had hypothesized that the LPVI could provide such improved results, our results do not support this: despite the thickness variation, extracting the value of  $G$  by analysing a 2 cm long M-line in the centre of the

plate yielded a better result (1.9 % error) than using either a 4 mm long M-line or a 4 mm by 2.7 mm window at the same location (14.1 % error in both cases). The same conclusion can be drawn when considering the average values of  $G$  extracted throughout the plate (errors of 18.8 % and 18.7 % for LPVI and M-line approaches, respectively).

Analysing the data near the axial centre of the plates, we showed that using a short (4 mm) but high window, spanning the entire thickness of the plate, yielded better results than an equally short M-line. However, the long M-line still produced the most accurate results. This result suggests that the information retrieved from the perpendicular direction (the  $y$ -direction) plays a less significant role in reconstructing the dispersion curve. Notably, for the local measurements, the error increased towards the thin end of the plate. Reflections at the boundary are unlikely to be the cause of this increased error, as they were not observed in the data and are naturally filtered out by the  $f$ - $k$  domain approach. It should also be noted that the problem of incorporating areas where different modes can be detected was not an issue in these measurements, since only A0 is present at the low frequencies considered, and this mode has a uniform distribution over the entire thickness of the plate.

A limitation of the present work lies in the analysis of the central section of flat plates, where the LPVI approach reconstructs a curve that transitions from A0 to A1. Due to the smooth transition, it was not possible to fit the extracted curve entirely with the dispersion curve of any single theoretical mode to obtain the material properties. As a consequence, when analysing the central region of the plate, only the lower frequencies (corresponding to A0) could be analysed, reducing the amount of data available. Moreover, part of the transition region of the curve was included in the analysis because the cut-off was chosen in correspondence with the frequency at which the A1 mode was closer to the curve than the A0. This affected the accuracy of the reconstruction by introducing overestimations of the phase velocity.

Future work will be dedicated to obtaining a better understanding of the error distribution in the 2D stiffness maps, as well as developing and validating techniques to analyse several Lamb modes simultaneously. This could enable the use of taller windows (e.g. square windows) in flat plates, increasing the amount of information obtained from the  $y$ -direction and, potentially, improving the accuracy of the LPVI approach.

## 4.5. CONCLUSIONS

The LPVI technique can be used to perform SWE on IVS-like plates to reconstruct Lamb dispersion curves. Analysing in the  $f$ - $k$  domain M-lines that span comparable spatial domains, on average, yields equally accurate results, even in the presence of thickness variations.

## SUPPLEMENTARY MATERIALS

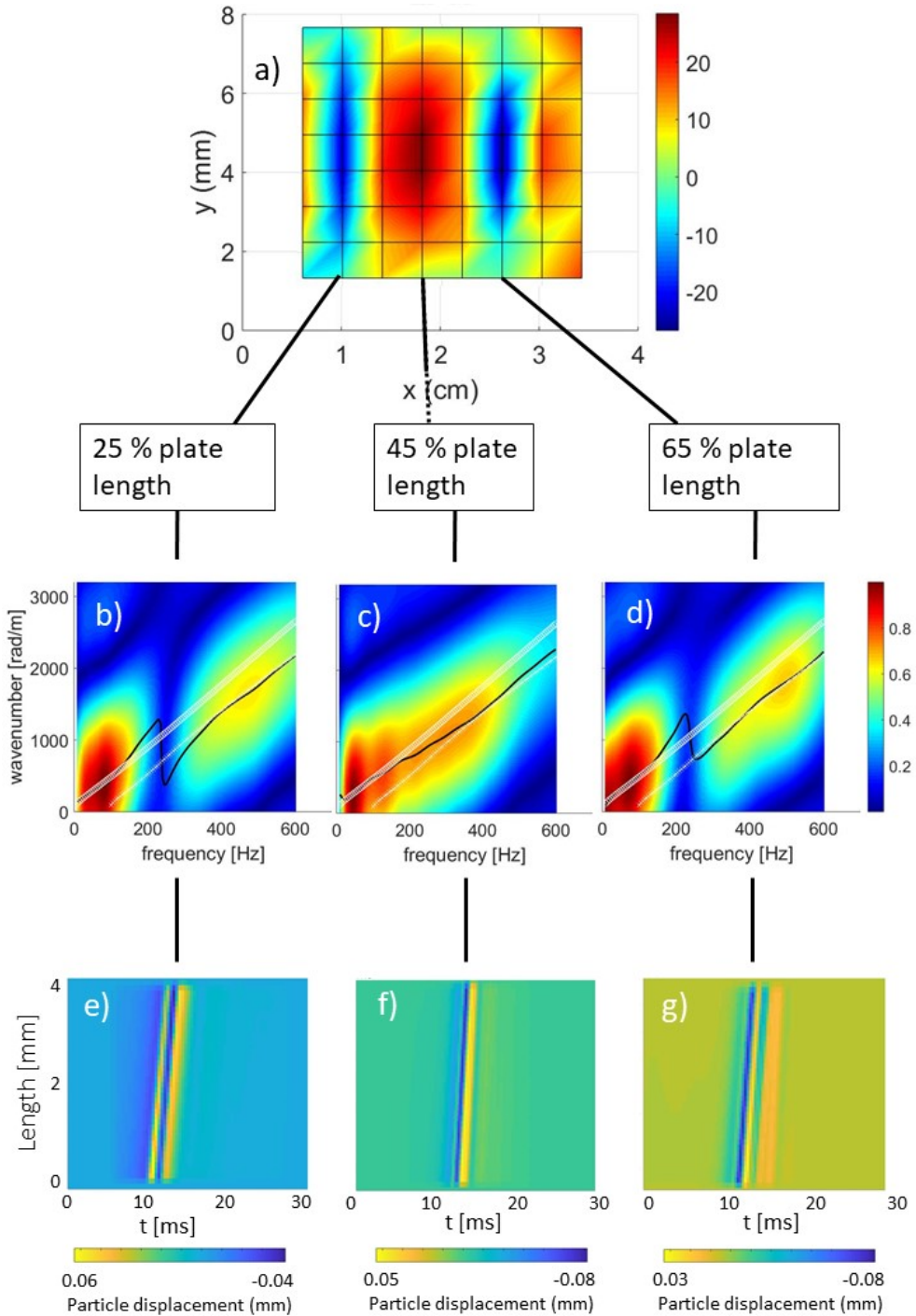


Figure 4.8: Panel a): 2D shear modulus error map reconstructed with the M-line approach in a flat plate for an ARF-induced wave. Panels b), c), d):  $f$ - $k$  domain representation of the shear wave measured along a 4 mm long M-line at  $y = 4.95$  mm, at different  $x$  coordinates. The black lines show the extracted dispersion curve, while the white circles and crosses show the theoretical A0 and A1 curves, respectively. Panels e), f), g):  $x$ - $t$  domain representation of the shear wave measured along a 4 mm long M-line at  $y = 4.95$  mm, at different  $x$  coordinates.

## REFERENCES

- [1] G. Ferraioli, C. Tinelli, B. Dal Bello, M. Zicchetti, G. Filice, and C. Filice, *Accuracy of real-time shear wave elastography for assessing liver fibrosis in chronic hepatitis C: A pilot study*, *Hepatology* **56**, 2125 (2012).
- [2] J. E. Brandenburg, S. F. Eby, P. Song, H. Zhao, J. S. Brault, S. Chen, and K.-N. An, *Ultrasound Elastography: The New Frontier in Direct Measurement of Muscle Stiffness*, *Archives of Physical Medicine and Rehabilitation* **95**, 2207 (2014).
- [3] M. L. Palmeri, M. H. Wang, J. J. Dahl, K. D. Frinkley, and K. R. Nightingale, *Quantifying Hepatic Shear Modulus In Vivo Using Acoustic Radiation Force*, *Ultrasound in Medicine and Biology* **34** (2008), 10.1016/j.ultrasmedbio.2007.10.009.
- [4] E. Maksuti, E. Widman, D. Larsson, M. W. Urban, M. Larsson, and A. Bjällmark, *Arterial Stiffness Estimation by Shear Wave Elastography: Validation in Phantoms with Mechanical Testing*, *Ultrasound in Medicine and Biology* **42**, 308 (2016).
- [5] O. Villemain, M. Correia, E. Mousseaux, J. Baranger, S. Zarka, I. Podetti, G. Soulat, T. Damy, A. Hagège, M. Tanter, M. Pernot, and E. Messas, *Myocardial Stiffness Evaluation Using Noninvasive Shear Wave Imaging in Healthy and Hypertrophic Cardiomyopathic Adults*, *JACC: Cardiovascular Imaging* **12**, 1135 (2019).
- [6] H. Kanai, *Propagation of spontaneously actuated pulsive vibration in human heart wall and in vivo viscoelasticity estimation*, *IEEE Transactions on Ultrasonics, Ferroelectrics, and Frequency Control* **52**, 1931 (2005).
- [7] P. Santos, A. M. Petrescu, J. Pedrosa, M. Orlowska, V. Komini, J.-U. Voigt, and J. D'hooge, *Natural Shear Wave Imaging in the Human Heart: Normal Values, Feasibility, and Reproducibility*, *IEEE Transactions on Ultrasonics, Ferroelectrics, and Frequency Control* **66**, 442 (2019).
- [8] M. Strachinaru, J. G. Bosch, L. van Gils, B. M. van Dalen, A. F. L. Schinkel, A. F. W. van der Steen, N. de Jong, M. Michels, H. J. Vos, and M. L. Geleijnse, *Naturally occurring shear waves in healthy volunteers and hypertrophic cardiomyopathy patients*, *Ultrasound in medicine & biology* **00**, 1977 (2019).
- [9] N. C. Rouze, M. H. Wang, M. L. Palmeri, and K. R. Nightingale, *Robust estimation of time-of-flight shear wave speed using a Radon sum transformation*, *Proceedings - IEEE Ultrasonics Symposium* **57**, 21 (2010).
- [10] M. Pernot, W.-N. Lee, A. Bel, P. Mateo, M. Couade, M. Tanter, B. Crozatier, and E. Messas, *Shear Wave Imaging of Passive Diastolic Myocardial Stiffness*, *JACC: Cardiovascular Imaging* **9**, 1023 (2016).
- [11] M. Strachinaru, J. G. Bosch, B. M. van Dalen, L. van Gils, A. F. van der Steen, N. de Jong, M. L. Geleijnse, and H. J. Vos, *Cardiac Shear Wave Elastography Using a Clinical Ultrasound System*, *Ultrasound in Medicine and Biology* (2017), 10.1016/j.ultrasmedbio.2017.04.012.

- [12] C. Amador Carrascal, S. Chen, A. Manduca, J. F. Greenleaf, and M. W. Urban, *Improved Shear Wave Group Velocity Estimation Method Based on Spatiotemporal Peak and Thresholding Motion Search*, IEEE Transactions on Ultrasonics, Ferroelectrics, and Frequency Control **64** (2017), 10.1109/TUFFC.2017.2652143.
- [13] H. J. Vos, B. M. van Dalen, I. Heinonen, J. G. Bosch, O. Sorop, D. J. Duncker, A. F. W. van der Steen, and N. de Jong, *Cardiac Shear Wave Velocity Detection in the Porcine Heart*. Ultrasound in medicine & biology **43**, 753 (2017).
- [14] L. B. Keijzer, M. Strachinaru, D. J. Bowen, M. L. Geleijnse, A. F. van der Steen, J. G. Bosch, N. de Jong, and H. J. Vos, *Reproducibility of Natural Shear Wave Elastography Measurements*, Ultrasound in Medicine & Biology **45**, 3172 (2019).
- [15] E. Maksuti, F. Bini, S. Fiorentini, G. Blasi, M. W. Urban, F. Marinozzi, and M. Larsson, *Influence of wall thickness and diameter on arterial shear wave elastography: A phantom and finite element study*, Physics in Medicine and Biology **62** (2017), 10.1088/1361-6560/aa591d.
- [16] A. Caenen, M. Pernot, D. A. Shcherbakova, L. Mertens, M. Kersemans, P. Segers, and A. Swillens, *Investigating Shear Wave Physics in a Generic Pediatric Left Ventricular Model via *In Vitro* Experiments and Finite Element Simulations*, IEEE Transactions on Ultrasonics, Ferroelectrics, and Frequency Control **64**, 349 (2017).
- [17] M. Bernal, I. Nenadic, M. W. Urban, and J. F. Greenleaf, *Material property estimation for tubes and arteries using ultrasound radiation force and analysis of propagating modes*, The Journal of the Acoustical Society of America **129**, 1344 (2011).
- [18] I. Z. Nenadic, M. W. Urban, S. A. Mitchell, and J. F. Greenleaf, *Lamb wave dispersion ultrasound vibrometry (LDUV) method for quantifying mechanical properties of viscoelastic solids*, Physics in Medicine and Biology **56**, 2245 (2011).
- [19] I. Z. Nenadic, M. W. Urban, C. Pislaru, D. Escobar, L. Vasconcelos, and J. F. Greenleaf, *In vivo open- and closed-chest measurements of left-ventricular myocardial viscoelasticity using lamb wave dispersion ultrasound vibrometry (LDUV): A feasibility study*, Biomedical Physics and Engineering Express **4** (2018), 10.1088/2057-1976/aabe41.
- [20] K. J. Parker, J. Ormachea, F. Zvietcovich, and B. Castaneda, *Reverberant shear wave fields and estimation of tissue properties*, Physics in Medicine and Biology **62** (2017), 10.1088/1361-6560/aa5201.
- [21] J. Ormachea, K. J. Parker, and R. G. Barr, *An initial study of complete 2D shear wave dispersion images using a reverberant shear wave field*, Physics in Medicine and Biology **64** (2019), 10.1088/1361-6560/ab2778.
- [22] E. Budelli, J. Brum, M. Bernal, T. Deffieux, M. Tanter, P. Lema, C. Negreira, and J. L. Gennisson, *A diffraction correction for storage and loss moduli imaging using radiation force based elastography*, Physics in Medicine and Biology **62** (2017), 10.1088/1361-6560/62/1/91.

- [23] J. H. Langdon, E. Elegbe, and S. A. Mcaleavey, *Single tracking location acoustic radiation force impulse viscoelasticity estimation (STL-VE): A method for measuring tissue viscoelastic parameters*, IEEE Transactions on Ultrasonics, Ferroelectrics, and Frequency Control **62** (2015), 10.1109/TUFFC.2014.006775.
- [24] R. J. Van Sloun, R. R. Wildeboer, H. Wijkstra, and M. Mischi, *Viscoelasticity Mapping by Identification of Local Shear Wave Dynamics*, IEEE Transactions on Ultrasonics, Ferroelectrics, and Frequency Control **64** (2017), 10.1109/TUFFC.2017.2743231.
- [25] P. Kijanka and M. W. Urban, *Local Phase Velocity Based Imaging: A New Technique Used for Ultrasound Shear Wave Elastography*, IEEE Transactions on Medical Imaging **38** (2019), 10.1109/TMI.2018.2874545.
- [26] P. Kijanka and M. W. Urban, *Local Phase Velocity Based Imaging (LPVI) of Viscoelastic Phantoms and Tissues*, IEEE Transactions on Ultrasonics, Ferroelectrics, and Frequency Control (2020), 10.1109/tuffc.2020.2968147.
- [27] E. B. Flynn, S. Y. Chong, G. J. Jarmer, and J. R. Lee, *Structural imaging through local wavenumber estimation of guided waves*, NDT and E International **59** (2013), 10.1016/j.ndteint.2013.04.003.
- [28] N. Bekki and S. A. Shintani, *Simple Dispersion Equation Based on Lamb-Wave Model for Propagating Pulsive Waves in Human Heart Wall*, Journal of the Physical Society of Japan **84**, 124802 (2015).
- [29] C. C. Shih, X. Qian, T. Ma, Z. Han, C. C. Huang, Q. Zhou, and K. K. Shung, *Quantitative assessment of thin-layer tissue viscoelastic properties using ultrasonic micro-elastography with lamb wave model*, IEEE Transactions on Medical Imaging **37** (2018), 10.1109/TMI.2018.2820157.
- [30] H. Lamb, *On Waves in an Elastic Plate*, Proceedings of the Royal Society A: Mathematical, Physical and Engineering Sciences **93**, 114 (1917).
- [31] J. Rose, *Ultrasonic Guided Waves in Solid Media*, Vol. 9781107048 (2014) pp. 1–512.
- [32] P. H. M. Bovendeerd, J. Rijcken, D. H. Van Campen, A. J. G. Schoofs, K. Nicolay, and T. Arts, *Optimization of Left Ventricular Muscle Fiber Orientation*, (1999) pp. 285–296.
- [33] A. Sabbadini, A. Caenen, H. J. Vos, N. de Jong, and M. D. Verweij, *Modelling Lamb waves in the septal wall of the heart*, The Journal of the Acoustical Society of America **146** (2019), 10.1121/1.5137654.
- [34] H. Kanai, *2H-5 Regional Differences in Phase Velocity of Pulsive Wave Propagating Along the Heart Wall*, in *2006 IEEE Ultrasonics Symposium* (IEEE, 2006) pp. 760–763.
- [35] H. J. Vos, B. M. van Dalen, J. G. Bosch, A. F. van der Steen, and N. de Jong, *Myocardial passive shear wave detection*, in *2015 IEEE International Ultrasonics Symposium (IUS)* (IEEE, 2015) pp. 1–4.
- [36] P. Kijanka and M. W. Urban, *Fast Local Phase Velocity-Based Imaging: Shear Wave Particle Velocity and Displacement Motion Study*, IEEE Transactions on Ultrasonics, Ferroelectrics, and Frequency Control **67** (2020), 10.1109/TUFFC.2019.2948512.



# 5

## PLANAR WAVE GUIDE CHARACTERIZATION BY MULTI-PARAMETER LAMB WAVE DISPERSION CURVE ANALYSIS

## Abstract

In recent years, several fitting techniques have been presented to reconstruct the parameters of a plate from its Lamb wave dispersion curves. Published studies show that these techniques can yield high accuracy results and have the potential of reconstructing several parameters at once. The precision with which parameters can be reconstructed by inverting Lamb wave dispersion curves, however, remains an open question of fundamental importance to many applications. In this work, we present an approach that allows both the simultaneous extraction of the thickness of a plate and the shear and compressional bulk wave sound speeds, as well as the provision of quantitative information on the precision with which these parameters can be extracted. As opposed to the error minimization algorithms commonly employed in fitting techniques, our approach compares a target curve to a database of theoretical ones that covers a given parameter space. For every point in the parameter space, a measure of dissimilarity (error) is calculated, thus showing not only the location of the minimum error, but also the distribution of the error itself. We use this approach to reconstruct the parameters of a plate from Finite Element simulations and experimental measurements of the zeroth order Lamb wave modes ( $A_0$  and  $S_0$ ), showing that the precision with which each parameter is reconstructed depends on the mode used, as well as the frequency range in which it is considered.

## 5.1. INTRODUCTION

In a variety of fields, from medical research to industrial applications, measurements of the propagation of a mechanical wave through a medium are used to reconstruct its material properties [1–6]. In the simple case of a fluid bulk medium, the propagation speed of a wave is proportional to the inverse square root of the density and the compressibility of the medium. However, when the object under investigation is a solid plate or a plate-like geometry, waves are characterized by sets of symmetric and antisymmetric dispersive wave modes. Waves characterised by these modes are referred to as Lamb waves [7]. The propagation speed of these wave modes depends not only on the elastic properties of the medium, but also on the product of its thickness and the frequency of the wave [7, 8].

Due to the dispersive behaviour of Lamb waves, time-of-flight measurements of wave speed cannot be employed directly to reconstruct the properties of a medium [9, 10], as shown also in Chapter 3 of this thesis. Rather, a common approach consists in assuming that a given combination of shear speed ( $c_T$ ), compressional speed ( $c_L$ ) and thickness ( $h$ ) defines uniquely a set of dispersion curves; based on this assumption, these three parameters can be reconstructed by extracting the dispersion curves from a measurement and then finding the parameters that generate the same (or most similar) curves [11–15]. Several techniques have already been developed to extract the dispersion curves from measured data and to solve the so-called inverse problem for one or more parameters simultaneously [12, 14–20]. In most of these studies, the accuracy of the techniques is then compared with benchmarking methods, such as mechanical testing or pulse-echo measurements. However, little to no information is available on the reliability of the Lamb dispersion curve approach: whether the solution is unique and independent of the inversion algorithm employed, how robust this approach is with respect to noise, how sensitive different modes are to the three parameters and whether this sensitivity depends on the frequency range available, and, in general, how precise the results are. This information, however, is crucial to assess whether and when this approach can be used in practical applications. If, for instance, two different sets of material properties generated similar A0 curves, and if noise would cause these curves to become indistinguishable, the inversion would not necessarily be able to distinguish between the two sets in practice.

In the first part of this work we present our approach to simultaneously extract  $c_T$ ,  $c_L$  and  $h$  from measured or simulated dispersion curves. In addition to parameter extraction, this method provides quantitative information on how sensitive a mode is to each of the three parameters, as well as an indication of whether a solution is at least locally unique. We then employ this method to show numerically how random noise applied to the dispersion curves in the wavenumber direction can affect the results. Moreover, we show how the sensitivity of the zeroth order wave modes (A0 and S0) to  $c_T$ ,  $c_L$  and  $h$  varies between modes and how it depends on the frequency range available. Finally, we show applications of our approach to simulated and experimental data.

## 5.2. SETUP

### 5.2.1. NUMERICAL SETUP

The Finite Element software package PZFlex (Onscale, Redwood City, CA, USA) was used to simulate the acoustic wave propagation of Lamb waves in a  $h = 1$  mm thick stainless

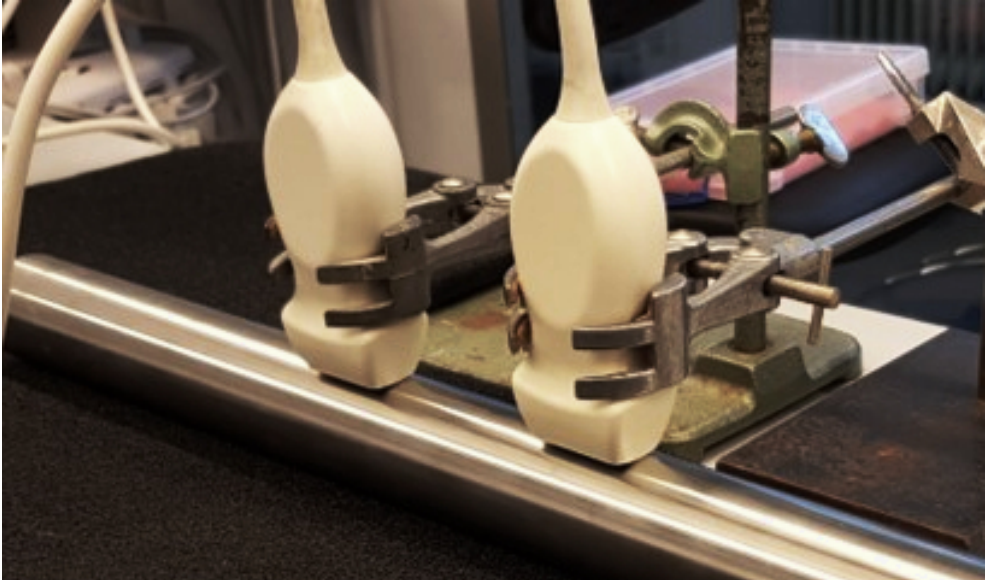


Figure 5.1: Experimental setup, consisting of two ATL P4-1 probes held in contact with a 1 mm thick stainless steel pipe.

steel plate, which was simulated using nominal values of  $c_L = 5800$  m/s and  $c_T = 3100$  m/s. Guided waves were excited in the plate by placing a small transducer on one of the surfaces and exciting it with a broadband ultrasound pulse with a center frequency of 2.7 MHz. Considering the lowest sound speed of the geometry, a mesh consisting of square grids with a length of 30 points per wavelength was defined to properly sample the guided waves. Along one of the surfaces of the plate, virtual receivers were placed over a distance of 90 mm to record the time signals of these waves. Finally, a 2D Fast Fourier Transform (FFT) was applied to visualize the propagating wave modes, i.e. the dispersion curves, in the  $f-k_x$  domain .

### 5.2.2. EXPERIMENTAL SETUP

The experiments were conducted on a 40mm -inner diameter 304-stainless steel pipe (nominal values:  $c_L = 5920$  m/s and  $c_T = 3141$  m/s) with a wall thickness of  $h = 1$ mm. Two ATL P4-1 probes (Philips, Bothell, WA, USA), one functioning as an ultrasound source and the other as a receiver, were placed in line on the pipe wall (see Fig. 5.1), with a center-to-center distance of 10 cm, and were driven with a Verasonics Vantage 256 (Verasonics Inc., Kirkland, WA, USA) system. A 1-cycle pulse with a center frequency of 2.25 MHz was used to excite one element of the source probe, and all 96 elements of the receiver probe were used to record the propagating guided waves.

## 5.3. METHODS

### 5.3.1. DISPERSION CURVE EXTRACTION

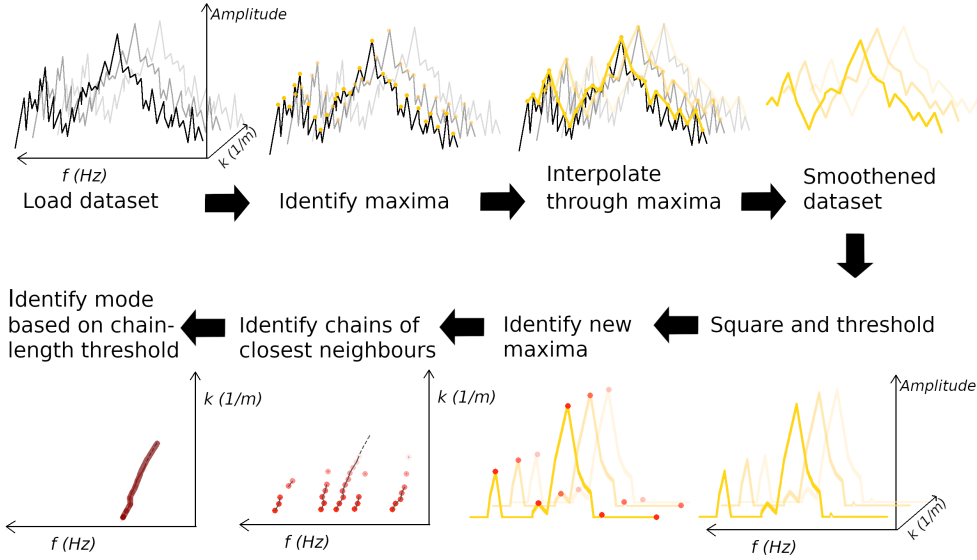


Figure 5.2: Algorithm to extract the dispersion curves from experimental data in the frequency-wavenumber domain.

### MEASURED DATA

The following procedure was adapted from [20] to isolate and extract the A0 and S0 modes (see Fig. 5.2). First, all the local maxima of the  $f$ - $k_x$  surface were found and connected by straight lines, so as to generate a new, smoother dataset. This interpolation removes the valleys between consecutive peaks, e.g. turning a sawtooth pattern into a straight line. The new dataset, converted to decibel scale, was then squared (to increase the prominence of the highest peaks) and thresholded (to remove the lower values), thus partially isolating the modes and removing noise. The local maxima of the treated data were then extracted again and stored into a database (e.g. " $data_A$ ").

The mode identification was then executed as a search for chains of neighbouring maxima: starting from a point in  $data_A$ , it was determined which (if any) other local maximum was the closest neighbour within a given radius; if such a point was found, the starting point would be moved from  $data_A$  into a different database (e.g. " $mode_1$ "), and the neighbour would become the next starting point. Once no neighbour was found within the searching radius, a new starting point was chosen from  $data_A$  and a new database (e.g. " $mode_2$ ") was created to store the next chain. Finally, spurious chains were separated from the real modes on the basis of chain length because a mode, being a set of points ordered along a curve, forms a consistently longer chain than randomly distributed spurious clusters of maxima). The modes themselves were identified on the basis of the order of appearance along the  $k_x$  direction: at every frequency, the  $k_x$  belonging to the A0 mode have a lower value than those belonging to the S0 mode.

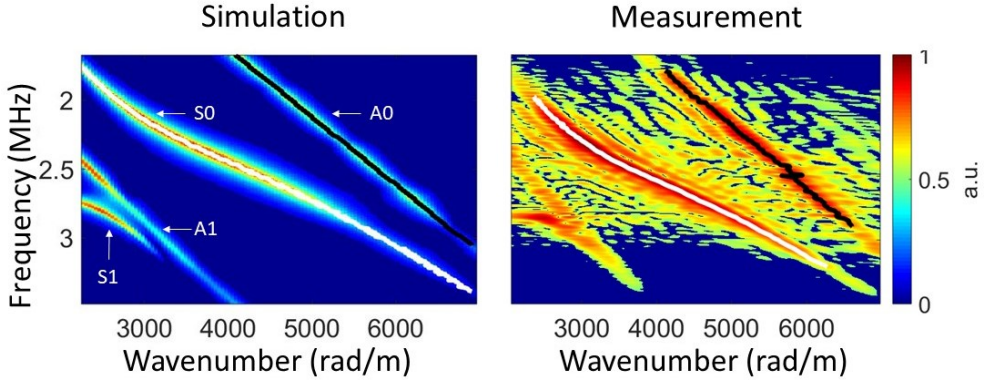


Figure 5.3: Magnitude of a 2D FFT applied to time signals obtained on the surface of a 1mm-thick simulated stainless steel plate (left) and measured on the surface of a 1 mm-thick stainless steel pipe (right). The white lines show the reconstructed S0 curve, the black lines indicate the reconstructed A0 mode.

## 5

### SIMULATED DATA

The extraction of dispersion curves from the simulated data was more straightforward, thanks to the comparatively low level of noise: the curves were found by extracting directly the local maxima in the untreated  $f$ - $k_x$  domain, and were then sorted out according to the last step of the procedure described above. The results of the curve extraction algorithms are shown for both experiment and simulation in Fig. 3.

#### 5.3.2. CURVE FITTING AND ERROR VOLUMES

Once an experimental or simulated curve has been extracted, a fitting procedure can be used to identify the set of  $c_T$ ,  $c_L$  and  $h$  (shear bulk wave speed, longitudinal bulk wave speed and thickness) that generates a theoretical curve that best matches the extracted ones. Typically, such fitting procedures consist in defining an error function that describes the discrepancy between the target and the model, and then applying an optimization algorithm to minimize this error. For instance, a least squares fitting algorithm can be used [12, 17].

In contrast with other studies, the present work does not make use of an optimization algorithm to find the best fitting curve. Instead, a 3D parameter space of  $c_T \in [2000 - 4000]$  m/s,  $c_L \in [4500 - 7500]$  m/s and  $h \in [0.1 - 4.0]$  mm was considered, with speed resolution of 50 m/s and thickness resolution of 0.1 mm. For each point in this space the theoretical curves of A0 and S0 were computed at frequencies comprised between 50 kHz and 3.6 MHz, sampled every 50 kHz. Each curve was then stored in a database. Similarly to other fitting procedures, an error function  $E$  was then introduced, defined here as a Mean Absolute Percentage Error (MAPE),

$$E = \frac{100}{N} \sum_i^N |k_i^{Th} - k_i| / k_i^{Th} \quad (5.1)$$

where  $N$  is the number of frequencies considered, the index  $i$  runs from 1 to  $N$ ,  $k_i$  is the wavenumber corresponding to the  $i$ -th frequency of the measured dispersion curve,

and  $k_i^{Th}$  is the wavenumber of the theoretical curve at the same frequency.

The extracted curves were compared to every theoretical curve in the corresponding database, and the MAPE of each comparison was added to a 3D plot. The resulting image shows the volumetric distribution of the MAPE in the entire parameter space. We will refer to this distribution as “error volume”. Once the error volume has been reconstructed, it is possible to identify the best fitting theoretical curve by finding the coordinates of the global minimum of the MAPE. Moreover, this approach allows one to observe the distribution of the error in the parameter space.

### 5.3.3. FITTING RELIABILITY

To study how noise can affect the correct identification of  $c_T$ ,  $c_L$  and  $h$ , we employed as target curves the theoretical dispersion curves corresponding to the A0 and S0 wave modes, with random noise assigned to the wavenumber coordinate of each point on the curves. At each point, the noise applied was drawn from a uniform distribution of values between -0.5 % and 0.5 % of the wavenumber value of the point. The boundaries of the noise distribution were chosen so that the minimum MAPE would be between 0.2 and 0.4 %, which were the values observed for the global minimum in simulated data of A0 and S0, respectively. Repeating the analysis for ten different realizations of the noise, we observed that the minimum MAPE value could vary by up to approximately 10 % of its average value.

Within the resolution of the database, it is possible to determine whether the minimum is global, as well as how sensitive the error is to the different parameters. For instance, if many points along the  $c_L$  axis correspond to comparably low values of MAPE, similar curves can be generated by different values of longitudinal speed; the optimal value of  $c_L$  may therefore be not reliable.

A traditional sensitivity analysis would be ill suited to describe the reliability of MAPE minimizations, due to its local nature (see Appendix 5.1). Instead, to quantify this concept of reliability based on the error volume analysis, we introduce two parameters: a low error volume (LEV) and a spread around the minimum (SAM). The LEV value indicates the number of theoretical curves whose MAPE is at most 10 % greater than the global minimum; this boundary was chosen based on the 10 % variation in minimum MAPE that was observed to come from random noise. Notably, the points within the LEV form a curved shape within the 3D space, thus the LEV cannot be described as a rectangular volume (i.e. as the product of three orthogonal coordinates). The SAM values indicate how far the points within the LEV are spread along each axis. The SAM values are computed as a weighted mean absolute percentage deviation from the coordinates with minimum MAPE:

$$SAM_X = \frac{100}{i_{min_X}} \sum_i \frac{|i_X - i_{min_X}|}{E_i - E_{min}} \left( \sum_i \frac{1}{E_i - E_{min}} \right)^{-1} \quad (5.2)$$

where  $SAM_X$  is the SAM value along the  $X$  axis (e.g. longitudinal speed),  $\mathbf{i}(X, Y, Z) = (i_X, i_Y, i_Z)$  is a point within the LEV,  $i_X$  is the  $X$  coordinate of the  $\mathbf{i}$  point,  $E_i$  is its corresponding MAPE,  $i_{min_X}$  is the  $X$  coordinate of the point with minimum MAPE,  $E_{min}$  is the minimum value of MAPE, and the sum runs over all the points  $\mathbf{i} \in LEV$ , excluding the global minimum (the point with minimum MAPE). This function was chosen so as to give

more relevance to the points whose MAPE is the most similar to the minimum. The percentage term  $100/i_{min_x}$  was included to allow the comparison of SAM values of different axes.

## 5.4. RESULTS

### 5.4.1. ERROR VOLUMES

#### SIMULATED DATA

Figure 5.4 shows slices of the error volume computed for an A0 curve extracted between 1.5 and 3.1 MHz from simulated data. A global minimum exists within the parameter space considered, and corresponds to a MAPE of 0.218 % at coordinates  $c_L = 4800 \pm 25$  m/s,  $c_T = 3200 \pm 25$  m/s, and  $h = 1.1 \pm 0.05$  mm. The indicated variations are due to the step-sizes of the parameters. The material properties corresponding to the best fitting curve, therefore, are in poor agreement with the actual values  $c_L = 5800$  m/s,  $c_T = 3100$  m/s and  $h = 1$  mm. As can be seen in the plot, however, there is an extended volume in the parameter space in which the MAPE is within 1 %. In fact, the third-lowest error point corresponds to a MAPE of 0.225 % at coordinates:  $c_L = 5850 \pm 25$  m/s,  $c_T = 3100 \pm 25$  m/s, and  $h = 1.0 \pm 0.05$  mm, which are in much better agreement with the input parameters of the simulation.

The same analysis was performed for the S0 mode extracted from the simulated data, see Fig. 5.5. Once again, there is a global minimum error within the parameter space, corresponding to a MAPE of 0.551 % at coordinates  $c_L = 5850 \pm 25$  m/s,  $c_T = 3100 \pm 25$  m/s, and  $h = 1.0 \pm 0.05$  mm. As can be seen in Fig. 5.5, the distribution on the  $c_L$ - $c_T$  plane is similar to that of the A0 mode, while the distribution on the other planes is clearly different. Interestingly, while the coordinates of the global minimum are much closer to the expected values than those of A0, overall the MAPE is higher. This result suggests that, at the frequencies considered, variations in the parameter space of material properties causes greater variations in S0 than in A0 curves. As a consequence, an extracted S0 curve that deviates more from the theoretical one may still yield parameters that are closer to the actual ones, as compared to the A0 case.

Comparing the A0 and S0 error volumes, we can observe that they show a similar trend for the distribution of the low errors along the longitudinal speed axis (almost uniform for  $c_L > 5000$  m/s, indicating a low sensitivity to overestimations of this parameter), whereas the distribution in the  $c_S$ - $h$  plane is different: for the S0 mode, the coordinates of low error points on the  $c_S$  axis increase with increasing thickness, while for the A0 mode the distribution along  $h$  is similar to that along  $c_L$ , indicating low sensitivity to thickness overestimations.

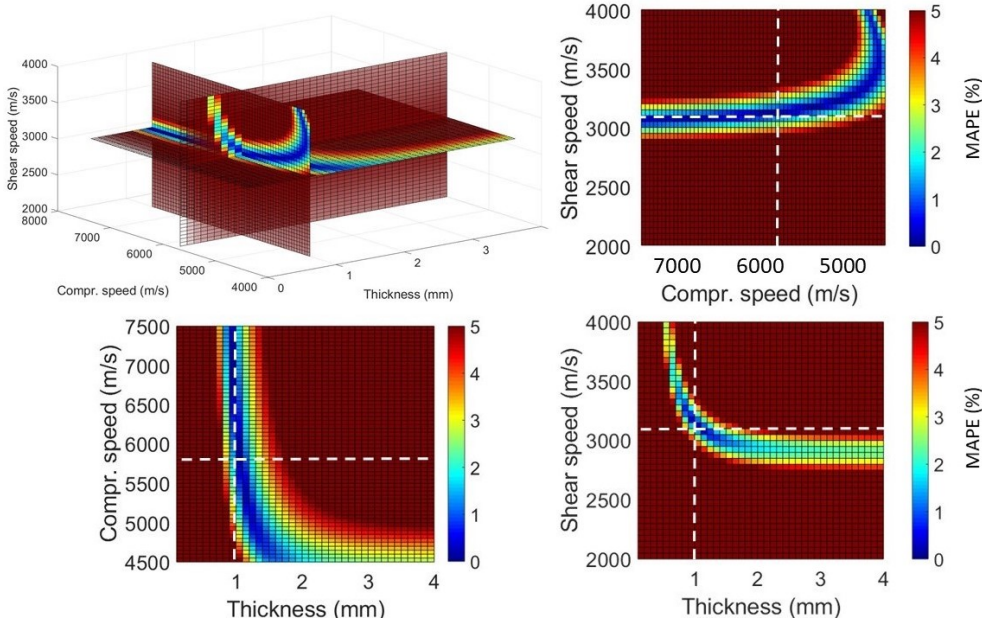


Figure 5.4: The top-left panel shows slices of the error volume for the simulated A0 mode of a stainless steel plate at frequencies between 1.5 and 3.1 MHz . The slices represent planes at the fixed values  $c_L = 5800$  m/s,  $c_T = 3100$  m/s, and  $h = 1$  mm, which are the actual values of these parameters . Each other panel shows the frontal view of a single plane ( $c_L$ - $c_T$ ,  $c_T$ - $h$ ,  $c_L$ - $h$ , in clockwise order). Colors represent the value of MAPE at each coordinate in the parameter space. The white dashed lines show where the planes intersect in each view.

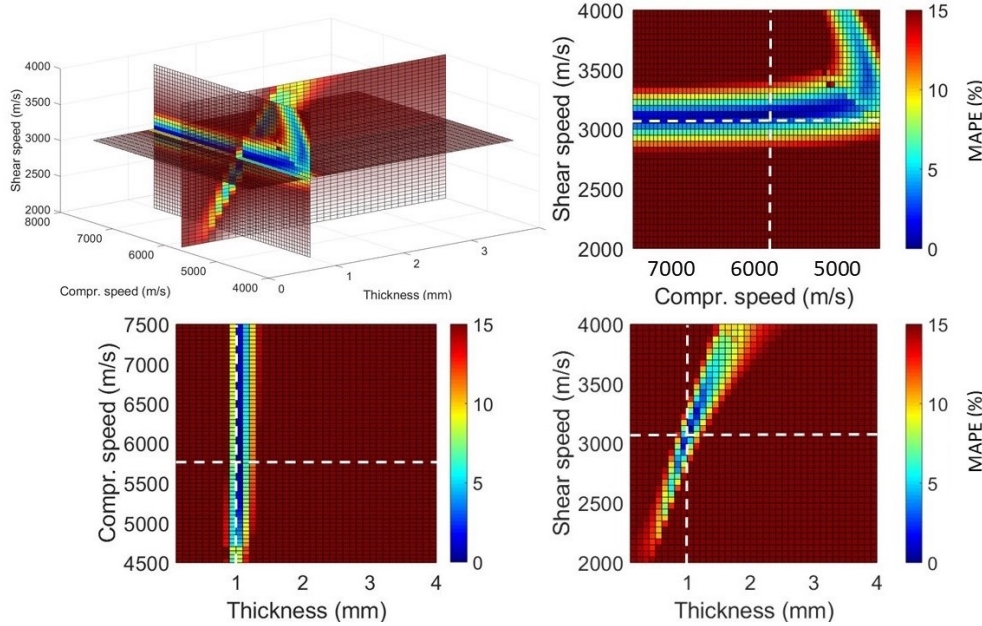


Figure 5.5: The top-left panel shows slices of the error volume for the simulated S0 mode of a stainless steel plate at frequencies between 1.5 and 3.1 MHz . The slices represent planes at the fixed values  $c_L = 5800$  m/s,  $c_T = 3100$  m/s, and  $h = 1$  mm, which are the actual values of these parameters . Each other panel shows the frontal view of a single plane ( $c_L$ - $c_T$ ,  $c_T$ - $h$ ,  $c_L$ - $h$ , in clockwise order). Colors represent the value of MAPE at each coordinate in the parameter space. The white dashed lines show where the planes intersect in each view.

**MEASURED DATA**

Figures 5.6 and 5.7 show the error volumes computed for the A0 and S0 curves extracted from the experiment. Qualitatively speaking, the volumes appear very similar to those of the simulated data. The material properties identified by the minimum of the error volume of A0 are  $c_L = 5500 \pm 25$  m/s,  $c_T = 3100 \pm 25$  m/s, and  $h = 1.0 \pm 0.05$  mm; those extracted from S0 are  $c_L = 5250 \pm 25$  m/s,  $c_T = 3250 \pm 25$  m/s, and  $h = 1.0 \pm 0.05$  mm.

Subsequently, the LEV and SAM values were computed for the two modes for both simulated and experimental data, and are reported in Table 5.1. For each dataset, the S0 mode appears more sensitive than the A0: the LEV and all the SAM values are smaller, confirming that variations in the parameter space of material properties lead to greater variations in S0 than in A0.

<b>Simulated data 1 mm thick stainless steel plate</b>				
	<b>LEV</b>	<b>SAM<sub>c<sub>L</sub></sub></b>	<b>SAM<sub>c<sub>T</sub></sub></b>	<b>SAM<sub>h</sub></b>
<b>A0</b>	50	20.8 %	3.2 %	10.0 %
<b>S0</b>	14	0.8 %	0.0 %	0.0 %
<b>Experimental data 1 mm thick stainless steel pipe</b>				
	<b>LEV</b>	<b>SAM<sub>c<sub>L</sub></sub></b>	<b>SAM<sub>c<sub>T</sub></sub></b>	<b>SAM<sub>h</sub></b>
<b>A0</b>	209	13.0 %	2.1 %	7.0 %
<b>S0</b>	7	3.8 %	0.4 %	0.0 %

Table 5.1: Values of LEV and SAM for the A0 and S0 modes extracted from a simulated 1 mm thick stainless steel plate (above) and from an experiment on a 1 mm thick stainless steel pipe (below) at frequencies between 1.5 MHz and 3.1 MHz.

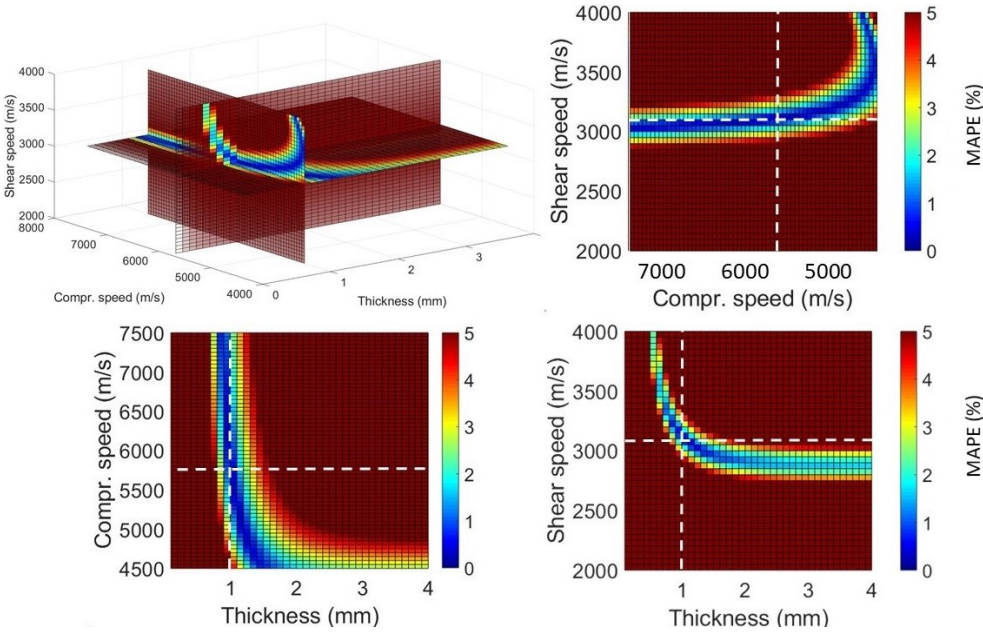


Figure 5.6: The top-left panel shows slices of the error volume for the A0 mode extracted from an experiment on a 1 mm thick stainless steel pipe at frequencies between 1.5 and 3.1 MHz . The slices represent planes at the fixed values  $c_L = 5800$  m/s,  $c_T = 3100$  m/s, and  $h = 1$  mm, which are the actual values of these parameters . Each other panel shows the frontal view of a single plane ( $c_L$ - $c_T$ ,  $c_T$ - $h$ ,  $c_L$ - $h$ , in clockwise order). Colors represent the value of MAPE at each coordinate in the parameter space. The white dashed lines show where the planes intersect in each view.

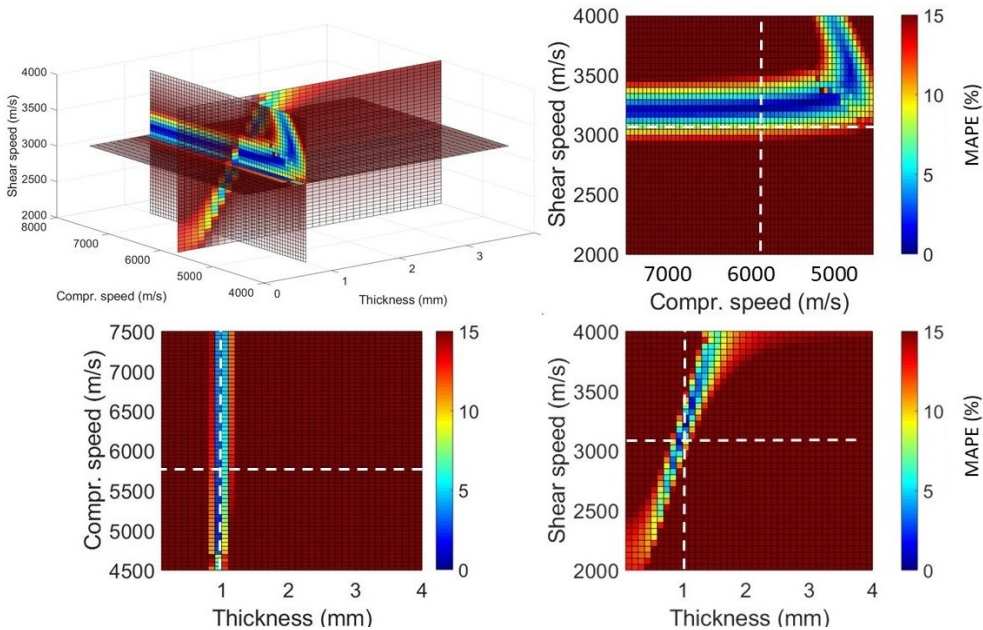


Figure 5.7: The top-left panel shows slices of the error volume for the S0 mode extracted from an experiment on a 1 mm thick stainless steel pipe at frequencies between 1.5 and 3.1 MHz . The slices represent planes at the fixed values  $c_L = 5800$  m/s,  $c_T = 3100$  m/s, and  $h = 1$  mm, which are the actual values of these parameters . Each other panel shows the frontal view of a single plane ( $c_L$ - $c_T$ ,  $c_T$ - $h$ ,  $c_L$ - $h$ , in clockwise order). Colors represent the value of MAPE at each coordinate in the parameter space. The white dashed lines show where the planes intersect in each view.

### 5.4.2. ROBUSTNESS AGAINST NOISE

The theoretical curves of A0 and S0 were calculated between 50 kHz and 3.5 MHz for a 1 mm thick stainless steel plate. As described in section 5.2.3, random noise was added to the wavenumber coordinates of both curves. For each curve, the error volume was reconstructed and used to identify the best fitting curve, i.e. the curve with minimum error. This procedure was repeated ten times for each mode. Table 5.2 shows the average and highest minimum MAPE, and the mean absolute error (MAE) and maximum error of  $c_T$ ,  $c_L$  and  $h$ , compared to their true values ( $c_L = 5800$  m/s,  $c_T = 3100$  m/s, and  $h = 1.0$  mm), for each mode.

	$\bar{E}$ (%)	$E_{min}$ (%)	MAE $c_L$ (m/s)	$\Delta c_{L,max}$ (m/s)	MAE $c_T$ (m/s)	$\Delta c_{T,max}$ (m/s)	MAE $h$ (mm)	$\Delta h_m$ (mm)
<b>A0</b>	0.25	0.27	95	1000	10	100	0.01	0.1
<b>S0</b>	0.24	0.26	5	50	0	0	0.00	0.0

Table 5.2: Results of generating ten A0 and ten S0 curves affected by uniformly distributed random noise applied to the wavenumber coordinates. Entries in the table show, from left to right: the average minimum MAPE ( $\bar{E}$ ), the highest value of minimum MAPE ( $E_{min}$ ), the mean and maximum absolute error of  $c_L$  compared to the true value (MAE  $c_L$  and  $\Delta c_{L,max}$ ), the mean and maximum absolute error of  $c_T$  compared to the true value (MAE  $c_T$  and  $\Delta c_{T,max}$ ), and the mean and maximum absolute error of  $h$  compared to the true value (MAE  $h$  and  $\Delta h_{max}$ )

### 5.4.3. FREQUENCY RANGE ANALYSIS

During data analysis, we observed that theoretical curves generated for different values of one parameter could be more similar to each other at certain frequencies than at others. For example, the MAPE between two S0 curves corresponding to thicknesses of 1 mm and 1.2 mm, for shear and compressional speeds fixed at 3100 and 5800 m/s respectively, was less than 1 % at frequencies between 0 and 1 MHz and around 18% between 1.5 and 2.5 MHz.

To investigate how different frequency regions affected the LEV and SAM results, comparison of noiseless theoretical A0 and S0 curves to the database was performed at various frequency ranges. The frequency ranges considered included bands with a width of 0.2 to 2.9 MHz, within an overall range of 0.1 - 3.1 MHz. For each frequency range, the LEV and SAM values were computed and plotted. For this calculation only, the LEV was defined as all the curves whose MAPE was within 110 % of the second-lowest error, instead of the lowest error. This choice was made because the lowest error was always zero, since theoretical curves were considered and the database contained the theoretical curves themselves.

Figures 5.8 and 5.9 show the values of LEV and SAM at different frequency ranges for the noiseless theoretical A0 and S0 curves, respectively, of a 1 mm thick stainless steel plate. The vertical axis represents the starting frequency for each of the ranges considered, while the horizontal axis represents the bandwidth of each range. Since only frequencies between 0.1 and 3.1 MHz were considered in this analysis, the maximum bandwidth of the frequency ranges decreases with the increase of the starting frequency. Each point in the plots shown in figures 5.8 and 5.9 thus corresponds to an analysis performed at a different frequency range, determined as the combination of a starting frequency and a bandwidth.

For A0, considering only higher frequencies introduces a greater variability of longitudinal speeds within the LEV, while the highest precision seems to be achievable for all three parameters within the first MHz; the value of SAM of the shear speed appears to be relatively low (within 50 m/s) at most frequencies. The LEV itself can vary considerably depending on the frequency band considered. In contrast, the SAM values for the S0 mode are almost uniformly low at the higher frequencies, while there is a region of frequencies around 0.5 MHz in which they increase, especially for the thickness.

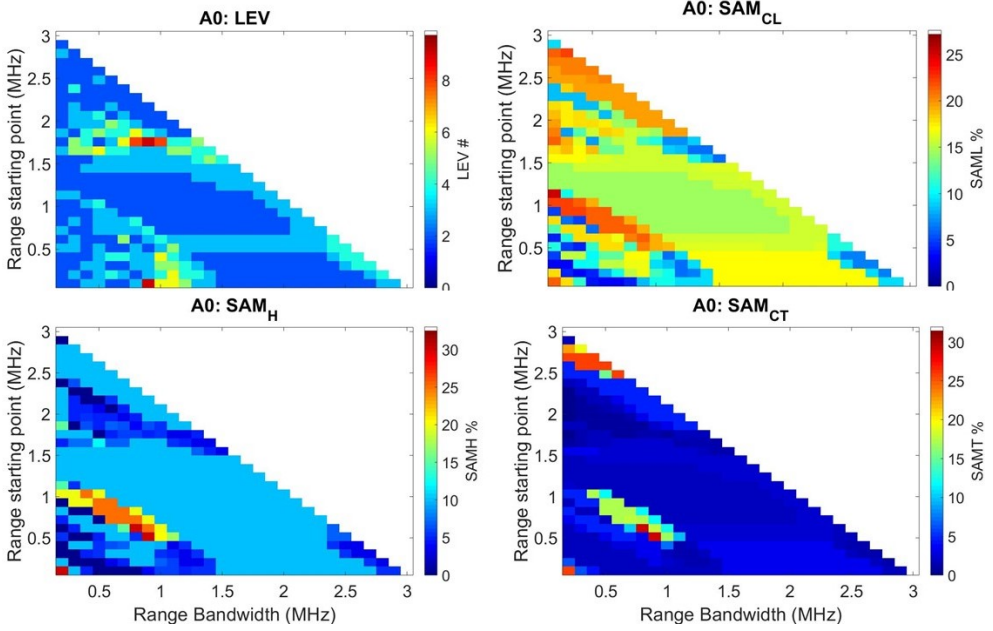


Figure 5.8: LEV,  $SAM_{CL}$ ,  $SAM_{CT}$ , and  $SAM_h$  for a theoretical A0 curve at different frequency ranges. The colors represent the amplitude of each variable, with each point corresponding to a different combination of bandwidth and starting frequency.

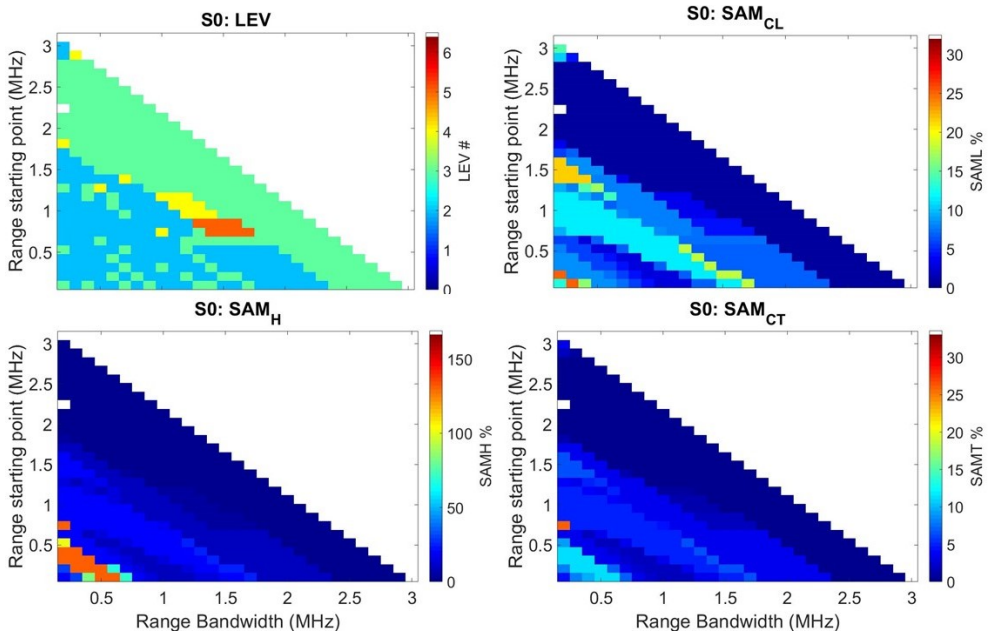


Figure 5.9: LEV,  $SAM_{CL}$ ,  $SAM_{CT}$ , and  $SAM_h$  for a theoretical S0 curve at different frequency ranges. The colors represent the amplitude of each variable, with each point corresponding to a different combination of bandwidth and starting frequency.

## 5.5. DISCUSSION

Several studies can be found in literature detailing techniques to extract Lamb dispersion curves and inversion methods to reconstruct material properties [11–22]. However, these studies rely on minimization techniques that only yield information about the (possibly) global minimum of a given error function. When employing such an approach, therefore, all information about how the error is distributed over the parameter space is lost. One of the advantages of the comparison approach presented in this chapter is that information about the matching error of the dispersion curves (the MAPE defined in Eq. 5.1) is extracted along with the coordinates of the global minimum, at the cost of having to initially compute and store dispersion curves for the entire parameter space. This additional information is necessary to assess how reliable the results of the inversion are, both in a general sense (i.e. how precise can we expect a multi- or single-parameter inversion to be) and for a specific measurement (e.g. how reliable a measurement is performed with a given setup under specific experimental conditions and corresponding experimental noise). Moreover, our results identify which zeroth order wave mode is the most sensitive to what material property at what frequencies, and the approach we have presented here could also be employed to extend these results to higher order modes and higher frequencies, providing a toolset to maximise the precision of the results of inversion.

To better understand how information on the MAPE is connected to the precision of the inversion, let us consider the following: if, along a given axis (e.g. longitudinal wave speed), there are multiple coordinates at which the MAPE is comparable to the global minimum, then many curves corresponding to different material properties are comparably similar to the target one (e.g. the one extracted from experiments). Small variations in the target curve, for instance due to experimental noise or poor reconstruction of the wave mode, could then greatly shift the location of the global minimum and therefore the values of the reconstructed properties. Knowing the distribution of the MAPE, then, allows one to know how much the material properties can vary with small variations of this error. Intuitively, the larger the range of parameters with a low error, the less reliable are the properties corresponding to the global minimum.

To provide a quantitative measure of the sensitivity described above, we have introduced the values of Low Error Volume (LEV) and Spread Around Minimum (SAM). The LEV value represents how many different curves have a MAPE comparable to the minimum one. Here, ‘comparable’ is defined as a threshold of up to 10 % higher than the minimum MAPE. By itself, however, the LEV is not sufficient to tell whether a result is reliable: if there were 100 curves represented within the LEV, but all located at similar coordinates, even if the global minimum was shifted to another point (e.g. due to noise), the result would not be affected greatly. The SAM values represent how the error spreads along each parameter axis: a lower spread along one axis means a higher precision with respect to the corresponding parameter. This is different from a standard sensitivity analysis, in that the SAM values consider all the points within the LEV to determine how much a coordinate could vary, whereas the sensitivity analysis only looks at the derivatives in the neighbourhood of the minimum, fixing two coordinates out of three at a time. A more detailed explanation of why this local information is not sufficient is given in the Appendix.

Practical observations guided the choices made for the LEV and SAM thresholds: the LEV boundary (110 % of the minimal MAPE) was established based on the observed vari-

ability in minimal MAPE when the target curve was a theoretical curve with uniformly distributed random noise on the wavenumber coordinates; the SAM values were computed as an average weighted by the inverse of the MAPE, to reflect that lower error curves are more likely to be mixed up with the curve of the global minimum. As long as LEV and SAM are defined consistently, they allow to compare different curves of the same wave mode, different wave modes and frequency ranges, and even different experiments.

By employing the LEV and SAM parameters, it was also possible to analyse how the sensitivity of the A0 and S0 modes varies with the frequency range over which the curves are compared. In particular, figures 5.8 and 5.9 show that the A0 mode can be more reliable than S0 in estimating the longitudinal wave speed and the thickness when only low frequencies are available, i.e. up 1 MHz for a 1 mm plate. At higher frequencies, the S0 mode appears to provide more precise information about all three parameters. Notably, in our study we have only focussed on zeroth order modes, and these two modes were only analysed separately. As mentioned above, however, our approach can be used also to analyse higher order modes. It would be interesting to investigate, then, if combining multiple modes at their “best” frequency ranges, e.g. by combining their error volumes by sum or multiplication, could improve precision or accuracy.

Low values of LEV and SAM, however, don't guarantee that the minimum error curve corresponds to the true values of the properties of the medium; they should be interpreted as a measure of precision, rather than accuracy. In fact, when comparing the A0 and S0 modes in the experimental data, the SAM and LEV values are lower for S0, but the parameters identified by the minimum of the error volume of A0 are more accurate compared to the expected nominal properties of the pipe. This result means that, in this one measurement, the curves extracted from the experiment yield a more accurate result for A0 than for S0; however, given the higher values of SAM and LEV, it is reasonable to expect that repeated experiments would show a greater variation in results for A0 than for S0. It is also worth mentioning here that the central assumption of this paper, i.e. that we can use the Lamb characteristic equations to describe our measurements, is verified only in an approximate sense: the equations, in fact, are defined for infinite plates with perfectly parallel, smooth surfaces and elastic, homogeneous and isotropic materials, while a real metal plate necessarily presents surface roughness and imperfections, warping, and anisotropic behaviours due to sheet fabrication process. For finite element simulation, moreover, the applied discretization scheme (size and shape of the elements, interpolation between nodes) can alter the accuracy with which results are calculated. All of these factors are likely to cause deviations from the theoretical curves, and it is reasonable to expect that different modes will be affected differently, due to their different particle motion patterns and wave velocities.

Besides providing information on the distribution of the matching error, the approach we employ in this study has several other advantages over traditional optimization algorithms. For one, its results don't depend on initial guesses. Moreover, most of the computational cost lies in the generation of the database of theoretical curves that is used for the comparisons with the target curve; once the database exists, it can be used any number of times on any number of different experimental or simulated curves. In contrast, every time an optimization algorithm runs, it has to re-compute each theoretical curve it uses. While the number of curves thus computed is usually lower than that necessary to create

a database, the cost for the database is paid only once, whereas that of the optimization is paid every time it is employed. In terms of real-world applications, this approach could benefit greatly the efficiency of in-situ non-destructive tests, such as pipe inspections, where the database could be computed during the fabrication of the testing instrument, ready to be used at every subsequent test.

A drawback of the database approach, however, is that it only provides results within its parameter space, which is defined at the moment of the creation of the database. Moreover, there is a trade-off between accuracy (limited by the resolution of the database), range of parameters explored (defined by the boundaries of the database) and size of the database itself (for reference, the database used in the present work has a size of 55 Mb). This problem can be circumvented by preparing various application-specific databases, in which resolution and boundaries of a database are tailored to the use it has to serve, e.g. analysing a steel pipe with nominal thickness of 1 mm.

Finally, the results presented in Table 2 highlight a potential general weakness in the approach of inverting dispersion curves to reconstruct material properties. In fact, while the S0 curve showed less sensitivity to the random noise, one out of ten noise-affected A0 curves yielded a longitudinal speed 1000 m/s lower than the true value. Repeating the same analysis with noise randomly distributed across a wider range (between -1 % and 1 % of each wavenumber coordinate), comparable to the average variations observed in the experiment, yielded three cases out of ten in which the longitudinal speed extracted from the A0 curve was between 800 and 1000 m/s lower than the true value. These results would suggest that the properties found by inverting the A0 curve can be considerably affected by noise, undermining their reliability in practical applications. Moreover, here all three parameters (transverse and longitudinal wave speeds, and thickness) were extracted simultaneously, but it would also be reasonable to investigate whether prior knowledge on some of the parameters would improve the results. Indeed, for a noise-affected theoretical A0 curve in which three-parameters estimation yielded  $c_L = 4800$  m/s, we observed that fixing the thickness at 1.0 mm corresponded to a minimum error curve generated by  $c_L = 5500$  m/s; fixing both the thickness at 1.0 mm and the shear speed at 3100 m/s yielded an estimated  $c_L = 5850$  m/s, suggesting that a priori knowledge of some parameters can increase the robustness of results against noise.

In principle, using our results, it could even be possible to extract a single property using the most precise combination of mode and frequency range, then use that property as input fixed value and extract the second property, again based on its corresponding best mode and frequency range, and iterate until all properties are extracted. This bootstrapping approach could be very useful in applications where a priori knowledge is not available; however, it remains to be proven whether it would have the same effect, which likely depends on the accuracy with which the first property is extracted. In any case, it would be interesting to perform a more extensive analysis, both on noise-affected theoretical curves as well as on repeated experiments, to determine what percentage of cases leads to significant over- or underestimations of material properties.

## 5.6. CONCLUSIONS

In this work we have presented a new approach for the extraction of parameter values from Lamb wave dispersion curves. This approach yields simultaneously three parameters of

the wave guide (thickness, longitudinal speed and shear speed), as well as quantitative information on the precision with which the information is extracted. We have observed that low amplitude random noise can affect the results of Lamb wave dispersion curve inversion, with few A0 curves yielding longitudinal speeds far off their true value, thus highlighting the importance of having such a measure of precision. Moreover, using the proposed method, we have shown that the S0 mode is more sensitive than the A0 mode to all three properties at higher frequencies, and that both modes are more sensitive to shear speed and thickness than to compressional speed. These results could therefore be employed to increase the precision with which the material properties are reconstructed, by identifying the optimal combination of wave mode and frequency range for each.

## 5.7. APPENDIX: SENSITIVITY ANALYSIS

In the main text, we often refer to the reliability of extracting parameters by comparing dispersion curves of Lamb modes, or the sensitivity of such a procedure to each parameter. A well-known approach to quantify this information is to perform a so-called sensitivity analysis. In our case, this could be done by considering the error function  $E$  (corresponding to the MAPE values) and computing its first derivatives around the minimum. For example, the sensitivity of  $E$  with respect to variations on the compressional speed axis can be calculated as:

$$S(c_L, P) = (\partial E / \partial c_L)|_P \quad (5.3)$$

where  $S$  is the sensitivity,  $c_L$  is the compressional speed, and  $|_P$  indicates that the derivative is evaluated at the coordinates  $(c_L^P, c_T^P, h^P)$  of the point  $P$ , which corresponds to the minimum MAPE value. This value of  $S$  expresses how fast the function  $E$  grows for small variations of the  $c_L$  coordinate. However, it does not provide any information on the existence and location of the local minima of comparable depth that can exist within the MAPE space. As such, the sensitivity analysis does not show that a small variation in MAPE could lead to large variations in e.g.  $c_L$ . The SAM and LEV values were introduced to provide this necessary information.

In Figure 5.10, the left panel is the same as in Fig. 5.6, while the right panel shows all the points within the LEV, projected onto the  $h$ - $c_L$  plane. The points highlighted as  $P_1$  and  $P_2$  in the right panel correspond to the minimum and second-minimum MAPE points, respectively. The coordinates of  $P_1$  are:  $c_L = 5500$  m/s;  $c_T = 3100$  m/s;  $h = 1.0$  mm; The coordinates of  $P_2$  are:  $c_L = 4850$  m/s;  $c_T = 3150$  m/s;  $h = 1.1$  mm. The MAPE of  $P_1$  is 0.439 %, the MAPE of  $P_2$  is 0.441 %. These numbers show that the two curves corresponding to  $P_1$  and  $P_2$  are very similar to each other; the smallest alteration of  $P_1$  could turn it into  $P_2$ , resulting in an extracted compressional speed of 4850 m/s instead of 5500 m/s.

The sensitivity analysis of  $E$  in the  $c_L$  direction around  $P_1$ ,  $S(c_L, P_1) = 0.5$  ms/m (i.e. the MAPE grows by approximately 6 % in a step of 50 m/s on the  $c_L$  axis) is limited to a local description along a single axis, and it does not provide any information to describe the situation shown in Fig. 5.10. The SAM  $c_L$  value of 604 m/s, on the other hand, accounts for the entire LEV (across all three axes), and it does show that small variations of the MAPE could potentially lead to large variations in compressional speed. As such, in this situation the LEV and SAM values are necessary to provide the quantitative description that a standard sensitivity analysis cannot supply.

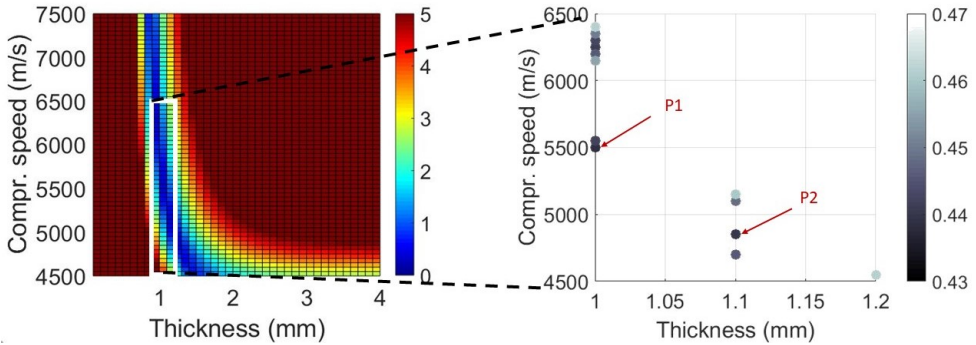


Figure 5.10: Left panel: the  $h$ - $c_L$  slice of Fig. 5.6. Right panel: the LEV of this dataset, collapsed onto the  $h$ - $c_L$  plane. Highlighted are  $P_1$  and  $P_2$ , the points corresponding to the lowest and second-lowest values of MAPE, respectively. The colors in both panels represent the MAPE.

## 5

## REFERENCES

- [1] K. Heller, L. J. Jacobs, and J. Qu, *Characterization of adhesive bond properties using Lamb waves*, NDT & E International **33**, 555 (2000).
- [2] K. I. Lee and S. W. Yoon, *Feasibility of bone assessment with leaky Lamb waves in bone phantoms and a bovine tibia*, The Journal of the Acoustical Society of America **115**, 3210 (2004).
- [3] G. Rizzuti and A. Gisolf, *2-D wavefield inversion for high-resolution elastic property estimation*, in *76th European Association of Geoscientists and Engineers Conference and Exhibition 2014: Experience the Energy - Incorporating SPE EUROPEC 2014* (2014) pp. 4606–4610.
- [4] P. Song, X. Bi, D. C. Mellema, A. Manduca, M. W. Urban, J. F. Greenleaf, and S. Chen, *Quantitative Assessment of Left Ventricular Diastolic Stiffness Using Cardiac Shear Wave Elastography*, Journal of Ultrasound in Medicine **35**, 1419 (2016).
- [5] M. Fakh, S. Mustapha, J. Tarraf, G. Ayoub, and R. Hamade, *Detection and assessment of flaws in friction stir welded metallic plates*, in *Proceedings of SPIE - The International Society for Optical Engineering*, Vol. 10168 (2017).
- [6] S. Otsuka, X. Shan, K. Yoshida, T. Yakura, M. Naito, and Y. Kawakami, *Site dependent elastic property of human iliotibial band and the effect of hip and knee joint angle configuration*, Journal of Biomechanics **109** (2020), 10.1016/j.jbiomech.2020.109919.
- [7] H. Lamb, *On Waves in an Elastic Plate*, Proceedings of the Royal Society A: Mathematical, Physical and Engineering Sciences **93**, 114 (1917).
- [8] J. Rose, *Ultrasonic Guided Waves in Solid Media*, Vol. 9781107048 (2014) pp. 1–512.
- [9] E. Maksuti, F. Bini, S. Fiorentini, G. Blasi, M. W. Urban, F. Marinozzi, and M. Larson, *Influence of wall thickness and diameter on arterial shear wave elastography: a phantom and finite element study*, Physics in Medicine and Biology **62**, 2694 (2017).

- [10] A. Caenen, M. Pernot, D. A. Shcherbakova, L. Mertens, M. Kersemans, P. Segers, and A. Swillens, *Investigating Shear Wave Physics in a Generic Pediatric Left Ventricular Model via In Vitro Experiments and Finite Element Simulations*, IEEE Transactions on Ultrasonics, Ferroelectrics, and Frequency Control **64**, 349 (2017).
- [11] I. Z. Nenadic, M. W. Urban, S. A. Mitchell, and J. F. Greenleaf, *Lamb wave dispersion ultrasound vibrometry (LDUV) method for quantifying mechanical properties of viscoelastic solids*, Physics in Medicine and Biology **56**, 2245 (2011).
- [12] M. Bernal, I. Nenadic, M. W. Urban, and J. F. Greenleaf, *Material property estimation for tubes and arteries using ultrasound radiation force and analysis of propagating modes*, The Journal of the Acoustical Society of America **129**, 1344 (2011).
- [13] T. Tran, M. Sacchi, D. Ta, V.-H. Nguyen, E. Lou, and L. Le, *Nonlinear Inversion of Ultrasonic Dispersion Curves for Cortical Bone Thickness and Elastic Velocities*, Annals of Biomedical Engineering **47**, 2178 (2019).
- [14] C. Grünsteidl, T. Berer, M. Hettich, and I. Veres, *Using zero-group-velocity lamb waves to determine thickness and bulk sound velocities of isotropic plates*, in *AIP Conference Proceedings*, Vol. 2102 (2019) p. 050016.
- [15] L. Zhu, X. Duan, and Z. Yu, *On the Identification of Elastic Moduli of In-Service Rail by Ultrasonic Guided Waves*, Sensors **20**, 1769 (2020).
- [16] Y.-C. Lee and S.-W. Cheng, *Measuring Lamb wave dispersion curves of a bi-layered plate and its application on material characterization of coating*, IEEE Transactions on Ultrasonics, Ferroelectrics, and Frequency Control **48**, 830 (2001).
- [17] J. L. Deán, C. Trillo, Á. F. Doval, and J. L. Fernández, *Determination of thickness and elastic constants of aluminum plates from full-field wavelength measurements of single-mode narrowband Lamb waves*, The Journal of the Acoustical Society of America **124**, 1477 (2008).
- [18] M. Sale, P. Rizzo, and A. Marzani, *Semi-analytical formulation for the guided waves-based reconstruction of elastic moduli*, Mechanical Systems and Signal Processing **25**, 2241 (2011).
- [19] J. Foiret, J.-G. Minonzio, C. Chappard, M. Talmant, and P. Laugier, *Combined estimation of thickness and velocities using ultrasound guided waves: A pioneering study on in vitro cortical bone samples*, IEEE Transactions on Ultrasonics, Ferroelectrics, and Frequency Control **61**, 1478 (2014).
- [20] M. Ponschab, D. A. Kiefer, and S. J. Rupitsch, *Simulation-Based Characterization of Mechanical Parameters and Thickness of Homogeneous Plates Using Guided Waves*, IEEE Transactions on Ultrasonics, Ferroelectrics, and Frequency Control **66**, 1898 (2019).
- [21] C. Chang and F. Yuan, *Dispersion curve extraction of Lamb waves in metallic plates by matrix pencil method*, in *Proceedings of SPIE - The International Society for Optical Engineering*, Vol. 10168 (2017).

- [22] P. Zabbal, G. Ribay, B. Chapuis, and J. Jumel, *Multichannel Multiple Signal Classification for dispersion curves extraction of ultrasonic guided waves*, Journal of the Acoustical Society of America **143**, EL87 (2018).

# 6

## CONCLUSIONS AND DISCUSSION

## 6.1. CONCLUSIONS

Based on the results of the research presented in this thesis, the following conclusions can be drawn:

- **The frequency of a propagating wave carries information about the heart cycle.** As the heart contracts or relaxes, its stiffness varies over time. This variation leads to shifts in the amplitude and the frequency of the wave, which can be distinguished from the effects of spatial inhomogeneities (since these would alter the wavelength, rather than the frequency).
- **The thickness variations of the interventricular septum can have a significant impact on wave propagation.** The plate-like shape of the septum leads to Lamb dispersion effects, which severely undermine the reliability of converting time-of-flight speeds into stiffness. Moreover, Lamb wave analysis assumes constant values of plate thickness, which is not the case in the septum; as a consequence, the dispersion curve of a mode (e.g. A0) can be distorted by the thickness variations in the region where the M-line is placed. In this thesis, we have shown that the shear modulus can be reconstructed more accurately if the average thickness of the plate is considered when fitting theoretical curves to the measured one.
- **The Local Phase Velocity Imaging (LPVI) approach and frequency-wavenumber domain analyses of short M-lines provide comparable estimates of shear modulus in cardiac-mimicking plates.** Both methods can reconstruct Lamb dispersion curves by analysing data contained within a short horizontal space (4 mm, in a 40 mm long plate), and both can yield an estimate of shear modulus deviating less than 20 % from the true value. In our implementation, the computational time of the short M-line analysis was approximately five times shorter than that of the LPVI approach. Surprisingly, restricting the analysis of tapered plates to local information did not yield more accurate results than assuming an average thickness over longer M-lines. As such, among the methods considered in this work, using the longest M-line available remains the best approach to analyse homogeneous cardiac-mimicking plates, even in the presence of thickness variations.
- **Inverting zero-order Lamb modes can simultaneously yield the thickness and the shear and compressional speeds, but the process can have low precision and is susceptible to noise.** In fact, during the analysis of the results from Chapters 3 and 4, we observed that small variations of the input parameters (e.g. a slightly different frequency range) could yield significantly different results of global optimizations; these observations were further confirmed with experiments and simulations of Lamb propagation in steel plates and pipes. The error maps showed that numerous similar curves are spread over the parameter space  $c_p - c_s - h$  (compressional speed, shear speed and thickness, respectively). By performing controlled numerical tests, we demonstrated that even using a theoretical curve as target can result in large errors, in the presence of low-amplitude random noise. To provide a quantitative description of the error distribution, we have introduced new parameters, the SAM and LEV values.

## 6.2. RESULTS IN CONTEXT

The propagation of shear waves in the heart has been extensively investigated over the past decades. Many studies have focused on developing and refining different approaches to acquire and analyse [1–7] wave propagation images. A lot of progress has been made, and there are already reports of shear waves being detected and analysed *in-vivo* [8–11], correlating the results with pathologies such as cardiac hypertrophy and amyloidosis [11, 12].

Fewer studies have focused on investigating the interplay between physical properties of the heart and wave propagation, analysing e.g. the impact of muscle fiber orientation [13–16], viscosity [3, 17–19] and curvature of the muscle [18]. These results are of great importance to the interpretation of shear wave measurements, as they provide the link between the raw number (e.g. wave speed) and the physical state of the muscle (e.g. its stiffness). At the start of this thesis, however, several fundamental aspects of the heart still remained to be investigated in relation to wave propagation.

For example, Chapter 2 deals with the effects of temporal variations of stiffness on wave propagation, such as take place during the natural contraction-relaxation cycle of the heartbeat. This topic has been under investigation for over half a century in the context of electromagnetic waves [20–27] but had never been considered before in the field of medical imaging. On the other hand, many studies of cardiac elastography do measure wave propagation during transitional phases of the heart cycle, where the muscle is either contracting or relaxing [1, 10, 11, 28, 29]. The effects that we observed in our model, considering realistic relaxation values, are small compared to the resolution of current technologies, and as such it could be tempting to ignore them. However, if identified and resolved correctly, they could offer direct insight on the relaxation or contraction of the muscle, and consequently on its functioning.

Another important aspect of the heart is the relatively small thickness of the muscle, which, in first approximation, can be modeled as a plate, where the physical behaviour of waves is radically different from propagation in bulk media [30, 31]. Interestingly, despite several studies having shown that time-of-flight measurements of propagation speed cannot be directly converted to accurate values of the stiffness of plate-like media [18, 32], many contemporary studies still report these speeds as a direct measure of stiffness [11, 12, 29]. In this context, the results of Chapter 3 reinforce the evidence discouraging time-of-flights measurements for direct stiffness quantification, providing a quantitative estimation of the error that can be incurred even in a controlled setup (i.e. in simulations). Moreover, it extends the understanding of the relation between muscle shape and shear wave elastography by showing the effects for thickness variations, which had been previously shown to affect the dispersion curves of waves propagating in metal plates [33, 34].

The research presented in Chapter 4 is a direct consequence of the results of Chapter 3: since local variations of the cardiac thickness can impact the dispersion modes of propagating waves, a method to analyse these modes locally is necessary. Several methods had already been proposed in literature. For example, it was shown that diffuse reverberant fields can be analysed to reconstruct local wavenumbers [6, 35]; the applicability of analysing diffuse fields for cardiac elastography, however, remains to be proven. Other studies analysed local shear wave patterns with model-based estimators [36, 37], while

others still focused on the phase and amplitude decay of a shear wave at increasing distances from the wave source [38]; these works aimed at reconstructing viscoelastic properties in bulk media, thus neglecting Lamb-like dispersion. More recently, the LPVI method was proposed for the local analysis of viscosity-induced dispersion [7, 39, 40], based on a method used in non-destructive testing with guided waves [41]. This approach was proven to yield accurate results from data coming from a 2D window as small as 3x3 mm, and it was proven to perform better than other local elastography methods [7]. As such, it was considered to be a good candidate for the analysis of dispersive waves in heart-like plates. Our results show that, indeed, the LPVI can be successfully employed to reconstruct Lamb dispersion curves and, therefore, calculate local values of shear modulus within an accuracy of 30% from its true value. Moreover, in Chapter 4 we also present a significant comparison that was lacking in previous literature, that is a comparison with the results that can be found by performing the analysis of data extracted along a single M-line in the frequency-wavenumber domain, which is commonly done for non-local measurements [3, 18, 19]. The M-line approach was proven to yield, on average, equally accurate information on a local scale as the one provided by the LPVI approach, at a smaller computational cost. However, even in the presence of thickness variations, the values of shear modulus extracted locally were less accurate than those extracted using the approach of Chapter 3; from these results, it appeared that local dispersion measurements did not provide any advantage over global ones in homogeneous tapered plates.

## 6

In Chapters 3 and 4, the analysis of Lamb waves is limited to the antisymmetric modes, as is commonly done in SWE research [3, 18, 19, 42, 43]. The reason is that most of these studies, including the research presented in this thesis, consider as the wave source a transversal line source (e.g. induced by ARF) and record the transversal displacement from a parasternal point of view (i.e. with the axial direction of the transducer oriented transversally to the long side of the septal wall); these conditions result in the antisymmetric modes being primarily generated and detected. Keijzer *et al.* hypothesised that symmetric Lamb modes could also be generated by valve closure, and that they would be detectable when imaging the heart from an apical point of view (i.e. with the axial direction of the transducer oriented in parallel to the long side of the septal wall) [44]. However, they concluded that their results did not support this hypothesis. For this reason, symmetric modes were not considered in the present research.

Finally, the approach we propose in Chapters 3 and 4 to calculate the shear modulus shares many similarities with most the studies that focus on reconstructing material properties based on the propagation of Lamb waves: that is, given an experimentally extracted dispersion curve, parameters such as stiffness and thickness can be identified by fitting the curve with a theoretical one [3, 18, 45, 46]. In fact, recent studies have shown the possibility of reconstructing several parameters at once [47–49]. Two fundamental assumptions at the core of all these methods, including the one presented in this thesis, is that a single set of parameters corresponds to a unique dispersion curve, and that similar curves correspond to similar parameters. However, we could not find in literature a proof of the validity of this assumption. Chapter 5 was then dedicated to exploring this aspect of Lamb wave analysis, to determine the limitations of (multi-)parameter Lamb wave inversion approaches.

### 6.3. IMPLICATIONS FOR APPLICATIONS

The work shown in these pages may seem far removed from real-world clinical applications; after all, all the results come from either very simplified experiments or abstract numerical simulations. However, the improvement of our theoretical understanding of the behaviour of waves in the heart has a direct impact on how a real-world measurement is acquired and interpreted.

Let us make an example: A and B are two patients; a clinician performs an ultrasound SWE measurement in both, and observes clearly comparable time-of-flight speeds. This would be a very good and relevant achievement. Without further theoretical knowledge, it would also be where the clinician stops, concluding that the stiffness values are also similar and within normal parameters. However, using the knowledge presented in Chapter 3, the clinician knows that it is important to also account for the thickness of the heart where the measurements were taken: if, for example, it turned out that the heart of patient B was measured in a thinner area at the same frequencies, the same time-of-flight speed would have to correspond to a higher value of stiffness, perhaps indicating the onset of a pathology.

The one above is, of course, an *ad-hoc* example that greatly simplifies a complex situation to prove a point. It does help, however, in visualising how a practical, clinical activity could be informed by theoretical results such as those presented in this thesis.

In this optic, Chapter 2 suggests that, when technological developments will allow for a greater resolution in the frequency domain, it may be possible to perform functional imaging of diastolic relaxation based on frequency shifts. Chapter 4 shows the viability of a new method to analyse wave motion when the window in which it is visible is limited to a fraction of the septum. Chapter 5 provides new tools to quantify the reliability of the information extracted by analysing Lamb modes, which can be essential when this information is used for e.g. deciding on risky surgeries.

The results of this thesis point at a general consideration that could guide future research in this field: without a theoretical model of the heart as propagation medium for waves, SWE measurements have limited value. In fact, as has been shown in this thesis and in literature [14, 18], several parameters of the heart muscle (e.g. its curvature, its thickness variations, its anisotropic structure...) contribute to determine the speed of a traveling wave, not just the elastic moduli of the muscle; as a consequence, without knowing the role of each parameter (i.e. without a model), it is not possible to determine what a given measurement of speed means, for instance whether a high propagation speed indicates a stiffer muscle or simply a thicker one. This does not mean that all cardiac SWE research should focus exclusively on developing such a model, or that any other venue of investigation is useless: it is absolutely important that image acquisition and reconstruction techniques keep improving, and that *in-vivo* and *in-vitro* measurements provide the information necessary to develop the understanding of the cardiac muscle, which, in turn, informs the models.

### 6.4. LIMITATIONS AND FUTURE WORK

The entire research presented in this thesis constitutes but one step forward towards the realization of a cardiac SWE procedure suitable for clinical use. While each result adds

information on how to either measure or interpret SW propagation speed, each is also limited to the single facet it studied. As such, there is still a considerable gap between what can be expected from an in-vivo measurement and what can be observed.

A comprehensive model, one to account for all the features of a heart simultaneously to predict wave behaviour, should probably not be expected in the near future. However, there is a number of research avenues that would constitute a natural continuation of the work of this thesis, addressing current limitations and adding relevant pieces to the puzzle of the heart as a wave medium.

- The study of the effects of cardiac relaxation on waves provided interesting insights both from a physics perspective and in consideration of actual applications. However, one of the core simplifications that were made is also the one that brings the model furthest from reality: waves in the heart clearly cannot be assumed to be one dimensional! This simplification was necessary to isolate the effects that derive specifically from the stiffness temporal variation, but more interesting physics becomes involved once one considers at least one additional dimension: if we consider a 2D wave in a plate, in fact, Lamb dispersion also starts playing a role. Importantly, Lamb dispersion depends on the frequency content of the wave, which is altered by temporal variations of stiffness. The interplay of these two factors would likely affect the outcome of a SWE measurement performed e.g. at the onset of diastole. Future research could therefore be dedicated to shedding light on the behaviour of Lamb waves in temporally varying media. Moreover, once a clear understanding of wave behaviour in such a circumstance was achieved furthermore, another natural step would be to include in the model the thickness variations of Chapter 3.
- The analysis of Chapter 3 on Lamb waves in tapered plates could also be extended in several interesting and relevant ways. First of all, the surface of the interventricular septum is irregular and corrugated, e.g. due to the presence of the trabeculae. These irregularities effectively are thickness variations on a smaller scale than studied in this thesis, and they would likely impact wave propagation; how large their impact would be, and whether it would be relevant on a global scale or remain a local effect that averages out over a long sampling region, remains to be determined. Moreover, the theory of Lamb waves assumes a 2D plate (i.e. a plate of infinite extent and uniform shape and properties in the third dimension). An interesting research direction then could be aimed at determining whether irregularities and thickness variations in the third dimension would also affect a measurement.
- The research in Chapters 2 and 3 focused on understanding the effects that specific features (i.e. muscle relaxation and thickness variations) had on a propagating wave. As such, it was natural to choose the simplest form of wave that still contained the necessary information of each study - typically, a single sinusoidal cycle or a Gaussian pulse. Implementing a more realistic wave source could also contribute in bringing the model closer to the experimental observations. This can be more easily done when modelling ARF-induced waves, since the pulse generated by a transducer can be modelled numerically and then be implemented in FEM simulations. On the other hand, the exact mechanisms with which natural waves are

generated in the heart are not yet fully understood, and should be investigated in future studies.

- Throughout the entire thesis, when Lamb wave modes were used to reconstruct material properties, only a single mode at a time was considered (e.g. A0). This is also the approach generally described in literature, at least in the field of elastography in biological tissues. As we have shown, this puts a limitation on the data that can be collected and analysed in plates such as the septum: the entire spectrum of a wave (e.g. ARF-induced) follows a single mode only close to the surfaces; near the center of the plate, the wave energy is split between the A0 and the A1 mode, thus each provides less data. In principle, it is possible to extract and use both modes in conjunction. However, how the two modes should be combined is an open question: should they be fitted separately, and then the resulting parameters averaged? Alternatively, the error function for each could be computed separately, then combined (and then: adding the errors? Multiplying them? Which weight should a specific mode be given?), or the two modes could be considered a single entity and be compared to theoretical A0 and A1 simultaneously. Answering these questions requires careful investigation, but it could drastically improve the flexibility and accuracy of Lamb wave analysis for cardiac applications.
- The goal of this thesis is to improve the understanding of wave behaviour in the heart to enable the interpretation of a shear wave measurement in terms of stiffness. However, assuming that a single, constant value of stiffness (or, more precisely, of Young's and shear moduli) can describe entirely the heart muscle implies assuming that the heart muscle itself is isotropic and linearly elastic; on the other hand, it is known that the orientation of the muscle fibers causes the heart to be anisotropic [13–15, 50], while viscoelasticity and hyperelasticity introduce non-linear effects in how the tissue responds to deformation [50, 51]. Including all of these features into a single, comprehensive model of wave propagation would allow for a more accurate and complete description (and, therefore, interpretation) of the cardiac muscle as propagation medium, which, in turn, would inform on how to use shear waves to fully characterize the heart.

## REFERENCES

- [1] H. Kanai, *Propagation of spontaneously actuated pulsive vibration in human heart wall and in vivo viscoelasticity estimation*, IEEE Transactions on Ultrasonics, Ferroelectrics, and Frequency Control **52**, 1931 (2005).
- [2] N. C. Rouze, M. H. Wang, M. L. Palmeri, and K. R. Nightingale, *Robust estimation of time-of-flight shear wave speed using a Radon sum transformation*, Proceedings - IEEE Ultrasonics Symposium **57**, 21 (2010).
- [3] I. Z. Nenadic, M. W. Urban, S. A. Mitchell, and J. F. Greenleaf, *Lamb wave dispersion ultrasound vibrometry (LDUV) method for quantifying mechanical properties of viscoelastic solids*, Physics in Medicine and Biology **56**, 2245 (2011).
- [4] M. Tanter and M. Fink, *Ultrafast imaging in biomedical ultrasound*, IEEE Transactions on Ultrasonics, Ferroelectrics, and Frequency Control **61** (2014), 10.1109/tuffc.2014.6689779.
- [5] H. J. Vos, B. M. van Dalen, J. G. Bosch, A. F. van der Steen, and N. de Jong, *Myocardial passive shear wave detection*, in *2015 IEEE International Ultrasonics Symposium (IUS)* (IEEE, 2015) pp. 1–4.
- [6] K. J. Parker, J. Ormachea, F. Zvietcovich, and B. Castaneda, *Reverberant shear wave fields and estimation of tissue properties*, Physics in Medicine and Biology **62** (2017), 10.1088/1361-6560/aa5201.
- [7] P. Kijanka and M. W. Urban, *Local Phase Velocity Based Imaging: A New Technique Used for Ultrasound Shear Wave Elastography*, IEEE Transactions on Medical Imaging **38** (2019), 10.1109/TMI.2018.2874545.
- [8] B. Brekke, L. C. Nilsen, J. Lund, H. Torp, T. Bjastad, B. H. Amundsen, A. Stoylen, and S. A. Aase, *Ultra-high frame rate tissue doppler imaging*, Ultrasound in Medicine and Biology **40** (2014), 10.1016/j.ultrasmedbio.2013.09.012.
- [9] M. Strachinaru, J. G. Bosch, B. M. van Dalen, L. van Gils, A. F. van der Steen, N. de Jong, M. L. Geleijnse, and H. J. Vos, *Cardiac Shear Wave Elastography Using a Clinical Ultrasound System*, Ultrasound in Medicine and Biology (2017), 10.1016/j.ultrasmedbio.2017.04.012.
- [10] H. J. Vos, B. M. van Dalen, I. Heinonen, J. G. Bosch, O. Sorop, D. J. Duncker, A. F. W. van der Steen, and N. de Jong, *Cardiac Shear Wave Velocity Detection in the Porcine Heart*. Ultrasound in medicine & biology **43**, 753 (2017).
- [11] P. Santos, A. M. Petrescu, J. Pedrosa, M. Orłowska, V. Komini, J.-U. Voigt, and J. D'hooge, *Natural Shear Wave Imaging in the Human Heart: Normal Values, Feasibility, and Reproducibility*, IEEE Transactions on Ultrasonics, Ferroelectrics, and Frequency Control **66**, 442 (2019).

- [12] M. Strachinaru, J. G. Bosch, L. van Gils, B. M. van Dalen, A. F. L. Schinkel, A. F. W. van der Steen, N. de Jong, M. Michels, H. J. Vos, and M. L. Geleijnse, *Naturally occurring shear waves in healthy volunteers and hypertrophic cardiomyopathy patients*, *Ultrasound in medicine & biology* **00**, 1977 (2019).
- [13] E. D. Verdonk, S. A. Wickline, and J. G. Miller, *Anisotropy of ultrasonic velocity and elastic properties in normal human myocardium*, *J Acoust Soc Am* **92**, 3039 (1992).
- [14] M. Couade, M. Pernot, E. Messas, A. Bel, M. Ba, A. Hagege, M. Fink, and M. Tanter, *In Vivo Quantitative Mapping of Myocardial Stiffening and Transmural Anisotropy During the Cardiac Cycle*, *IEEE Transactions on Medical Imaging* **30**, 295 (2011).
- [15] M. W. Urban, B. Qiang, P. Song, I. Z. Nenadic, S. Chen, and J. F. Greenleaf, *Investigation of the effects of myocardial anisotropy for shear wave elastography using impulsive force and harmonic vibration*, *Physics in Medicine and Biology* **61**, 365 (2015).
- [16] O. Villemain, M. Correia, E. Mousseaux, J. Baranger, S. Zarka, I. Podetti, G. Soulat, T. Damy, A. Hagège, M. Tanter, M. Pernot, and E. Messas, *Myocardial Stiffness Evaluation Using Noninvasive Shear Wave Imaging in Healthy and Hypertrophic Cardiomyopathic Adults*, *JACC: Cardiovascular Imaging* **12**, 1135 (2019).
- [17] C. Pislaru, M. W. Urban, S. V. Pislaru, R. R. Kinnick, and J. F. Greenleaf, *Viscoelastic properties of normal and infarcted myocardium measured by a multifrequency shear wave method: Comparison with pressure-segment length method*, *Ultrasound in Medicine and Biology* **40**, 1785 (2014), arXiv:NIHMS150003 .
- [18] A. Caenen, M. Pernot, D. A. Shcherbakova, L. Mertens, M. Kersemans, P. Segers, and A. Swillens, *Investigating Shear Wave Physics in a Generic Pediatric Left Ventricular Model via *In Vitro* Experiments and Finite Element Simulations*, *IEEE Transactions on Ultrasonics, Ferroelectrics, and Frequency Control* **64**, 349 (2017).
- [19] I. Z. Nenadic, M. W. Urban, C. Pislaru, D. Escobar, L. Vasconcelos, and J. F. Greenleaf, *In vivo open- and closed-chest measurements of left-ventricular myocardial viscoelasticity using lamb wave dispersion ultrasound vibrometry (LDUV): A feasibility study*, *Biomedical Physics and Engineering Express* **4** (2018), 10.1088/2057-1976/aabe41.
- [20] B. A. Auld, J. H. Collins, and H. R. Zapp, *Signal Processing in a Nonperiodically Time-Varying Magnetoelastic Medium*, *Proceedings of the IEEE* **56**, 258 (1968).
- [21] S. M. Rezende and F. R. Morgenthaler, *Magnetoelastic Waves in Time-Varying Magnetic Fields. I. Theory*, *Journal of Applied Physics* **40**, 524 (1969).
- [22] L. Felsen and G. Whitman, *Wave propagation in time-varying media*, *IEEE Transactions on Antennas and Propagation* **18**, 242 (1970).
- [23] R. Fante, *Transmission of electromagnetic waves into time-varying media*, *IEEE Transactions on Antennas and Propagation* **19**, 417 (1971).
- [24] V. L. Preobrazhenskii and Y. K. Fetisov, *Magnetostatic waves in a time-dependent medium*, *Soviet Physics Journal* **31**, 898 (1988).

- [25] F. Fedotov, A. Nerukh, T. Benson, and P. Sewell, *Investigation of electromagnetic field in a layer with time-varying medium by volterra integral equation method*, Journal of Lightwave Technology **21**, 305 (2003).
- [26] A. G. Hayrapetyan, K. K. Grigoryan, R. G. Petrosyan, and S. Fritzsche, *Propagation of sound waves through a spatially homogeneous but smoothly time-dependent medium*, Annals of Physics **333**, 47 (2013).
- [27] A. G. Hayrapetyan, J. B. Götte, K. K. Grigoryan, S. Fritzsche, and R. G. Petrosyan, *Electromagnetic wave propagation in spatially homogeneous yet smoothly time-varying dielectric media*, Journal of Quantitative Spectroscopy and Radiative Transfer **178**, 158 (2016).
- [28] M. Vejdani-Jahromi, J. Freedman, Y.-J. Kim, G. E. Trahey, and P. D. Wolf, *Assessment of Diastolic Function Using Ultrasound Elastography*, Ultrasound in Medicine & Biology **44**, 551 (2018).
- [29] L. B. Keijzer, M. Strachinaru, D. J. Bowen, M. L. Geleijnse, A. F. van der Steen, J. G. Bosch, N. de Jong, and H. J. Vos, *Reproducibility of Natural Shear Wave Elastography Measurements*, Ultrasound in Medicine & Biology **45**, 3172 (2019).
- [30] H. Lamb, *On Waves in an Elastic Plate*, Proceedings of the Royal Society A: Mathematical, Physical and Engineering Sciences **93**, 114 (1917).
- [31] J. Rose, *Ultrasonic Guided Waves in Solid Media*, Vol. 9781107048 (2014) pp. 1–512.
- [32] E. Maksuti, E. Widman, D. Larsson, M. W. Urban, M. Larsson, and A. Bjällmark, *Arterial Stiffness Estimation by Shear Wave Elastography: Validation in Phantoms with Mechanical Testing*, Ultrasound in Medicine and Biology **42**, 308 (2016).
- [33] M.-C. El-Kettani, F. Luppé, and A. Guillet, *Guided waves in a plate with linearly varying thickness: experimental and numerical results*, Ultrasonics **42**, 807 (2004).
- [34] S.-Y. Huo, J.-J. Chen, G.-H. Song, and X. Han, *Asymmetric propagation of the first order antisymmetric lamb wave in a tapered plate based on time domain analysis*, Acoustical Physics **63**, 393 (2017).
- [35] J. Ormachea, K. J. Parker, and R. G. Barr, *An initial study of complete 2D shear wave dispersion images using a reverberant shear wave field*, Physics in Medicine & Biology **64**, 145009 (2019).
- [36] J. H. Langdon, E. Elegbe, and S. A. Mcleavey, *Single tracking location acoustic radiation force impulse viscoelasticity estimation (STL-VE): A method for measuring tissue viscoelastic parameters*, IEEE Transactions on Ultrasonics, Ferroelectrics, and Frequency Control **62** (2015), 10.1109/TUFFC.2014.006775.
- [37] R. J. Van Sloun, R. R. Wildeboer, H. Wijkstra, and M. Mischi, *Viscoelasticity Mapping by Identification of Local Shear Wave Dynamics*, IEEE Transactions on Ultrasonics, Ferroelectrics, and Frequency Control **64** (2017), 10.1109/TUFFC.2017.2743231.

- [38] E. Budelli, J. Brum, M. Bernal, T. Deffieux, M. Tanter, P. Lema, C. Negreira, and J. L. Gennisson, *A diffraction correction for storage and loss moduli imaging using radiation force based elastography*, *Physics in Medicine and Biology* **62** (2017), 10.1088/1361-6560/62/1/91.
- [39] P. Kijanka and M. W. Urban, *Fast Local Phase Velocity-Based Imaging: Shear Wave Particle Velocity and Displacement Motion Study*, *IEEE Transactions on Ultrasonics, Ferroelectrics, and Frequency Control* **67** (2020), 10.1109/TUFFC.2019.2948512.
- [40] P. Kijanka and M. W. Urban, *Local Phase Velocity Based Imaging (LPVI) of Viscoelastic Phantoms and Tissues*, *IEEE Transactions on Ultrasonics, Ferroelectrics, and Frequency Control* (2020), 10.1109/tuffc.2020.2968147.
- [41] E. B. Flynn, S. Y. Chong, G. J. Jarmer, and J. R. Lee, *Structural imaging through local wavenumber estimation of guided waves*, *NDT and E International* **59** (2013), 10.1016/j.ndteint.2013.04.003.
- [42] C. Pislaru, M. Urban, I. Nenadic, and J. Greenleaf, *Shearwave dispersion ultrasound vibrometry applied to in vivo myocardium*, in *2009 Annual International Conference of the IEEE Engineering in Medicine and Biology Society* (IEEE, 2009) pp. 2891–2894.
- [43] N. Bekki and S. A. Shintani, *Simple Dispersion Equation Based on Lamb-Wave Model for Propagating Pulsive Waves in Human Heart Wall*, *Journal of the Physical Society of Japan* **84**, 124802 (2015).
- [44] L. B. Keijzer, M. Strachinaru, D. J. Bowen, A. Caenen, A. F. Van Steen, M. D. Verweij, N. De Jong, J. G. Bosch, and H. J. Vos, *Parasternal Versus Apical View in Cardiac Natural Mechanical Wave Speed Measurements*, *IEEE Transactions on Ultrasonics, Ferroelectrics, and Frequency Control* **67** (2020), 10.1109/TUFFC.2020.2978299.
- [45] T. Tran, M. Sacchi, D. Ta, V.-H. Nguyen, E. Lou, and L. Le, *Nonlinear Inversion of Ultrasonic Dispersion Curves for Cortical Bone Thickness and Elastic Velocities*, *Annals of Biomedical Engineering* **47**, 2178 (2019).
- [46] L. Zhu, X. Duan, and Z. Yu, *On the Identification of Elastic Moduli of In-Service Rail by Ultrasonic Guided Waves*, *Sensors* **20**, 1769 (2020).
- [47] J. L. Deán, C. Trillo, Á. F. Doval, and J. L. Fernández, *Determination of thickness and elastic constants of aluminum plates from full-field wavelength measurements of single-mode narrowband Lamb waves*, *The Journal of the Acoustical Society of America* **124**, 1477 (2008).
- [48] J. Foiret, J.-G. Minonzio, C. Chappard, M. Talmant, and P. Laugier, *Combined estimation of thickness and velocities using ultrasound guided waves: A pioneering study on in vitro cortical bone samples*, *IEEE Transactions on Ultrasonics, Ferroelectrics, and Frequency Control* **61**, 1478 (2014).
- [49] M. Ponschab, D. A. Kiefer, and S. J. Rupitsch, *Simulation-Based Characterization of Mechanical Parameters and Thickness of Homogeneous Plates Using Guided Waves*,

- IEEE Transactions on Ultrasonics, Ferroelectrics, and Frequency Control **66**, 1898 (2019).
- [50] G. A. Holzapfel and R. W. Ogden, *Constitutive modelling of passive myocardium: a structurally based framework for material characterization*, Philosophical Transactions of the Royal Society A: Mathematical, Physical and Engineering Sciences **367**, 3445 (2009).
- [51] W. H. Gaasch, H. J. Levine, M. a. Quinones, and J. K. Alexander, *Left ventricular compliance: mechanisms and clinical implications*. The American journal of cardiology **38**, 645 (1976).

# ACKNOWLEDGEMENTS

It is with great pleasure that I have shared in this thesis the results of my four years long labor. This thesis is undoubtedly one of my biggest achievements, and I am proud to call it my own. However, sticking a single name on the front page is somewhat deceiving, as this manuscript would have not come into existence without the concerted efforts and support of so many other people. These pages are dedicated to thanking all of you, without whom I cannot imagine completing (or enjoying) my PhD.

First, I would like to thank my promotors and co-promotors, without whom I would have not started this project, and without whose guidance I would have not completed it. **Martin**, you are the first person I've met in relation to this project, and you have accompanied me all the way to where I am now. You've had the largest impact in shaping my scientific growth and perspective, and I cannot but be happy for it: I've always been impressed with your sharpness in discerning problems, causes and solutions, and I can just hope to develop in the same direction. I know I can be stubborn at times, and passionate when defending my stubborn positions; I'm very happy that you never shied away from having heated arguments when I needed it, and that you taught me to instead cool down and be sensitive when I should. **Annette**, you were the last addition to the team, but you made all the difference in the world: you have always been available to help me and guide me, and you have always been kind, fast, precise and sharp on time. In the span of half my PhD you helped me triple my output, you taught me how to simulate waves in Abaqus and how to measure them with the Verasonics, how to analyse data and how to write about it, you gave me confidence when I needed it and helped me find my own solutions, and the list would just go on and on... Without you, my thesis would surely have been a lot more *mager* and my PhD life a lot more stressful. **Rik**, your optimism and cheeriness always helped pick me up when I was feeling insecure about my work, and your questions and feedback often helped me sharpen my arguments and fight off my tendency to implicit information. Beside your help in the scientific content of this thesis, you also helped me learn how to manage the project itself, in terms of realistic planning, communication and task division. Last, but not least, **Nico**: your different perspective was helpful to keep my project grounded to the practical applications at the core of our EFFECTS project, you have always been accessible and open to discussions, and I admire how you use humor to lighten up the mood of meetings and to put people at ease.

I would also like to thank one person who was not directly involved in the EFFECTS project, but with whom collaboration emerged naturally and was both fun and proficuous. **Paul**, working with you was just as fun as discussing the qualities of italian *vs* spanish hams in the streets of Kobe. The discussions we had together were always concrete and to the point, making for highly effective meetings that resulted in two collaboration papers, a chapter of my thesis and a substantial improvement of another. All this, while keeping

the mood light and enjoyable.

Of course, a big shout-out goes to all the other PhDs in Delft and Rotterdam, without whom the past four years would have been a lot less enjoyable. **Jack**, for scientific contributions, for traveling around the world for conferences together, and for all the discussions, complaints, beers, dinners and games we've shared. **Bo, Moein Fabian**, for fighting the same battles, for the conspiracy meetings, the table tennis, the bouldering, the anime, the scientific discussions, the culinary discussions, the laughters. **Elango, Ulas, Agis, Chiara, Martijn** and the others, for time well spent at lunch breaks, evenings out and camaraderie. **Lucy** and **Geraldi**, for the phantom making, Mozarts eating, (more) table tennis, and the general fun of sharing the office with you. Finally, thank you **Lana**, for showing me around at the EMC and helping me with the experiments, for all the conversations, for offering me four-months glimpses-into-the-future, and for all the encouragement near the end of our projects.

While a lot more people had a positive impact on my PhD from within the university environment, there are four that still deserve a special mention for the help they've given me. **Angela**, for lubricating the large amount of paperwork, form-filling, meeting-scheduling work that surrounds a PhD, and for organising all the fun activities and borrels that brightened each year; **Ronald**, without whom running Abaqus and using the cluster would have been a far away dream; **Robert**, for the punctual, effective and friendly help in all things technical in Rotterdam; and **Henry**, for all the time you've dedicated to helping me with the experiments in Delft, for helping me and my students fabricate, assemble and improve the setup, for your suggestions, for always being friendly, open and available, for always being sharp on time, for the 30 C rule, and for the nice talks.

Many people were not directly involved in my day-to-day PhD life, and yet gave a substantial contribution. **Alice** and **Bart**, first of all, thank you for always putting up with ten consecutive minutes of complaints as answer to 'how are you doing?', for the months leading up to this dissertation being completed. More broadly, thanks for all the fun we've had together, for the trips, music and the magical escapism that brought relief in stressful times. **Papá**, thank you for your continued interest and encouragement. **Mamma**, thank you for your unconditional love and for sending up north the very necessary supplies of real food. **Jacopo**, thank you for your support, your advice, and for being a really good brother. **Daikokutennya**, thank you for *mhrw*.

Finally, for celebrating every small and big success, for helping me think when I got stuck, for always listening, for your help and suggestions in all practical matters, for making bad days good and good ones better; for all these things and so much more, thank you **Hanna**. I cannot imagine this PhD journey to have been nearly as succesful without your continuous support, patience and encouragement, and it certainly would have been far less enjoyable.

# LIST OF PUBLICATIONS

8. **A. Sabbadini**, A.E.M. Caenen, H.J. Vos, N. de Jong, and M.D. Verweij, "*Local reconstruction of Lamb dispersion curves for mapping of cardiac tissue stiffness*", (in preparation).
7. **A. Sabbadini**, J. Massaad, A. Caenen, N. de Jong, P.L.M.J. van Neer, and M.D. Verweij, "*On planar wave guide characterization by multi-parameter Lamb wave dispersion curve analysis*", (submitted to *Ultrasonics*).
6. J. Massaad, P.L.M.J. van Neer, D. M. van Willigen, **A. Sabbadini**, N. de Jong, M.A.P. Pertijs, and M.D. Verweij, "*Auto-calibration Procedures of Pipe and Fluid Properties prior to Ultrasonic Clamp-on Flow Metering with Matrix Transducer Arrays*", (submitted to *Transactions on Ultrasonics, Ferroelectrics, and Frequency Control*).
5. **A. Sabbadini**, A. Caenen, L.B.H. Keijzer, H.J. Vos, N. de Jong, and M.D. Verweij, "*Effects of tapering on ultrasound elastography of the interventricular septum*", (submitted to *Journal of Acoustical Society of America*).
4. **A. Sabbadini**, L.B.H. Keijzer, H.J. Vos, N. de Jong, and M.D. Verweij, "*Fundamental modeling of wave propagation in temporally relaxing media with applications to cardiac shear wave elastography*", *Journal of the Acoustical Society of America*, 2020, 147(5), pp. 3091-3099.
3. **A. Sabbadini**, A. Caenen, H.J. Vos, N. de Jong, and M.D. Verweij, "*Numerical model of Lamb wave propagation in the tapered septal wall of the heart*", *Proc. Mtgs. Acoust.* 39 (2019)
2. C. Coulais, **A. Sabbadini**, F. Vink, M. van Hecke "*Multi-step self-guided pathways for shape-changing metamaterials.*", *Nature*, vol. 561, no. 7724, p. 512 (2018).
1. L. Keijzer, **A. Sabbadini**, J.G. Bosch, M.D. Verweij, A.F.W. van der Steen, N. de Jong, H.J. Vos, "*Diffuse shear wave elastography in a thin plate phantom*", 2017 IEEE International Ultrasonics Symposium (IUS), Washington, DC, pp. 1-1 (2017).



# ABOUT THE AUTHOR

## **Alberico SABBADINI**

Alberico Sabbadini was born in Milan, Italy, on May the 12<sup>th</sup>, 1991. He received his B.Sc. degree in physics from the University of Milan in 2014. He then followed a Research Master in physics at the University of Leiden, receiving a M.Sc. degree in 2016. His research at the time was focused on mechanical metamaterials, with a thesis project on 2D foldable networks conducted at Leiden University, and another thesis project on 3D multistable metamaterials conducted at Harvard University.

In December 2016, he started a Ph.D. project in applied physics at Delft University of Technology, in the Medical Imaging group (then: Acoustical Wavefield Imaging). The goal of the project was to advance current diagnostic techniques of heart failure, and his research aimed at describing wave propagation in the heart muscle to translate speed measurements into cardiac material properties. This thesis presents the results of his four years of doctoral research.

On the 1<sup>st</sup> of February, 2021, he became a member of the Delft Haptics Lab as a Post-Doc, where he is researching applications of metamaterials and wave propagation to the field of Soft Robotics.